Scalable Microchip
Ion Traps and Guides
for Cold Molecular Ions

Inauguraldissertation

zur
Erlangung der Würde eines Doktors der Philosophie
vorgelegt der
Philosophisch-Naturwissenschaftlichen Fakultät
der Universität Basel

von

Arezoo Mokhberi
aus Shemiran, Tehran, Iran

Basel, 2016

Genehmigt von der Philosophisch-Naturwissenschaftlichen Fakultät
auf Antrag von

Prof. Dr. Stefan Willitsch und Prof. Dr. Jonathan P. Home

Basel, 24.05.2016

Prof. Dr. Jörg Schibler

Abstract

Sympathetic cooling and Coulomb crystallisation of molecular ions above the surface of an ion-trap chip were demonstrated. N_2^+ and CaH^+ ions were confined in a surface-electrode radiofrequency ion trap and cooled by the interaction with laser-cooled Ca^+ ions to secular translational temperatures in the milliKelvin range. The configuration of trapping potentials generated by the surface electrodes enabled the formation of planar bicomponent Coulomb crystals and the spatial separation of the molecular from the atomic ions. The structural and thermal properties of the crystals were characterized using molecular dynamics simulations. The effects of trap anharmoncities on the shape and energy of bicomponent crystals were theoretically investigated. It was shown that the trapping potentials can also deliberately be engineered to spatially separate ion species in bicomponent crystals. Furthermore, a multi-functional surface-electrode radiofrequency ion-trap chip has been developed to enable experiments with cold molecular ions using a monolithic device. The chip was designed to combine various tasks such as loading and preparation of ions, mass spectrometry, spectroscopy, reaction studies, and manipulation of ion crystals in a miniaturised device. This chip features carefully engineered ion channel intersections that enable transporting sympathetically cooled molecular ions in the form of bicomponent crystals. A detailed description of the fabrication and simulation of the two chips are presented. The present study extends chip-based trapping techniques to Coulomb-crystallised molecular ions with potential applications in mass spectrometry, cold chemistry, quantum technology, and spectroscopy.

To my loving parents,
Mina and Saeed

Acknowledgments

I would first like to gratefully acknowledge Stefan Willitsch for the opportunity to be part of such an exciting research program. His guidance and advice were outstanding, and his constant support and openness to discussion and debate was crucial in making this work the success that it is.

I would like to acknowledge Roman Schmied for the fruitful and enjoyable collaboration on the optimisation of the "multi-functional chip", and for his kind and ceaseless openness to discussion.

I would like to acknowledge the mechanical workshop for the excellent and ceaseless support and high-quality work: Dieter Wild, Philipp Knöpfel, Grischa Martin, Volkan Demir, and Sascha Martin.

I would like to warmly acknowledge the assistance with electronics from Georg Holderied, Andreas Tonin, and Roberto Maffiolini, and the assistance with lasers and programming from Anatoly Johnson, as well as the assistance with software licenses from Mike Devereux.

I would like to acknowledge Xin Tong for his patient demonstration of some of key techniques used in this work, as well as for his kind openness to discussion, and for the productive working environment that he helped to maintain during his time in the group.

I would like to acknowledge former and current members of the group for the help and support, as well as for creating pleasant working atmosphere and for being open to useful discussions, in particular Matthias Germann for help with computer programming. I would like to thank my project student Dominik Rohner for his very good work on some MD simulations at the initial stage of the project, however those simulations are not presented in this thesis due to the simplification used.

I would like to gratefully acknowledge Jonathan Home for kindly agreeing to co-examine this work, as well as for helpful discussions and insightful corrections on the thesis.

I would like to acknowledge Markus Meuwly for kindly agreeing to be the chair of the doctoral examination.

I would like to acknowledge the enjoyable collaboration with the Swiss Center for Electronics and Microtechnology *CSEM* in Neuchâtel, Switzerland, on the fabrication of the "multi-functional chip". This is currently being executed under supervision of Yves Petremand, and helpful discussions with him and Olivier Dubochet are acknowledged.

I would like to acknowledge Bjoern Lekitsch, from Ion Quantum Technology Group, University of Sussex, for helpful discussions and advices about the fabrication of the "multi-functional chip".

I would like to acknowledge Corey A. Rice and Ian Rouse for careful reading of the manuscript of this thesis, as well as for helpful discussions.

This work has been supported by the University of Basel, the COST Action MP1001 'Ion Traps for Tomorrow's Applications', the Swiss National Science Foundation through the National Centre of Competence in Research 'Quantum Science and Technology' and the Swiss Nanoscience Institute.

Finally, I would like to wholeheartedly thank my family, especially my parents, Mina and Saeed, for their kindest and endless support, allowing me to give my best to this work. Also, I would like to thank my kind sisters Adele and Azade, who also helped me with graphics software.

Contents

Chapter 1

Introduction

1.1 Cold and controlled atomic and molecular ions

Major developments in modern atomic, molecular, and optical physics over the past decades are due to a remarkable progress in techniques for producing, trapping and controlling cold and ultracold atoms [1, 2]. Once particles are cooled to low kinetic energies, their wave nature may manifest itself in measurements or quantitative observations[1]. The techniques developed for coherent manipulation of atomic systems using electromagnetic interactions were pivotal for many advancements [3]. Such well-controlled quantum systems provide experimental benchmarks to test theories as well as detailed probes of fundamental concepts, e.g., the time invariance of physical constants [4, 5], the Lorentz covariance [6], and collision mechanisms [7, 8].

Along with the growth of fundamental studies, cold atoms and atomic ions have important applications. Quantum information science has found one of its most promising platform in laser-cooled trapped ions [9], and the experimental achievements attained thus far in quantum computation are to a large extent based on ion-trap processors [10–13]. Quantum simulations [14–16], quantum-

---

[1] The measure often used for quantification is the de Broglie wavelength of the particle $\lambda = h/mv$, where h is the Planck's constant, and m and v are the mass and velocity of the particle.

state engineering [17], atom interferometry and meteorology [18–20], in particular extraordinarily precise atomic clocks [21], have been realised based on cold atomic systems. These cutting-edge fields are expected to play leading roles in new jumps in science and technology.

Originally inspired by the field of cold atoms, cold molecule research became a widely interesting topic which has introduced innovative approaches and pursued its own aims [22]. Molecular systems are more complicated compared to atomic ones, but also more appealing from some aspects. The wealth of the frequency ranges available in a molecular quantum system resulting from the electronic, vibrational, and rotational degrees of freedom offers untold possibilities for new experiments. In addition, molecules may exhibit large electric and magnetic moments, which can enable better control of the molecules, as well as properties that do not exist in atoms, e.g., conformations which are important for reaction studies [23] and chirality which is important for symmetry violation studies [24].

The exquisite control of the internal and external degrees of freedom of the molecules which can already be achieved paves the way for new applications in quantum technology [25, 26], precision spectroscopy [27–31], mass spectrometry [32, 33], reaction studies, and cold chemistry [34–37]. Cold molecular ions may enable even higher precision for some applications such as time-frequency standards [38] and explorations of the time invariace of physical constants [39, 40].

However, significant difficulties in cooling molecules arise because, in most cases, their complex energy level structure precludes the implementation of closed optical transitions. Thus, standard techniques of atomic physics like laser cooling and fluorescence detection of single particles are at best only applicable to a very restricted number of molecular systems (Section 1.2.1). Therefore, significant efforts have been invested into developing methods for controlling translational and internal degrees of freedom of molecules (Section 1.2).

In this context, "cold" refers to a low average kinetic energy of species in the range of $1\,\mathrm{mK} \lesssim \langle E_{kin}\rangle/k_\mathrm{B} \lesssim 1\,\mathrm{K}$, while "ultracold" denotes $\langle E_{kin}\rangle/k_\mathrm{B} \lesssim 1\,\mathrm{mK}$. It is customary in the field to present the average kinetic energy of samples $\langle E_{kin}\rangle$ in units of Kelvin with $\langle E_{kin}\rangle/k_\mathrm{B}$, where k_B is the Boltzmann constant. However, in many cases, no temperature is assigned to species due to the fact that they are not in thermal equilibrium with their environment, and hence, their velocity distribution significantly deviates from Maxwell-Boltzmann behaviour [22].

1.2 Methods of production

The technology for preparing and controlling cold and ultracold molecular species has made impressive progress over the past 20 years [41–43]. The methods developed are broadly divided into two categories of indirect and direct techniques. In the former, laser-cooled atoms (usually alkali metals) are combined to form molecules. In photoassociation, a bound state, which is often excited rotationally and vibrationally, is formed by the absoption of a photon [44]. Magnetic association via Feshbach resonances is another important mechanism [45]. In both methods, the molecules formed are translationally ultracold, as their constituent atoms. Furthermore, the resulting molecular clouds feature high phase-space density, which is important for the formation of Bose-Einstein condensates (BEC). However, these techniques are limited to mostly alkali metal dimers [22].

Direct methods start with the molecules to be studied and employ a range of strategies which enable cooling a variety of molecules. Buffer gas cooling is widely used owing to its generality and simplicity, which depends only on the elastic scattering cross section of cold helium and target molecules. The molecules cooled in buffer-gas cells can be trapped magnetically or used in order to generate molecular beams [22]. Another method is based on selecting out a slow fraction of a molecular sample taking advantage of the Stark effect in a curved electrostatic quadrupole [46], which was employed in a pioneering ion-neutral collision experiment at milliKelvin temperatures [34]. Pulsed molecular beams and supersonically expanded packets of molecules are required as starting points for an important class of cooling techniques: Stark and Zeeman deceleration [47]. In these techniques, inhomogeneous electric and magnetic fields are used to deterministically accelerate or decelerate neutral molecules to desired velocities. Recently, centrifuge deceleration [48] and optoelectrical cooling of polar molecules using the Sisyphus cooling technique [49] have been demonstrated. Such outstanding achievements, however, have been obtained in very expensive and sophisticated machines. The diversity of these techniques and the complexity of the experimental setups used again emphasize formidable challenges in the field.

Molecular ions can be more precisely controlled to achieve ultralow temperatures. Standard techniques for trapping charged particles in ion traps [50] (Section 1.3) have been widely used in molecular physics, e.g., spectroscopy and reaction studies [51]. Therefore, ion trapping combined with cooling techniques has become a versatile tool in the field. The key advantage of this technique is that ions are highly isolated from the environment which allows long interrogation times. In the following, we focus on Doppler laser cooling and sympathetic cooling; two methods which enable the formation of cold molecular ions at sub-Kelvin temperatures.

1.2.1 Doppler laser cooling

Doppler laser cooling [52] has been a standard technique in atomic physics for more than three decades [53]. In Doppler laser cooling, absorption of light leads to the transfer of momentum from the radiation field to the particles. If the atoms decay by spontaneous emission, the associated recoil is in a random direction, and thus, over many scattering events (e.g., $> 10^4$) is averaged out. Photons of the laser beam, which is slightly red detuned from the atomic resonance, are preferentially absorbed by those atoms which are moving antiparallel to the k-vector of the beam and fulfil the frequency mismatch according to the Doppler shift. Selected atomic choices for laser cooling are typically alkaline atoms, e.g., Li, Na, K, Rb, and Cs, and alkaline earth ions, for instance Be^+, Mg^+, Ca^+, Ba^+, and Sr^+, due to their simple energy-level structures which allow the implementation of closed optical transitions.

Ions confined in a trap (Section 1.3) can be laser cooled such that they undergo a phase transition resulting in the formation of ordered structures of translationally cold and spatially localised ions called Coulomb crystals [54, 55]. To achieve this, the potential energy of ions have to exceed their kinetic energies by a factor of $\Gamma \gtrapprox 170$ in a typical experiment. This factor is called plasma-coupling parameter and is expressed by:

$$\Gamma = \frac{E_{\mathrm{pot}}}{E_{kin}} = \frac{q^2}{4\pi\epsilon_0 a_{\mathrm{WS}} k_{\mathrm{B}} T} \quad . \tag{1.1}$$

Here, q is the charge of the ion and a_{WS} is the Wigner-Seitz radius which is given by the density of ions in these systems [56]. Intriguing properties of such confined plasmas have extensively been explored [57–60]. More importantly, the application of such crystals in various experiments resulted in developing novel techniques for precise measurements, e.g., collision studies [8, 34, 36].

Sympathetic crystalisation of co-trapped ions [61] in particular is of great importance for experiments with molecules enabling the cooling of cold molecular ions down to temperatures of milliKelvins. This technique is used as the basis of the present study, and structural and thermal properties of a variety of Coulomb-crystallised molecular ions have been explored.

Laser cooling of molecules requires nearly diagonal Frank-Condon factors which allow acceptably small losses in the cooling cycles. These quasi-closed optical cycles have been employed in order to cool magneto-optically trapped SrF [62], YO [63], and more recently a supersonic beam of CaF molecules [64]. In addition, theoretical investigations have identified promising candidates for such experiments; RaF [65, 66] as well as ionic species BH^+ and AlH^+ [67]. There are also proposals for the laser cooling of alkaline earth metal monohydrides [68, 69] and OH molecules [70]. Recent calculations point to the possibility of the laser cooling of some non-linear, polyatomic molecules such as $CaCH_3$ [71] which have yet to be demonstrated. Although these studies present new perspectives for experiments with cold molecules, the very limited choice of molecules restricts wider applications and thus alternative techniques are required.

1.2.2 Sympathetic cooling

Sympathetic cooling relies on the energy exchange between simultaneously trapped ions of different types[2] where only one is directly cooled with radiation. Laser-

---

[2] To achieve this, the trapping parameter have to be chosen such that both species fulfil the trapping stability criteria (Section 2.1.1).

cooled atomic ions acting as a charged "buffer gas" serve to remove the kinetic energy of other ionic species through elastic collisions. The key advantage of this technique is that it does not depend on internal level structures or electric or magnetic moment of the particles. The cooling efficiency depends on the mass-to-charge ratio, temperatures, spatial distribution, and the number of ions of both types [72]. The long range Coulomb scattering allows efficient cooling which may result in translational temperatures below 10 mK for sympathetically cooled ions [61]. Consequently, the benefits of laser-cooled atomic ions, i.e., long-term confinement and low temperatures, are transferred to sympathetically cooled ions while they are not internally perturbed by the cooling lasers applied.

As follows from the above discussion, this method is widely applicable to a variety of ion species, and is rightly known as a "work-horse" technique in the field [54]. In analogy to the development of the cold atomic and cold molecular physics, sympathetically cooled ions were first observed in atomic systems [73, 74], and later in molecular ones [75, 76]. The technique is applicable to molecules ranging from diatomic to large biomolecules [77] and highly charged particles [78]. It has recently been combined with helium buffer-gas techniques to also achieve cooling of the internal molecular degrees of freedom [79].

A number of other important applications significantly benefits from sympathetic cooling. For instance, the central idea of quantum logic spectroscopy relies on this method [80]. For quantum information processing based on trapped ions, sympathetic cooling is important because the laser cooling would cause dissipation of the internal states of ions, while it is crucial to implement quantum logic operations without affecting the information stored in ions [81, 82].

In this work, sympathetic cooling and Coulomb crystallisation of molecular ions were used as the basis for all the experiments demonstrated. The theoretical studies, e.g., molecular dynamic simulations, as well as calculations for trapping potentials and guides are based on this cooling technique for molecular ions.

1.3 Ion trapping advancements

Ion traps have taken a prominent position in physics and chemistry since their development in the 1950's and 1960's by Hans Dehmelt [83] and Wolfgang Paul

[84]. Two types of ion traps are mainly used; Paul and Penning traps. In Paul traps (also referred to as radiofrequency (RF) traps), time-varying and static electric fields are applied together to generate a three-dimensional confinement. By contrast, in a Penning trap a magnetic field in combination with a static electric field provides the trapping potential. In recent years, several variants of trap geometries have been employed leading to revolutionary developments in ion trapping and have enabled unprecedented levels of control over quantum systems. One groundbreaking advance was the miniaturisation of ion traps [85] which was inspired by the requirement for the scalability that possibly enables large-scale quantum information processing [86].

A special variant of miniaturised traps are surface-electrode (SE) traps in which all electrodes lie in a plane and the ions are trapped at a certain height above the surface [85, 87, 88]. This new generation of ion traps offers high flexibility in shaping the trapping potentials, large gradients of potentials and fields, and an open geometry which significantly facilitates, e.g., optical access. Such traps have been used for the precise manipulation of trapped particles by capitalizing on the strong field gradients achievable in microstructured devices [89], for improving the scalability of traps [90] which is of importance for the fast shuttling and separation of ions [91, 92], and quantum simulations [93].

An extremely important aspect of miniaturised traps is that they can benefit from high precision fabrication techniques. In particular, SE traps feature higher flexibility for designing and shaping electrode structures on two-dimensional geometries, as well as significant potential for scalability. Therefore, cutting-edge technologies in, e.g, micro-electro-mechanical systems (MEMS) [85, 94], surface science [95], and semiconductor technology [96, 97] have been used to overcome practical limitations of conventional machining methods.

While chip techniques for atomic species are by now well established [98], their extension to molecules has proven challenging. For polar neutral molecules such as CO and Rydberg atoms, the deceleration and trapping on a chip has recently been achieved using their interaction with time-varying inhomogeneous electric fields generated by microstructured electrodes on a surface [99, 100]. In this study, we present the application of this new trapping technology for experiments with cold molecular ions based on radio-frequency (RF) surface-electrode ion traps.

1.4 This thesis

This work presents an investigation into the capabilities of single-layer ion-trap chip devices for experiments with cold molecular ions. The aim of the project was first to demonstrate sympathetic cooling of molecular ions in a surface-electrode radiofrequency trap, and second to characterise the energetic and structural properties of bicomponent Coulomb crystals in the trap using molecular dynamics (MD) simulation methods (Section 2.6.2).

A theoretical introduction to the concepts used in this thesis is presented in Chapter 2. As a part of this work, a six-wire, SE ion trap as well as the experimental setup used to test the trap were developed of which Chapter 3 provides a detailed account.

This thesis presents the first demonstration and characterization of sympathetically cooled molecular ions in a surface-electrode ion trap. N_2^+ and CaH^+ ions were confined in the SE trap and cooled by the interaction with laser-cooled Ca^+ ions to secular translational temperatures in the milliKelvin range[3]. The configuration of trapping potentials generated by the surface electrodes enabled the formation of planar bicomponent Coulomb crystals and the spatial separation of the molecular from the atomic ions on the chip. The influence of trap anharmonicities on the properties of bicomponent crystals was theoretically explored giving an insight into the main distinct between symmetric and asymmetric trapping architectures. These results are discussed in detail in Chapter 4, and covered in Refs. [104, 105].

Having established the basis for experiments with molecular ions in a SE trap, a multi-functional monolithic chip was designed which integrates dedicated trapping zones for the preparation, cooling, spectroscopy, chemistry and mass spectrometry of molecular ions. The chip consists of two planar junctions

---

[3] Nitrogen molecular cation is an interesting choice because it is one of the most extensively studied molecules in spectroscopy [101]. Metal hydride ions are useful for applications in quantum logic spectroscopy [102], frequency standards and black-body radiation (BBR) thermometry [103].

(Section 2.5.2); a cross between four quadrupolar channels and a quadrupole-to-octupole field-modifying junction. Capitalizing on the flexibility of planar structures, each constituent element of the geometry has comprehensively been optimised. As a result, the optimised structure will enable smooth transporting of cold ions via precisely shaped trapping potentials in the quadrupolar as well as octupolar channels. Chapter 5 presents details of the design of this multi-functional chip. Considerations with regards to the fabrication of the chip are given in Chapter 6. The resulting work is the first step that has been accomplished towards "Cold Chemistry on a Chip". Finally, Chapter 7 summarises the results achieved and gives an outlook for the future experiments.

Chapter 2

Concepts

2.1 Radiofrequency ion traps

2.1.1 Linear Paul traps

Earnshaw's theorem states that charged particles cannot be confined solely by means of electrostatic forces [106]. Therefore, radiofrequency ion traps (also referred to as Paul traps) employ oscillating electric fields in combination with static fields to provide three-dimensional confinement. A schematic of a linear Paul trap is depicted in Fig. 2.1 (a). The rods labelled with "RF" are held at $V_{\mathrm{RF}}\cos(\Omega_{\mathrm{RF}}t)$, where V_{RF} and Ω_{RF} denote the zero-to-peak amplitude and frequency of the RF voltage, respectively. Additionally, a static potential U_{END} is applied to each "endcap" electrode. Near the geometrical centre of the trap, this configuration of voltages[1] gives rise to a potential

$$\varPhi(x,y,z,t) = \frac{V_{\mathrm{RF}}}{2}\left(1 - \tfrac{(x^2-y^2)}{R^2}\right)\cos(\Omega_{\mathrm{RF}}t) + \frac{\kappa U_{\mathrm{END}}}{z_0^2}\left(z^2 - \tfrac{x^2+y^2}{2}\right). \quad (2.1)$$

---

[1] Note that if the RF potential is generated by all rods with RF voltages of opposite polarity applied to adjacent electrodes, e.g. following Ref. [107], the RF potential is given by

$$\varPhi_{\mathrm{RF}} = V_{\mathrm{RF}}(\frac{x^2-y^2}{R^2})\cos(\Omega_{\mathrm{RF}}\mathrm{t}),$$

which provides two times stiffer confinement. In miniaturised traps, only one RF voltage is applied to avoid heating effects [85].

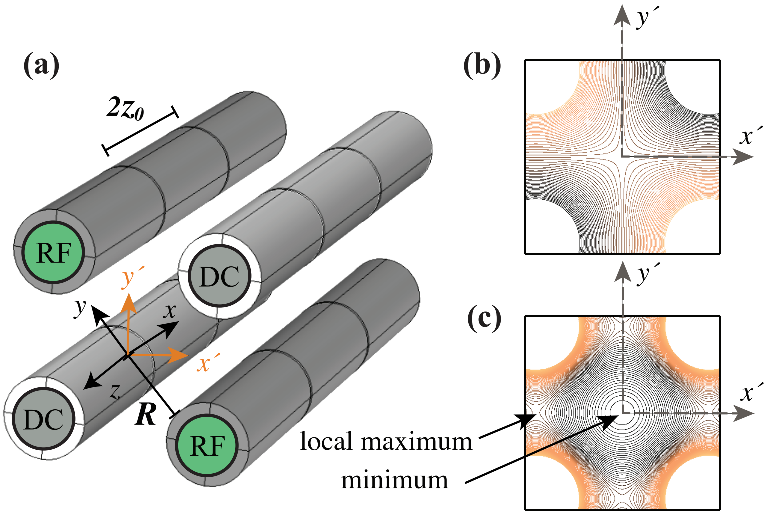

Figure 2.1: (a) A schematic of the electrode configuration of a linear Paul trap following the design of Ref. [8]. The rods are assumed to be parallel and located at the vertices of a square. The eight outer most segmented electrodes are called "endcap" electrodes. (b,c) Contour plots of the RF potential at the instance $t = 0$ and the normalised pseudopotential (Section 2.1.3) in the radial plane perpendicular to the trap symmetry axis z. The ions are trapped at the minimum of pseudopotential where the RF field vanishes (RF null line).

Here, R is a scaling factor, often taken as the distance between the trap centre and the nearest electrode [108], $2z_0$ is the distance between the endcap electrodes, and κ is a geometrical factor which is determined either using numerical solutions of the Laplace equation for a specific geometry, or experimentally [109]. Due to the symmetry of the trap geometry, it is often sufficient to assume[2] that only orthogonal harmonic terms contribute to the static potential[3]

$$\Phi_{\mathrm{DC}} = C_{2x}x^2 + C_{2y}y^2 + C_{2z}z^2. \tag{2.2}$$

---

[2] For a given trap, the validity of this assumption has to be verified.

[3] Although "DC" stands for direct current, it is customary in the ion trapping community to use this abbreviation for static potentials as well as the trap electrodes that are used to generate static trapping fields.

The coefficients C_{2x}, C_{2y}, and C_{2z} can be extracted from a three-dimensional fit to numerically calculated potentials, and thus, κ is given by:

$$\kappa = \frac{C_{2z} z_0^2}{U_{\mathrm{END}}} = \frac{-2C_{2x} z_0^2}{U_{\mathrm{END}}} = \frac{-2C_{2y} z_0^2}{U_{\mathrm{END}}} \tag{2.3}$$

For instance, for the trap employed in [8] it was calculated to be 0.334 [110]. The electric field close to the trap centre is written as:

$$\mathbf{E} = -\nabla \mathit{\Phi} = \begin{pmatrix} -\frac{V_{\mathrm{RF}}}{R^2}\cos(\Omega_{\mathrm{RF}} t)x + \frac{\kappa U_{\mathrm{END}}}{z_0^2} x \\ +\frac{V_{\mathrm{RF}}}{R^2}\cos(\Omega_{\mathrm{RF}} t)y + \frac{\kappa U_{\mathrm{END}}}{z_0^2} y \\ -2\frac{\kappa U_{\mathrm{END}}}{z_0^2} z \end{pmatrix}. \tag{2.4}$$

2.1.2 Motion of trapped ions and the Mathieu equations

The classical equations of the motion for a single ion with mass m in a linear Paul trap are derived from the field in Eqn. 2.4: $F_i = m\ddot{r_i} = qE_i$, $i \in \{x, y, z\}$, where $r_x \equiv x(t)$, $r_y \equiv y(t)$, and $r_z \equiv z(t)$, and hence is formulated as:

$$\ddot{r_i} + [a_i + 2q_i \cos(2\tau)]r_i = 0, \tag{2.5}$$

where $\tau \equiv \frac{\Omega_{\mathrm{RF}}}{2} t$ and

$$\begin{cases} a_x = a_y = -\dfrac{1}{2} a_z = -\dfrac{4q\kappa U_{\mathrm{END}}}{m\Omega_{\mathrm{RF}}^2 z_0^2}, \\ q_x = -q_y = \dfrac{2qV_{\mathrm{RF}}}{m\Omega_{\mathrm{RF}}^2 R^2}, \quad q_z = 0. \end{cases} \tag{2.6}$$

In the z direction, when $qU_{\mathrm{END}} \propto a_z > 0$, ions are confined in a harmonic well along the trap axis with a frequency $\omega_z = \frac{\Omega_{\mathrm{RF}}}{2}\sqrt{a_z}$. In the x and y directions, Eqn. 2.5 is in the form of the standard Mathieu equation [111]. The solutions are given by:

$$r_j(\tau) = A_j e^{i\beta_j \tau} \sum_{n=-\infty}^{n=+\infty} C_{2n} e^{i2n\tau} + B_j e^{-i\beta_j \tau} \sum_{n=-\infty}^{n=+\infty} C_{2n} e^{-i2n\tau}, \quad j \in \{x, y\}. \tag{2.7}$$

Here, A_j and B_j are constants which depend on the inital conditions. By substituting Eqn. 2.7 into Eqn. 2.5, one obtains a recursion relation for C_{2n} as well as an expression for β_i [50]. For stable ion trapping, the primary stability region in the a_i-q_i space is used [50, 112]. When $|a_i|$, $|q_i| \ll 1$, the solution in Eqn. 2.7 is approximated by keeping only the terms with the C_{-2}, C_0, C_{+2} coefficients. Thus, the value of β_i can be analytically calculated,

$$\beta_i \simeq \sqrt{a_i + \frac{q_i^2}{2}}. \tag{2.8}$$

Thus, the solution of Eqn. 2.5 is given by [111]:

$$r_i(t) \simeq r_{1i}\cos(\omega_i t + \phi_i)[1 + \frac{q_i}{2}\cos(\Omega_{\mathrm{RF}} t)], \tag{2.9}$$

where ϕ_i depends on the initial conditions of the position and velocity of the ion. The first term called the "secular" motion of the ion is the harmonic oscillation at frequency ω_i,

$$\omega_i \simeq \frac{\Omega_{\mathrm{RF}}}{2}\beta_i \quad . \tag{2.10}$$

The second term driven by the RF field is referred to as "micromotion" of the ion. This "intrinsic" micromotion is unavoidable and arises from the secular motion of the ion around the RF null line. If the trapped ion is in addition subject to a uniform static electric field $\mathbf{E}_{\mathrm{DC}}$, the solution in Eqn. 2.9 becomes:

$$r_i(t) \simeq r_{1i}\cos(\omega_i t + \phi_i)[1 + \frac{q_i}{2}\cos(\Omega_{\mathrm{RF}} t)] + \frac{qE_{\mathrm{DC,i}}}{m\omega_i^2} + \frac{\sqrt{2}E_{\mathrm{DC,i}}}{m\omega_i\Omega_{\mathrm{RF}}}\cos(\Omega_{\mathrm{RF}} t). \tag{2.11}$$

These two additional terms result from the displacement of the ion from the RF null line. The third term is the positional offset caused by $\mathbf{E}_{\mathrm{DC}}$, and the forth term is called "excess" micromotion. This cannot be repressed by laser cooling, and therefore, static fields driving ions off the RF null line must be suppressed to avoid adverse effects of excess micromotion, such as the alternation of the atomic transition line shape, second-order Doppler shift and its adverse effects on the laser cooling rate [108].

In more generality, Eqn. 2.5 can be rewritten as [113]

$$\ddot{x}_i + \sum_j A_{ij} x_j + 2 \sum_j Q_{ij} x_j \cos(2\tau) = 0, \tag{2.12}$$

where x_i, $i \in \{x, y, z\}$, stand for the ion coordinates. A and Q matrices represent multidimensional generalised stability parameters [113, 114]:

$$A_{ij} = \frac{4q}{m\Omega_{\mathrm{RF}}^2} \left(\frac{\partial^2 \mathit{\Phi}_{\mathrm{DC}}}{\partial x_i \partial x_j} \right) \quad , \quad Q_{ij} = \frac{2q}{m\Omega_{\mathrm{RF}}^2} \left(\frac{\partial^2 \mathit{\Phi}_{\mathrm{RF}}}{\partial x_i \partial x_j} \right). \tag{2.13}$$

If the trapping potential is perfectly harmonic, the A and Q matrices are traceless due to the Laplace equation (Section 3.1.4).

Usually pseudopotential approximation (Section 2.1.3) is used first to determine the trapping frequencies. Strictly speaking, the trapping frequencies are obtained from the eigenvalues of the Hessian matrix of the trapping potential $\mathit{\Phi}$,

$$H = q \begin{pmatrix} \partial_x^2 & \partial_x \partial_y & \partial_x \partial_z \\ \partial_y \partial_x & \partial_y^2 & \partial_y \partial_z \\ \partial_z \partial_x & \partial_z \partial_y & \partial_z^2 \end{pmatrix} \mathit{\Phi}. \tag{2.14}$$

where $\partial_{x_i} \equiv \frac{\partial}{\partial x_i}$, $i \in \{x, y, z\}$, and are evaluated at the ion's position, i.e., the trap centre. The motional frequencies ω_i are then calculated from the eigenvalues Λ_i:

$$\omega_i = \sqrt{\frac{\Lambda_i}{m}}. \tag{2.15}$$

The second derivatives are often referred to as "curvature". The harmonic oscillations occur along three orthogonal eigenvectors which define a basis along which the ions' motion is independent from other directions. These eigenvalues and eigenvectors define the normal modes of a given system. In principle, for multipole ions in a trap as well as in the presence of anharmonic terms in $\mathit{\Phi}$, these motions are coupled [115].

In general, for all kinds of linear (i.e., translationally symmetric) RF traps, in the absence of the static field, transverse secular frequencies are well approximated by $\omega_x = \omega_y = q_x \Omega_{\mathrm{RF}} / \sqrt{8}$ [3]. In any case, $\omega_x \neq \omega_y$ may mean that a_x and a_y have different values and/or signs that result in the broken degeneracy of these radial oscillating modes (Section 3.1.4). The operation conditions for a given trap is often characterised by the "anisotropy parameter" [116, 117]

$$\alpha_{(x,y)} = \omega_z^2/\omega_{(x,y)}^2, \tag{2.16}$$

where, the z axis is the weakest axis. For specific values of $\alpha_{(x,y)}$, ion Coulomb crystals undergo phase transitions [118] and planar Coulomb crystals can be formed which are important for applications in quantum computation and quantum simulation [119–121].

2.1.3 Adiabatic approximation

Consider a particle with mass m and charge q under the influence of a trapping electric field $\mathbf{E} = \mathbf{E_0}(\mathbf{r})\cos(\Omega_{\mathrm{RF}}t)$. One can assume that the spatial variation of this field is smooth such that the Taylor expansion of $\mathbf{E_0}(\mathbf{r})$ can be truncated after two terms:

$$\mathbf{E_0}(\mathbf{r}(t)) = \mathbf{E_0}(\mathbf{r}_s(t)) - (\mathbf{r}_0 \cdot \nabla)\mathbf{E_0}(\mathbf{r}_s(t))\cos(\Omega_{\mathrm{RF}}t). \tag{2.17}$$

Here, the ion coordinate $\mathbf{r}(t)$ is given by superimposing a smooth drift term $\mathbf{r}_s(t)$ and a fast oscillating term $\mathbf{r}_\mu(t)$:

$$\mathbf{r}(t) = \mathbf{r}_s(t) + \mathbf{r}_\mu(t) = \mathbf{r}_s(t) + \mathbf{r}_0\cos(\Omega_{\mathrm{RF}}t), \tag{2.18}$$

where $\mathbf{r}_0 = \frac{-q}{m\Omega_{\mathrm{RF}}^2}\mathbf{E_0}$. By substituting Eqn. 2.17 and 2.18 into the equation of the motion of the ion $m\ddot{\mathbf{r}} = q\mathbf{E}$, one obtains:

$$m\ddot{\mathbf{r}}_s - m\Omega_{\mathrm{RF}}^2\mathbf{r}_0\cos(\Omega_{\mathrm{RF}}t) = q\mathbf{E_0}(\mathbf{r}_s)\cos(\Omega_{\mathrm{RF}}t) - q(\mathbf{r}_0 \cdot \nabla)\mathbf{E_0}(\mathbf{r}_s)\cos^2(\Omega_{\mathrm{RF}}t). \tag{2.19}$$

This expression is simplified using the vector analysis identity $(\mathbf{E}_0 \cdot \nabla)\mathbf{E_0} = \frac{1}{2}\nabla\mathbf{E}_0^2 - \mathbf{E}_0 \times (\nabla \times \mathbf{E}_0)$, and because $\nabla \times \mathbf{E}_0 = 0$, the time averaged form of

Eqn. 2.19 can be written as:

$$\langle m\ddot{\mathbf{r}}_s\rangle_t = \langle q^2\frac{1}{2}\nabla\mathbf{E}_0^2\cos^2(\Omega_{\mathrm{RF}}t)\rangle_t, \tag{2.20a}$$

$$m\ddot{\mathbf{r}}_s = -\frac{q^2}{4m\Omega_{\mathrm{RF}}^2}\nabla\mathbf{E}_0^2. \tag{2.20b}$$

The right-hand side of Eqn. 2.20 can be seen as a negative gradient of a time-independent potential called the "pseudopotential",

$$\varPhi_{\mathrm{ps}} = \frac{q^2}{4m\Omega_{\mathrm{RF}}^2}\mathbf{E}_0^2. \tag{2.21}$$

Note that this result is obtained based on two assumptions. First, $(\mathbf{r}_s(t))$ changes slowly on the time scale of $2\pi/\Omega_{\mathrm{RF}}$, i.e., $\ddot{\mathbf{r}}_s \ll \Omega_{\mathrm{RF}}\dot{\mathbf{r}}_s$. The second is $\mathbf{E_0}(\mathbf{r}_s(t))$ is approximately constant over one cycle of the RF oscillation, that is $\dot{\mathbf{r}}_0 \ll \Omega_{\mathrm{RF}}\mathbf{r}_0$. These two assumptions together are referred to as the "adiabatic approximation". Behaving adiabatically typically requires a high RF frequency and other changes in time to be slow. This is quantified using a dimensionless ratio called the "adiabacity parameter"

$$\eta = \frac{\|2(\mathbf{r}_0.\nabla)\mathbf{E_0}(\mathbf{r}_s)\|}{\|\mathbf{E_0}(\mathbf{r}_s)\|}. \tag{2.22}$$

This can be simplified to:

$$\eta = \frac{2q\|\nabla\mathbf{E_0}(\mathbf{r}_s)\|}{m\Omega_{RF}^2}. \tag{2.23}$$

The validity of the adiabatic approximation relies on small values of $\eta < 0.3$ [51]. This ensures that the spatial variation of the inhomogeneous electric field is smooth such that the change of the field is much smaller than the field itself (Eqn. 2.22).

The total energy of ions within this approximation is a constant of the motion, and is formulated as:

$$E = \frac{1}{2}m\dot{\mathbf{r}}_s^2 + \frac{q^2}{4\ m\Omega_{\mathrm{RF}}^2}\ \|\nabla\ \varPhi_{\mathrm{RF}}\|^2 + q\varPhi_{\mathrm{DC}}. \tag{2.24}$$

The first term is the kinetic energy of the slow motion called secular kinetic energy. The second and third term together form the total effective trapping potential $\mathit{\Phi}_t$ experienced by the ions as the sum of a time-independent pseudopotential $\mathit{\Phi}_{ps}$ and a static potential $\mathit{\Phi}_{DC}$:

$$\begin{aligned}\mathit{\Phi}_t(x,y,z) &= \mathit{\Phi}_{ps} + \mathit{\Phi}_{DC} \\ &= \frac{q^2}{4\ m\Omega_{RF}^2}\ \left\|\nabla\ \mathit{\Phi}_{\mathrm{RF}}\right\|^2 + q\mathit{\Phi}_{\mathrm{DC}}.\end{aligned} \tag{2.25}$$

The pseudopotential represents the kinetic energy of the micromotion of the ion. For considering micromotion effects, the position and kinetic energy of the ion due to micromotion can be written as:

$$\mathbf{r}_\mu(t) = -\frac{q}{m\Omega_{\mathrm{RF}}^2}\mathbf{E_0}\cos(\Omega_{\mathrm{RF}}t), \tag{2.26a}$$

$$E_{\mu,\mathrm{kin}} = \frac{q^2}{2m\Omega_{\mathrm{RF}}^2}|\mathbf{E_0}|^2\sin^2(\Omega_{\mathrm{RF}}t), \tag{2.26b}$$

The trap depth is calculated within the adiabatic approximation. The intrinsic trap depth is defined as the difference between the pseudopotential minimum at the RF null line and its local maxima, i.e., saddle points shown in Fig. 2.1 (c). The effective or total trap depth is defined as the difference between the minimum of the total trapping potential (Eqn. 2.25) and its saddle points, where ions can escape from the trap, in the presence of the static potential.

2.1.4 Types of trap geometries

A linear Paul trap (Section 2.1.1) can be modified in order to create linear RF traps which are suitable for miniaturisation. Figure 2.2 illustrates three classes of such designs where the confinement in the transverse plane (x, y) is provided by RF electrodes, and DC electrodes are segmented to allow confining along the z axis.

Three- and two-layer traps (Fig.2.2 (a) and (b)) present symmetric trapping configurations in the sense that ions are confined between the electrodes. In such symmetric designs, there is more flexibility of the orientation of laser beams (Section 2.2.2) in comparison with asymmetric traps. Three-layer designs provide

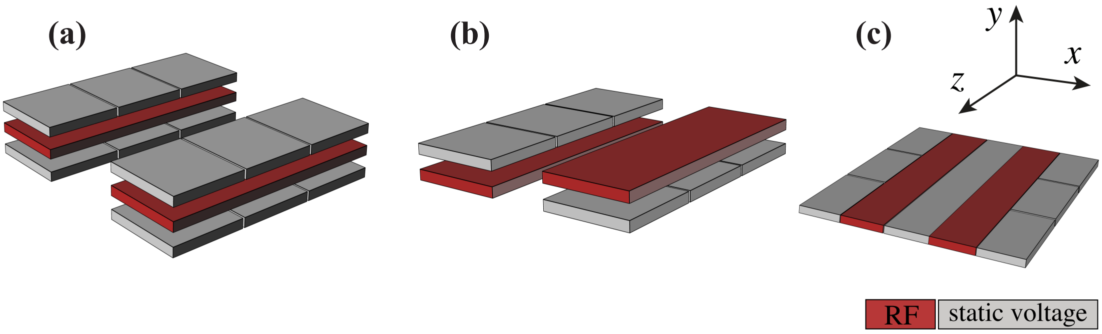

Figure 2.2: Schematics of different linear trap geometries. (a) A three-layer design with segmented DC electrodes surrounding the RF electrodes. (b) A two-layer design where the RF and DC electrodes are diagonally opposite. (c) A surface-electrode design in which all the electrodes reside in one plane.

better control over static trapping fields which is suitable for the compensation of stray fields as well as shuttling. Two-layer designs feature the highest trapping stiffness as compared to three- and single-layer designs with the same ion-to-electrode distance [85, 122].

Figure 2.2 (c) shows a single-layer design, referred to as a surface-electrode (SE) trap, where all the electrodes lie in a single plane and confining fields are generated above the electrode surface [87]. This asymmetric trap geometry is particularly important for several applications. The focus in this study is on the development of such linear SE ion-trap devices, which are discussed in detail in the following.

2.2 Surface-electrode ion traps

SE traps (Fig. 2.3) feature a number of advantages. First, this type of trap architecture offers great scalability which is important for large-scale quantum computation and shuttling of ions [86]. One of the key advantages is that SE structures exhibit enormous flexibility to be patterned, and thus are suited for complicated electrode geometries required [123] (Chapter 5). In addition, SE traps benefit from high-precision fabrication techniques [85] (Chapter 6). The open geometry of the trap provides wide access to the trap centre. Thus SE traps show potential to be integrated with other useful on-chip components.

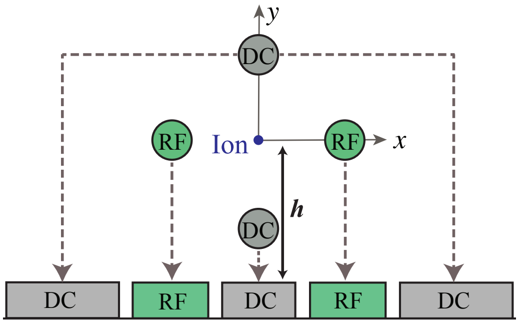

Figure 2.3: Projection of the electrodes of a linear Paul trap to a surface-electrode trap where all the electrodes lie in a single plane and ions are trapped at a certain height h above the surface.

These features make SE traps a superior choice for some new experiments as demonstrated in this work.

2.2.1 Trapping potential for single-layer geometries

In SE traps, ions are confined at a certain height above the surface of electrodes called the trapping height, and this must coincide with the position of the RF null line in order to avoid excess micromotion. The height of the RF null line for a given design depends only on the width of the RF electrodes and the distance between these two [124] (Fig. 2.3). SE quadrupole traps, with translational symmetry along the trap axis, are usually realised in the form of four-, five-, and six-wire designs (Fig.2.4 (a-d)).

General characteristics of trapping potentials can be obtained using analytical calculations [114, 124, 125]. However, analytical calculations [114, 124, 125] are subject to a set of approximations called the "gapless plane approximation"(Section 2.6.1). Therefore, solutions of the Laplace equation for SE traps are calculated numerically. The accurate model of the trapping potential is required for the determination of the secular frequencies, the trap depth and height.

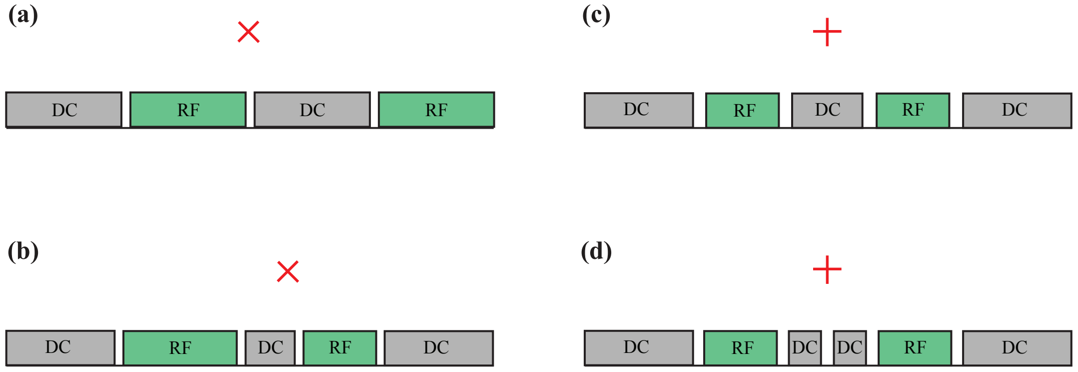

Figure 2.4: Cross-section in the xy plane for different SE traps. (a) Four-wire design in which the principal axes are intrinsically tilted with respect to the vertical direction. (b) Five-wire design with different RF-electrode widths which leads to the intrinsic rotated axes. (c) Five-wire design where RF electrodes are symmetric and one principal axis is perpendicular to the surface. (d) Six-wire design with a split central electrode where one principal axis perpendicular to the surface.

2.2.2 Orientation of the principal axes

To efficiently laser cool ions, the k-vector of the cooling beam must have a component along all three principal axes of the trap [126]. In SE traps, laser beams are commonly aligned parallel to the surface. The purpose of this is to avoid producing photoelectrons and scattered light which affect the florescence detection and build-up charges on exposed dielectrics. In this way, laser cooling beams have no projection along the vertical axis y.

To address this issue, the principal axes are oriented either using asymmetric geometries of electrodes (Fig.2.4 (a-b)) or asymmetric settings of static potentials (Fig.2.4 (c-d)). In 5-wire designs with symmetric RF electrodes (Fig.2.4 (c)), static voltages applied to DC electrodes are used to tilt the principal axes. In addition, the central electrode between the two RF ones shown in Fig.2.4 (c) can be split into two as in Fig.2.4 (d) in order to provide more degrees of freedom for designing static voltages and thus tilting the trap axes [127]. A method for calculating static voltages for a desired tilt angle is detailed in Section 3.1.3.

As a result of the orientation of the principal axes, the motion of ions are coupled and the stability regions are modified. However, it has been shown that the primary stability region is insensitive to the change of the principal axes orientation, and particularly in case of fourty-five degree tilt, this region is even larger [113]. Based on this investigation, stability diagrams of classical Paul traps can be safely used for other traps with a relative angle between RF and DC principal axes.

2.2.3 Trap asymmetry and anharmonicity of trapping potential

An evident consequence of the lack of symmetry in SE traps is a considerable deviation of the trapping potential from the harmonic behaviour [115]. As illustrated in Fig. 2.5, the intrinsic asymmetry of the trap geometry manifests itself in large odd-order terms in the trapping potential. Another source of anharmonic terms in the potential is the miniaturisation of the trap geometry. For a given trap with a characteristic length l, the n-th order term in the potential scales with l^{-n+2} [115]. The Coulomb interaction between ions in a trap introduces significant anharmonicities [128, 129]. Therefore, anharmonicity effects should be taken into account when investigating ion Coulomb crystals in miniaturised SE traps.

Anharmonicities in the trapping potential cause a number of disadvantages. These effects can be realised in two regimes, weak and strong [115]. The former leads to the modification of the amplitude and frequencies of normal modes of trapped ions, while the latter gives rise to amplitude-dependent shifts of trapping frequencies. Anharmonic terms of the trapping potential can cause instabilities [130], as well as non-linear resonances [131, 132] which result in the loss of ions, and consequently, incorrect measurements of reaction rates [131]. Other causes are heating ions due to the operation in the non-adiabatic regime, as well as adverse effects on the effective trapping depth [51, 133].

Anharmonicities can be introduced deliberately using tailored control fields to engineer ion crystals with special properties [134, 135]. These can be also employed to selectively address transitions and coherently control the motional mode of ions [136, 137].

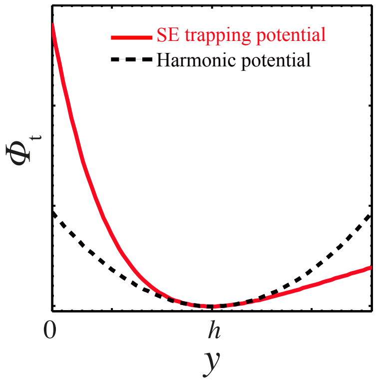

Figure 2.5: A schematic plot of an anharmonic potential generated by an SE trap highlighting the contribution of odd-order terms, in particular y^3. The dashed line shows a harmonic potential yielding the same secular frequency at the trapping height h above the surface.

2.3 Multipole traps

Multipole traps feature a large field-free volume which is of significant practical importance for cold reaction studies [51, 138]. A $2N$-pole trap consists of $2N$ conductive narrow rods equally spaced around a cylinder of radius ρ_0 at angular position of $m\pi/N$, where m is an integer number. A RF voltage $V = V_{\mathrm{RF}}\cos(\Omega_{\mathrm{RF}}t)$ with opposite polarity applied to adjacent rods is used. For infinitely long cylindrical configurations, the solutions of the Laplace equation in the plane polar coordinates (ρ, θ) gives rise to the following field near the axis of the cylinder [51]:

$$\Phi_{\mathrm{RF}}(\rho,\theta) = V_{\mathrm{RF}}(\frac{\rho}{\rho_0})^N\cos(N\theta)\cos(\Omega_{\mathrm{RF}}t). \tag{2.27}$$

Evidently, for $N > 2$ the equation of the ions' motion is not linear, in contrast to the quadrupole field, and hence, x and y motional modes are coupled. However, the general behaviour of trapping fields can be characterised within the adiabatic approximation. The corresponding pseudopotential (Eqn. 2.21) is written as:

$$\Phi_{\mathrm{ps}} = \frac{qV_{\mathrm{RF}}^2}{4m\Omega_{\mathrm{RF}}^2}\frac{N^2}{{\rho_0}^2}(\frac{\rho}{\rho_0})^{2N-2}. \tag{2.28}$$

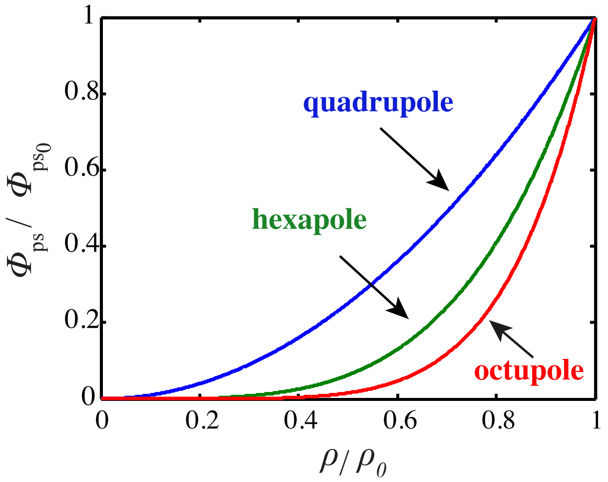

Figure 2.6: Comparison of normalised pseudopotentials for quadrupole, hexapole, and octupole fields.

The key advantage of a multipole over a quadrupole trap is that it provides larger RF-field free regions. For this reason, a 22-pole trap has been widely used for ion-neutral collision studies at low kinetic energies [138]. The effective trap depth of multipole traps does not scale with N^2 as it depends on the adiabacity regime of the trap operation [133]. Furthermore, a recent theoretical investigation showed that buffer-gas cooling of a single ion beyond the critical mass ratio is achievable using multipole RF traps [139].

An octupole trapping potential is particularly suitable for experiments with cold molecular ions for a number of reasons: (1) as discussed above, it exhibits a large field free region (Figure 2.6). (2) For simultaneous confinement of two ionic species with relative mass ratio < 100, the safe value of the adiabacity parameter is best reached with an octupole (i.e., $N = 4$) [51]. (3) It has been predicted that laser-cooled atomic ions in an appropriate octupolar potential form Coulomb crystals[4] [140]. Thus, techniques based on the fluorescence detection could be used to characterise pure and bicomponent crystals [141]. Intriguing features of such crystals could be investigated for applications in quantum computation and quantum simulation.

It is important to develop chip-based multipole traps in order to benefit

---

[4] The conditions for the Coulomb crystalisation is described in Section 1.2.1.

from advantages of miniaturised traps. A 22-pole ion trap based on a two-layer glass chip was demonstrated in Ref. [142]. However, for the reasons discussed in Section 2.2, we aimed to employ SE structures to generate multipole fields (Section 5.4). Analytical calculations show that the stiffest possible SE multipole is much weaker than the stiffest possible three-dimensional multipole of the same order with the same ion-to-electrode distance [124]. Moreover, the broken symmetry in these traps results in much less intrinsic trap depth (Section 5.4.1).

2.4 Two-dimensional ion-trap arrays and junction architectures

Two-dimensional ion-trap arrays were originally proposed as a promising platform for large-scale quantum information processing [3, 86]. Towards this goal, linear and two-dimensional multizone trap arrays were developed to enable transporting, separating and reordering of ions [90, 143–146]. Ion-trap arrays can refer also to ion-trap lattices designed for quantum simulations [94, 123, 147] as well as to ring-shaped ion-trap arrays [148–150]. In the present study, two-dimensional ion-trap arrays are employed to enable the integration of several experiments on a monolithic chip device (Chapter 5).

The key ingredient for developing such an ion-trap network is junctions. Usually a junction is thought of as a connection between identical trap arrays, e.g., a cross between four quadrupolar channels (Fig. 2.7 (b), Fig. 2.8 (b), and Section 5.3). In addition, a junction can be seen as an element that enables the modification of trapping fields between two different channels, e.g., a quadrupole-to-octupole junction (Section 5.5). Moreover, these field-modifying junctions can be used for the separation of a single-harmonic well into a double well trapping configuration [151]. In analogy to the classification used in Section 2.1.4 for miniaturised traps, junctions are broadly divided into three categories: three- and two-layer, as well as surface-electrode (SE) junctions.

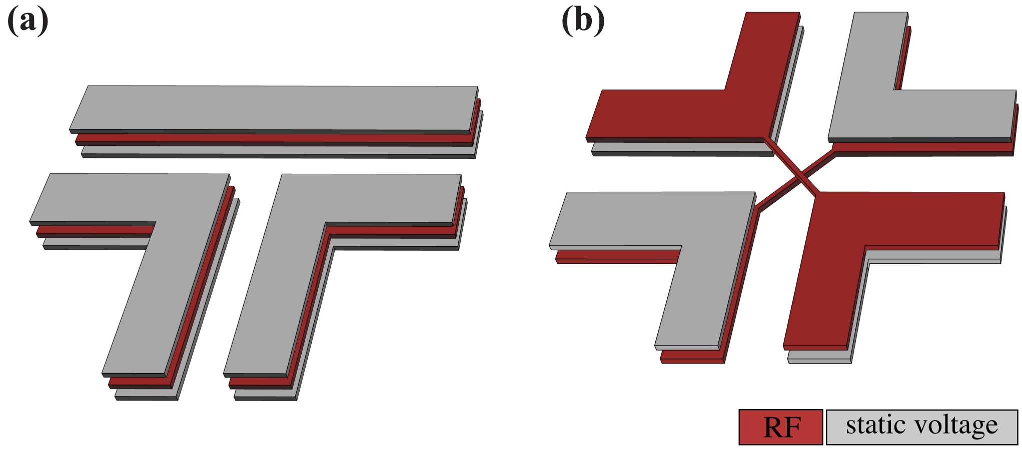

Figure 2.7: Schematics of the three-dimensional junctions that have been used for the successful transport of ions. (a) A three-layer T-junction design [152] used for the first demonstration of corner shuttling of ions as well as swapping of two ions. (b) A two-dimensional X-junction [145] used for highly reliable transport of ions where the ions' kinetic energy was increased by only a few motional quanta. Two diagonal RF bridges (one on the top wafer and the other on the bottom layer) were incorporated at the center of this junction. Adapted from Refs. [145, 152].

2.4.1 Two- and three-layer junctions

In principle, there are many possible configurations for connecting linear arrays of symmetric ion traps (Fig. 2.2 (a-b)). The T- and X-junction structures that have been already used for successful demonstrations of the ion transportation [145, 152] are depicted in Fig. 2.7. These junctions feature simple electrode geometries. In such symmetric designs, the ion channel, which is defined as the position of the pseudopotential minima, is at the geometrical centre of the cross-section of these structures. The axial component of the RF field at these ion channels does not vanish and causes pseudopotential barriers along ion paths (Section 5.2.3) and ion heating [145].

There is a subtle distinction between three- and two-layer junctions concerning the pseudopotential confinement at the intersection centre. Three-layer structures provide a confining pseudopotential at the center of the intersection in both T- (Fig. 2.7 (a)) as well as X-configurations (not shown here). By contrast, two-layer junctions suffer from a lack of harmonic pseudopotential confinement at the centre [153]. To address this issue, two RF bridges were incorporated into the two-layer cross junction demonstrated in Ref. [145] (Fig. 2.7 (b)). As a result, the bridged version of a two-layer junction behaves similarly to a three-layer junction [153]. Both designs (Fig. 2.7 (a,b)) exhibit pseudopotential barriers along their arms. In the X-junction, the height of pseudopotential barriers was found not to be strongly dependent on the width of these RF bridges[5] [154].

As a technical advantage, the number of control electrodes required for a two-layer design is half of that needed in a three-layer junction to achieve the same number of trapping zones, and thus the same level of control on the shuttling process. For this reason, two-layer junctions are preferred in practice [153].

2.4.2 Surfece-electrode junctions

Surface-electrode (SE) junctions are designed with all electrodes residing on a single plane. Such designs offer significant flexibility in terms of the electrode structure and can benefit from high precision fabrication techniques. In fact, the capabilities of SE traps, discussed in Section 2.2, are transferred to SE junctions.

The main challenge to the use of SE junctions arises from the fact that the lowest-order multipole component of the RF field at the centre of a given intersection is a hexapole term [155]. This hexapolar potential is determined by the tangents of the intersecting channels. Therefore, the straight RF electrodes intersecting at right angles do not provide any pseudopotential confinement perpendicular to paths because of field cancellation. The pseudopotential at the center becomes stiffer as the angle between straight arms reduces and also as the number of intersecting channels decreases. For this reason, SE Y-junctions (Fig. 2.8 (a)) are preferred to SE X-junctions (Fig. 2.8 (b)).

Figure 2.8 schematically illustrates two types of SE junctions which have been successfully tested. SE Y-junctions have first been realised in a state-of-the-art chip trap integrating 150 trapping zones[6] [90]. Such junctions were also employed for the shuttling process with a low gain of the ions' kinetic energy [156, 157]. Recently, more efforts have been invested on developing SE

---

[5] Note that this contrasts the case studied in Section 5.3.3 where one DC bridge was incorporated to a surface-electrode junction.

[6] During the shuttling of ions continuous laser cooling was required in this junction.

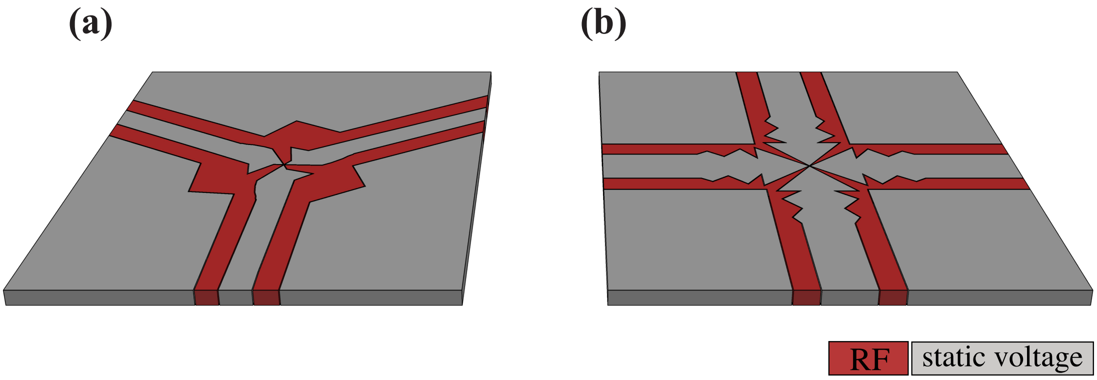

Figure 2.8: Schematics of the two-dimensional junctions that have successfully been tested. (a) A Y-junction used to demonstrate the transport of ions through a surface-electrode junction [90]. (b) A cross junction used for demonstrating transport of ions through a ninety-degree surface-electrode geometry [158]. Adapted from Refs. [90, 158].

X-junctions, resulting in successful demonstrations as well as new techniques for better control over the shuttling process [158, 159].

One of the key elements for these achievements is the optimisation of the junction geometry. The straight RF electrodes at the vicinity of the intersection center must be shaped such that the corresponding pseudopotential exhibits confinement along the direction perpendicular to the surface. To achieve this, the geometry of the RF electrodes is parametrised and the optimal design is computed using an optimisation process which yields the highest value of defined merit functions (Section 5.2).

The position of ion channels in SE junction designs drastically varies as function of the RF electrode geometry as a consequence of the asymmetric configuration. Thus the design of the geometry involves a simultaneous search for the height of ion channels as well as minimisation of the pseudopotential barriers along these channels.

2.5 Ion beam guides

A linear RF multipole is a ubiquitous tool for mass spectrometry, and can be modified into an ion beam guide that is employed to transport ions from a source to an analyser. Such devices are combined with other instruments to enable higher precision and sensitivity required in reaction studies, thermochemistry, and mass spectrometry [160–162]. For instance, an octupole ion guide [163] or a time-of-flight (TOF) mass spectrometer [164, 165] can be combined with a Paul trap. Another important instrument is a guided ion beam tandem mass spectrometer which has been developed to allow precise control over the kinetic energy of reactants in reaction and collision studies [160]. These machines typically consist of a series of quadrupole and multipole traps, as well as ion guides embedded in vacuum chambers and must be manually adjusted. The problem of mechanically adjusting such large machines can be addressed using precisely shaped trapping potentials using a monolithic chip device. The flexibility of electrode structures in SE traps allows the construction of such a multifunctional chip where ions can be guided through precisely-formed ion channels (Chapter 5).

2.6 Numerical methods

2.6.1 Ion trap modelling

Electrode-basis-function technique

A key concept for the simulation of the trapping potential in any arbitrary complex ion-trap device is the "electrode basis function" [166]. In this technique, a desired electric potential generated by a given configuration of voltages is formed as a linear combination of electrode basis functions of the trap.

The electric potential for a given electrostatic configuration with Dirichlet boundary conditions is expressed by [167]:

$$\Phi(x) = \frac{1}{4\pi\epsilon_0}\int_V \rho(x')G(x,x')dv' - \frac{1}{4\pi}\oint_S \Phi(x')\frac{\partial G(x,x')}{\partial n'}ds'. \tag{2.29}$$

The first term is an integral over the interior volume of the boundary with the appropriate Green's function $G(x,x')$ [167]. Because there is no discrete or continuous charge distribution inside an empty trap, i.e., $\rho(x') = 0$, this term vanishes. The second term is an integral over the surface of electrodes

$\Phi(x')$ multiplied by the derivative of the Green's function with respect to the outward normal to the boundary surface n'. Because of the linearity of the Laplace equation, the potential on the trap electrodes can be written as a sum of potentials on each individual electrode while all other electrodes are grounded:

$$\Phi(x') = \sum_{i}^{N} \Phi_i(x'). \tag{2.30}$$

Here, i denotes the electrode index and N is the number of the electrodes and boundaries that are involved in the problem. By substituting this into Eqn. 2.29, one obtains:

$$\Phi(x) = -\frac{1}{4\pi} \sum_{i}^{N} \oint_{S_i} \Phi_i(x') \frac{\partial G_i(x, x')}{\partial n'_i} ds'_i. \tag{2.31}$$

Therefore, the total electric potential is given as a sum of the potentials generated by each individual electrode when all other electrodes and boundaries are held at zero. The voltage applied to each electrode V_i is constant over the electrode surface, therefore Eqn. 2.31 is rewritten as:

$$\Phi(x) = \sum_{i}^{N} -\frac{V_i}{4\pi} \left(\oint_{S'} \frac{\partial G(x, x')}{\partial n'} ds' \right)_i = \sum_{i}^{N} V_i \Theta_i, \tag{2.32}$$

where

$$\Theta_i(x) = -\frac{1}{4\pi} \oint_{S'} \frac{\partial G(x, x')}{\partial n'} ds'. \tag{2.33}$$

$\Theta_i(x)$ is referred to as the electrode basis function of the ith electrode representing the electric potential that is generated by the ith electrode held at 1 volt when all other electrodes are grounded.

Strictly speaking, this formalism is valid only for time-independent voltages. However, it can be extended to the time-varying potential used in RF ion traps considering the range of voltages typically applied in experiments [166]. The time-varying field in a typical RF trap is in the megahertz range associated with wavelengths much larger than the size of ion traps ($\approx 10^{-2}$ m). Therefore, the entire trapping potential can be formulated based on electrode basis functions where the time-dependent potentials are simply treated as $V_i = V_{\mathrm{RF}}\cos(\Omega_{\mathrm{RF}} t)$, where V_{RF} and Ω_{RF} are the amplitude and frequency of the RF voltage applied to the electrodes. This is useful when accounting for micromotion effects is required (Section 2.6.2). In addition, electrode basis functions are used to obtain the potential energy of ions within the adiabatic approximation (Section 2.1.2).

$$\begin{aligned}\Phi_{\mathrm{t}}(x,y,z) &= \Phi_{\mathrm{ps}} + \Phi_{\mathrm{DC}} \\ &= \frac{q^2 V_{\mathrm{RF}}^2}{4\ m\Omega_{\mathrm{RF}}^2}\,\|\nabla\ \Theta_{\mathrm{RF}}\|^2 + q\sum_i^n V_i\Theta_{\mathrm{DC},i},\end{aligned}$$

where m and q are the mass and charge of the trapped ions, respectively, and n is the number of the DC electrodes.

Numerical methods for computing basis functions

Electrode basis functions for a given complex trapping architecture are calculated numerically. Two- and three-layer miniaturised traps are necessarily treated with numerical methods: finite element methods (FEM) or boundary element methods (BEM)[7]. SE traps can benefit from analytical calculations based on the following treatment, and full numerical calculations using FEM or BEM additionally serve to provide an accurate description. This can be seen as an advantage enabling the implementation of large calculations required for optimisation of complicated SE structures (Chapter 5).

The mathematical tool for analytical calculations of the field resulting from an arbitrary planar charge distribution is provided by a Biot-Savart-like integral [168]. Thus, the electric potentials associated with surface electrodes are calculated analytically [114, 124, 169] whilst three assumptions are made: the gaps are infinitely small as well as thin, i.e., there are no finite gaps between surface electrodes, and electrodes cover an infinite plane, i.e., they are surrounded by an infinitely large grounded plane. This set of assumptions is referred to as "gapless plane approximation" and is used as the basis for the models presented by Wesenberg, Schmied, and House [114, 124, 169]. Such calculations

---

[7] Finite difference methods (FDM), offered by, e.g., *SIMION*, is not suitable for potential modelling for miniaturised traps due to its limited meshing method, and thus, is not discussed here.

can be performed using the *Mathematica* package *SurfacePattern* [123, 169] to model and optimise arbitrary patterns of electrodes residing on a plane when the solution of the Laplace equation in an electrostatic or magnetostatic systems is required. In most SE ion traps, the usual assumptions of neglecting the influences of gaps between electrodes and the finite electrode extent lead to a negligible modifications on, e.g., trapping frequencies [169]. But this treatment cannot be used for ion channel intersections and mulipole ion channels, and thus alternative methods (i.e., FEM or BEM) are required.

FEM is a powerful, well-established technique for computing the electric potential of a realistic arrangement of electrodes. This method requires the discretisation of the entire boundary-value-problem domain into "mesh" elements. The vertices of these elements are related to each other by a simple linear or quadratic function. The potential is calculated at the vertices following specific algorithms while the boundary conditions are satisfied. These algorithms are classified to two broad categories: direct and iterative solvers. In these calculations, it is crucially important to ensure the convergence of the solutions obtained. The convergence studies verify the following conditions in a given set of calculations:

(1) The solutions must be independent of the fineness, the distribution, and the shape of the mesh elements used. To reduce the discretisation error, usually the size of the mesh is decreased which leads to increasingly more computational efforts. Taking advantage of symmetry and strategic meshing help to improve the efficiency of these calculations. As an example, Fig. 2.9 displays a free-tetrahedral mesh used to model the SE trap discussed in Chapter 3 where layer meshing was chosen to increase the accuracy of calculations in the region of interest. It is worth noticing that triangular and tetrahedral meshing are preferable for curved and complex geometries but greater number of vertices are required to reach converged solutions.

(2) The solutions must be independent of the auxiliary boundary conditions applied to the model. The boundary domain resembling the vacuum chamber walls and surfaces surrounding a given trap are typically replaced with a smaller chamber to facilitate the computation. Thus, it has to be proven that the variation of solutions with the size of this domain is reasonably small.

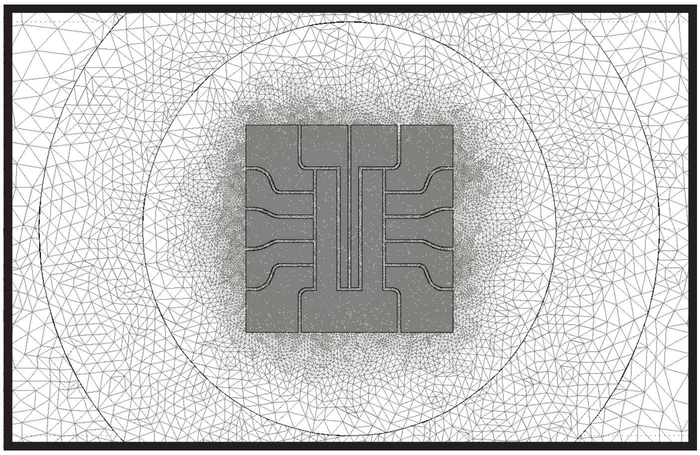

Figure 2.9: Illustration of a free tetrahedral mesh used in finite element calculations for the six-wire SE trap used in this work [104]. A cylindrical layer mesh was used to deliberately reduce the mesh size in the region of interest.

(3) The solutions must be independent of the algorithms employed. The solutions provided by direct solvers are independent of the algorithm, however, this is not the case for iterative solvers and hence must be checked.

FEM features a number of advantages. It is widely applicable to a variety of problems beyond electrostatic, e.g., mechanical stresses or thermal dissipation. More importantly, FEM enables simultaneous modelling of combinations of different effects which is important for the study of combined systems. In addition, complex geometries as well as non-linear material properties can be simulated. There are a number of commercially available software packages for FEM calculations, e.g., *COMSOL*[8], *Maxwell 3D*[9], and *Vector Fields*[10].

BEM is an alternative technique to FEM, where an integral equation formulation is used (similar to Eqns. 2.29-2.32) instead of the relevant differential equation, e.g., the Laplace equation. The surface of electrodes are discretised with mesh elements and the charge density over each element on the surface is found. The solution at a given point in the problem domain is computed by evaluating the integrals representing the contribution of the potential at this point from each charge element on the surface. BEM exhibits two key advantages:

---

[8] COMSOL MultiPhysics, www.comsol.com

[9] Maxwell 3D, by Ansoft, http://www.ansoft.com

[10] http://www.vectorfields.com

first, the potentials obtained are continuous functions because the discretisation occurs on boundary surfaces. Second, considerable improvement in the computational efficiency is offered owing to the reduction of the dimensionality from a volume in FEM to a surface in BEM. By increasing the number of trapping zones in large arrays and the total size of the trapping device, it becomes crucial to employ an efficient method amenable in terms of memory requirements and computational time. BEM can be implemented using, e.g., *BEMsolver* [170] or commercially available software packages, e.g., *CPO* [11].

2.6.2 Molecular dynamics simulations

Molecular-dynamics (MD) simulations [171, 172] have been widely used for theoretically studying Coulomb crystals in Paul and Penning traps [173–177], for instance, for the characterization of the structure and energy of ions in a trap. Here, we describe this technique and discuss its adaptation to SE traps since it has been employed as a key tool in this work. The routines were implemented in the MD framework ProtoMol [178].

In this treatment, the following classical equations of motion for the laser- and sympathetically cooled ions are solved:

$$\begin{aligned} m_i\ddot{\mathbf{r}}_i &= \mathbf{F}_{i,\mathrm{Total}}(\mathbf{r}_1, ..., \mathbf{r}_{\mathrm{N_{atoms}+N_{molecules}}}) \\ &= \mathbf{F}_{\mathrm{Trap}} + \mathbf{F}_{\mathrm{Coulomb}} + \mathbf{F}_{\mathrm{Heating}} + \mathbf{F}_{\mathrm{LC}}. \end{aligned} \tag{2.34}$$

Here, m_i and $\mathbf{r}_i$ are the mass and the position of the ith ion, respectively, and $i = 1, ..., N_{\mathrm{atoms}} + N_{\mathrm{molecules}}$ where N_{atoms} and $N_{\mathrm{molecules}}$ denote the number of the atomic and molecular ions, respectively. The contributions to the total force, as expressed by Eqn. 2.34, are: the trapping force $\mathbf{F}_{\mathrm{Trap}}$, the Coulomb force between ions $\mathbf{F}_{\mathrm{Coulomb}}$, a heating force $\mathbf{F}_{\mathrm{Heating}}$, the laser cooling force $\mathbf{F}_{\mathrm{LC}}$ [173]. The first three terms act on both the atomic and molecular ions whilst the last term acts only on the atomic ions. The sympathetic cooling is provided by the Coulomb interactions between the ions.

In this study, heating effects arising from collisions with background gas

---

[11] Charged Particles Optics, by Electronoptics, http://www.electronoptics.com

molecules and imperfections of the setup are modelled as random force kicks on the ions. The Doppler laser cooling force is modelled as a friction force [52],

$$\mathbf{F}_{\mathrm{LC},z} = \mathbf{F}_{\mathrm{RP},z} - \beta \mathbf{v}_z. \tag{2.35}$$

The velocity-independent term $\mathbf{F}_{\mathrm{RP}}$ stands for the radiation pressure force. The z index emphasizes the one-dimensional friction model. β is determined based on the parameters used in experiments, given by:

$$\beta = -\hbar k^2 \frac{4 s_0 (\delta/\gamma)}{(1 + s_0 + (2\delta/\gamma)^2)^2}. \tag{2.36}$$

Here, γ is the natural linewidth of the atomic transition, δ is detuning from the atomic resonance, k is the wavevector of the laser beam, and s_0 is the saturation parameter (defined by $2|\Omega|^2/\gamma^2$ where Ω is the Rabi frequency). This linear approximation of the laser-cooling force has been frequently used in MD treatment of trapped ions [173, 174, 176].

The trapping force dominates the properties of Coulomb crystals in a given trap through the geometrical as well as operational trapping parameters. The trapping force in case of linear Paul traps is given simply by the analytical gradient of the RF and static potentials given in Eqns. 2.1 and 2.3. To calculate the trapping force generated by a given SE trap, $\mathbf{F}_{trap}$ in Eqn. 2.34, three different approaches are considered.

In the first approach, the A and Q matrices (Section 2.1.2) are derived from a numerical model of the trap (e.g., computed using FEM), and the trapping force is formulated as:

$$\mathbf{F}_{\mathrm{Trap-AQ}}(x, y, z, t) = \frac{m\Omega_{\mathrm{RF}}^2}{4} \sum_{i=x,y,z} \Big(A_{ii} + 2Q_{ii} \cos(\Omega_{\mathrm{RF}} t) \Big) \mathbf{x}_i. \tag{2.37}$$

This method is straightforward to implement, however, it assumes that RF and static trapping potentials near the centre are fully described by second-order terms, i.e., it neglects higher order terms.

Second, the analytical solutions of the potential offered by Refs. [114, 124, 179] are used. This is an advantageous method because the force, computed as the analytical gradient of potentials, is not approximated to second-order terms and includes all higher-order and cross terms,

$$\mathbf{F}_{\mathrm{Trap-Ana}}(x,y,z,t) = -\nabla\left(V_{\mathrm{RF}}\cos(\Omega t)\phi_{\mathrm{RF}} + \sum_{i=1}^{n} V_i\phi_{\mathrm{DC}}\right). \tag{2.38}$$

Here, ϕ_{RF} and ϕ_{DC} are the RF and DC electrode basis functions, and n is the number of control electrodes, respectively. Note that the validity of the gapless plane approximation made to compute the trapping potential (Section 2.6.1) has to be verified to enable comparisons with experimental results.

In the third approach, the electrode-basis functions of the SE trap obtained from numerical calculations are fitted to a three-dimensional power series expansion of both static and RF potentials near the trap center (x_0, y_0, z_0). The expansion of trapping potentials is used to calculate the trap force $\mathbf{F}_{\mathrm{Trap}}$:

$$\begin{aligned}\mathbf{F}_{\mathrm{Trap}}(x,y,z,t) = -\nabla\Bigg(& V_{\mathrm{RF}}\cos(\Omega t)\sum_{k,l,m} C_{\mathrm{RF}_{(k,l,m)}}(x-x_0)^k(y-y_0)^l(z-z_0)^m \\ & + \sum_{i=1}^{n} V_i \sum_{k,l,m} C_{\mathrm{DC},i_{(k,l,m)}}(x-x_0)^k(y-y_0)^l(z-z_0)^m\Bigg).\end{aligned} \tag{2.39}$$

$C_{\mathrm{RF}_{(k,l,m)}}$ ($C_{\mathrm{DC},i_{(k,l,m)}}$) is the coefficient of the (k,l,m)-th order term in the RF (ith DC electrode) potential. In the simulations presented for the six-wire SE trap in Chapter 4, the coefficients C_{RF} and C_{DC} were obtained from fits to a series expansion truncated at 4-th order in a 400 μm cube around the trap center using FEM calculations to obtain the electrode basis functions (Section 4.5).

As expressed by Eqn. 2.39, the fully time-dependent trapping force was used in our simulations to enable the characterisation of micromotion effects [108]. To give an example, the integration time step in the simulations presented in Section 4.2 was 4.2 ns (=1/30 RF period, $\Omega_{\mathrm{RF}}=2\pi\times8.0$ MHz) while the typical simulation time interval was 3.75 ms. Note that the equilibrium position of ions, structural properties, and structural phase transitions crystals can adequately be modelled within the pseudopotential approximation [117, 173].

The ion trajectories obtained from the simulations are used to reconstruct the experimental images using a *MATLAB* routine. Figure 2.10 depicts an example

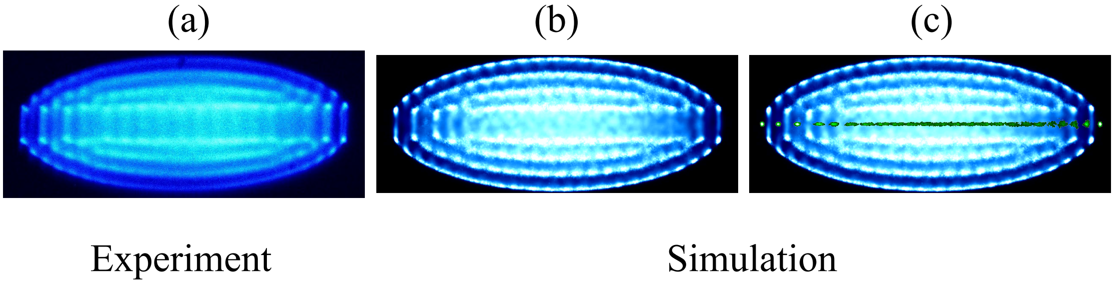

Figure 2.10: (a) Experimental and (b,c) simulated false-colour fluorescence images of a $Ca^{+}{-}N_2^{+}$ Coulomb crystal in a linear Paul trap. The crystal contains 25 sympathetically cooled N_2^{+} and 950 Ca^{+} ions. In (c), the sympathetically cooled molecular ions were made visible in the simulations for clarity. Colour code: Ca^{+}: blue, N_2^{+}: green.

of an experimental fluorescence image taken by a charge-coupled device (CCD) camera from a $Ca^{+}{-}N_2^{+}$ bicomponent Coulomb crystal in a linear Paul trap and the corresponding MD simulations [180]. An iterative comparison between the experimental and simulated images is used to determine the ion numbers and average kinetic energies in the experiments [54, 60, 173, 180].

The secular temperature of the ions has a strong effect on the diffusion behaviour of the ions in the crystals and therefore on the contrast of the crystal structure observed in the images. The secular temperature of the ions in the experiment was determined by adjusting the temperature in the simulations through varying the magnitude of the heating force $\mathbf{F}_{\text{Heating}}$ in Eqn. 2.34 until the best match between the experimental and simulated images is reached. The averaged total kinetic energies of ionic species (including the secular and micromotion energies) are subsequently derived from the ion trajectories [173].

A recent study [177] has addressed the simplifications made for modelling the cooling and heating mechanisms described in this section. There, the laser cooling force is modelled as the interaction of a two-level atomic system with near-resonant light using the optical Bloch equations. Furthermore, collisions of single ions with background gas molecules is realistically modelled as infrequent energetic collisions resulting in considerable heating of the entire ion clouds and time-dependent secular temperatures. Hence, the equation to be employed in realistic MD simulations is expressed as [177]:

$$m_i \ddot{\mathbf{r}}_i = \mathbf{F}_{\text{Trap}} + \mathbf{F}_{\text{Coulomb}} + \mathbf{F}_{\text{Background}} + \mathbf{F}_{\text{Scattering}}. \tag{2.40}$$

In conclusion, the MD-simulation results presented in this work, provide a precise estimation for the determination of the number of trapped ions as well as their spatial distribution. The reason is that the equilibrium positions of ions in a trap is independent of cooling and heating mechanisms and solely depend on the Coulomb interaction and the trapping force. However, the calculations performed give an upper limit for the kinetic energy of ions due to the assumptions made for thermalizations of ions.

Chapter 3

The six-wire surface-electrode ion trap

The present chapter describes the technical aspects of the development of the six-wire SE ion trap used for the first successful demonstration of the Coulomb crystalisation of molecular ions in a single-layer ion trap (September 2013) [104]. The design of the trap and detailed theoretical characterization of the trapping potential are presented. The entire experimental apparatus was conceived, designed, and implemented as a part of this work and therefore an insight is provided into the experimental tools and techniques that are integral in achieving the results demonstrated in Chapter 4.

3.1 Design of the trap

3.1.1 The geometry

Inspired by Ref. [181], we adopted a six-wire surface-electrode (SE) ion trap consisting of a split central electrode, two RF electrodes, six control electrodes, four endcap electrodes and two central electrodes as illustrated in Fig. 3.1. The RF electrodes were used to generate time-varying electric fields for the dynamic trapping of the ions in the transverse (x, y) directions (Section 2.2.1), and all other electrodes were used to apply static voltages. The static potentials served to confine the ions in the longitudinal direction z (the symmetry axis of the

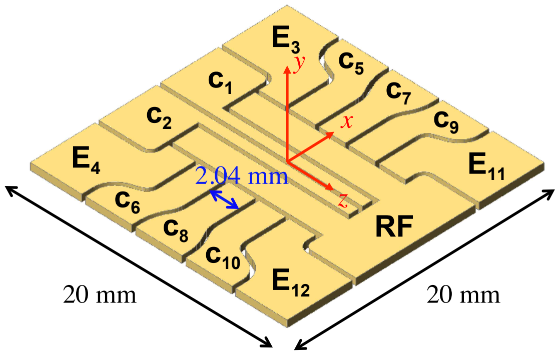

Figure 3.1: A schematic of the six-wire SE trap. RF: RF electrodes, 1,2: central DC electrodes, E: endcap electrodes, c: control electrodes. The DC electrodes are numbered from 1 to 12.

trap), to tilt the principal axes of the trap for efficient laser cooling of the atomic ions if required [181], to compensate excess micromotion [108] and to shape the trapping potentials in order to manipulate the structure of the Coulomb crystals [121]. The trap geometry was refined using the analytical model described in Ref. [114]. The nominal width of the RF and central electrodes amounted to 2.00 mm and 0.75 mm, respectively. The gaps between the electrodes has a nominal width of 0.30 mm.

3.1.2 Trapping potential modelling

The electrode potentials were calculated by solving the Laplace equation for a three-dimensional model of the trap using FEM implemented in the COMSOL Multiphysics software [182], as well as using an analytical model offered by the *SurfacePattern* package [123, 169, 179]. Within the adiabatic approximation, the total effective trapping potential Φ_t experienced by the ions is given by the sum of a time-independent pseudopotential Φ_ps and a static potential Φ_DC

generated by the trap electrodes (Section 2.2.1):

$$\begin{aligned}\Phi_{\mathrm{t}}(x,y,z) &= \Phi_{\mathrm{ps}} + \Phi_{\mathrm{DC}} \\ &= \frac{q^2 V_{\mathrm{RF}}^2}{4\, m\Omega_{\mathrm{RF}}^2}\, \|\nabla\ \phi_{\mathrm{RF}}\|^2 + q\sum_{i}^{12} V_i \cdot \phi_{i,\mathrm{DC}}.\end{aligned} \tag{3.1}$$

Here, q and m are the charge and mass of the trapped ions, respectively, and V_{RF} and Ω_{RF} denote the RF amplitude and frequency, respectively. The potential terms ϕ_{RF} and $\phi_{i,\mathrm{DC}}$ are the solution of the Laplace equation for a unit voltage applied to the RF and the ith DC electrode, respectively. V_i is the voltage applied on the ith DC electrode.

Having computed the electrode basis functions (Section 2.6.1), the voltages required to generate a desired trapping potential must be calculated. The pseudopotential (Section 2.1.2) was calculated at the amplitude and the frequency of the RF voltage which maximised the intrinsic trap depth while keeping the values of the Mathieu stability parameters [108] small for both N_2^+ and Ca^+ (Section 3.1.4). The determination of the voltages to be applied to the DC electrodes, however, necessitates simultaneously considering axialization conditions and the trap strength, i.e., the second derivative of the potential. In the following, the method used to compute the static voltages applied is presented.

3.1.3 Parametrisation

To determine the optimal static voltages to apply to the different DC electrodes, the parametrisation method of Refs. [181, 183] was used. First, the numerically computed electrode basis function of the ith DC electrode $\phi_{i,\mathrm{DC}}$ was fitted to a quadratic function:

$$\Psi_i = \alpha_{xi}x^2 + \alpha_{yi}y^2 + \alpha_{zi}z^2 + \beta_{xi}x + \beta_{yi}y + \beta_{zi}z + C_i. \tag{3.2}$$

Here, α is the quadratic and β is the linear coefficient for each ith electrode. In this way, an array of coefficients representing the confining force associated with a given trap geometry is calculated. The constants C_i are ignored because they have no effect on the present analysis. The expansion can be truncated when the coefficients become negligible, and this strongly depends on the size of the region for which we calculated the above quadratic functions, as well as on the length scale of the surrounding electrodes. If the electrode-electrode and ion-electrode distances are comparable, quadratic terms will usually suffice [183]. For the present trap, three-dimensional least-squares fits were obtained in a 100-μm side-length cube around the trap center.

Second, a particular potential Ψ is specified such that the required form of potential is given by the α and β coefficients:

$$\Psi = \alpha_x x^2 + \alpha_y y^2 + \alpha_z z^2 + \beta_x x + \beta_y y + \beta_z z. \tag{3.3}$$

Hence, an array of potential coefficients corresponding to the desired trap operating condition can be defined as in Table 3.1.

Finally by taking advantage of the linearity of the Laplace equation, the electrode voltages required are given by:

$$\begin{pmatrix} \alpha_x \\ \alpha_y \\ \alpha_z \\ \beta_x \\ \beta_y \\ \beta_z \end{pmatrix} = \begin{pmatrix} \alpha_{x1} & \alpha_{x2} & \cdots & \alpha_{x6} \\ \alpha_{y1} & \alpha_{y2} & \cdots & \alpha_{y6} \\ \alpha_{z1} & \alpha_{z2} & \cdots & \alpha_{z6} \\ \beta_{x1} & \beta_{x2} & \cdots & \beta_{x6} \\ \beta_{y1} & \beta_{y2} & \cdots & \beta_{y6} \\ \beta_{z1} & \beta_{z2} & \cdots & \beta_{z6} \end{pmatrix} \begin{pmatrix} V_1 \\ V_2 \\ V_3 \\ V_4 \\ V_5 \\ V_6 \end{pmatrix}. \tag{3.4}$$

Here, V is an array of independent voltages to be applied to the DC electrodes. As in Ref. [181], the electrodes were classified into six groups in this calculation. As an example, generating an axial secular frequency of 100 kHz for $^{40}\mathrm{Ca}^+$ necessitates the α values shown in the first row of Table 3.1. For the RF voltage $\mathrm{V}_{\mathrm{RF(0-peak)}} = 600$ V and the RF frequency $\Omega_{\mathrm{RF}} = 2\pi \times 8.0$ MHz, the values shown in Table 3.1 result in an estimated tilt angle of 33 °, and secular frequencies of 247 kHz and 306 kHz in the x and y directions, respectively.

Because for experiments with three-dimensional crystals tilting the trap principal axes is not required, a simplified configuration of typical voltages used in the experiments were {central (1,2), control (c), endcap (E) electrodes}={2 to 2.3, -6 to -6.6, 21.5 to 23} V, while maintaining the position of the ions at the

Table 3.1: The coefficients of the potential for four sets of operating bases: set the axial secular frequency at 100 KHz, x- and y-compensation configurations, and tilt the pricipal axes. α is in units of V m^{-2} and β in V m^{-1}. The coefficients in the "tilt" parameters denoted with primes were defined in an alternate coordinate system rotated by 45 ° around the z axis [181].

	β_x	β_y	β_z	α_x	α_y	α_z
Set the axial confinement	0	0	0	-4.12×10^4	-4.12×10^4	8.24×10^4
$\hat{\boldsymbol{x}}$-compensation	1	0	0	0	0	0
$\hat{\boldsymbol{y}}$-compensation	0	1	0	0	0	0
	β'_x	β'_y	β'_z	α'_x	α'_y	α'_z
Tilt the trap axes	0	0	0	-1.04×10^5	1.04×10^5	0

RF null line.

3.1.4 Trapping characteristics

The results obtained from FEM calculations are presented in Fig. 3.2 for ^{40}Ca$^+$ at V_{RF}=495 V, Ω_{RF}=$2\pi\times$8.0 MHz and $V = \{V_1, V_2, ..., V_{12}\} = \{2.35, 2.35, 21.5, 21.5, -6.0, -6.0, -6.6, -6.6, -6.0, -6.0, 23.0, 23.0\}$ V which correspond to typical operating parameters in our experiments. This configuration of static voltages resulted in "axialized" crystals, i.e., the center of the crystal coincided with both the RF null line and the minimum of the static potential Φ_{DC} in order to minimize excess micromotion [108]. The position of the RF null line was calculated to be 1.82 mm above the surface (Fig. 3.2 (c)).

The intrinsic trap depth (Section 2.2.1) is defined using the potential difference between the minimum and the saddle point on the y axis as illustrated in Fig. 3.2 (a). The application of the static potential Φ_{DC} gives rise to the off-center saddle points of Φ_{t} along the x axis providing additional escape routes of ions from the trap (Fig. 3.2 (b)). Thus, the effective trap depth was limited by the escape of the ions through these saddle points, and was calculated to be 117 meV for Ca$^+$. Using the same trapping parameters, the total trapping potential Φ_{t} was also calculated for N$_2^+$, CaH$^+$, and CaO$^+$ ions. Because of the inverse mass dependence of Φ_{ps}, lighter ions experience a stronger confining force

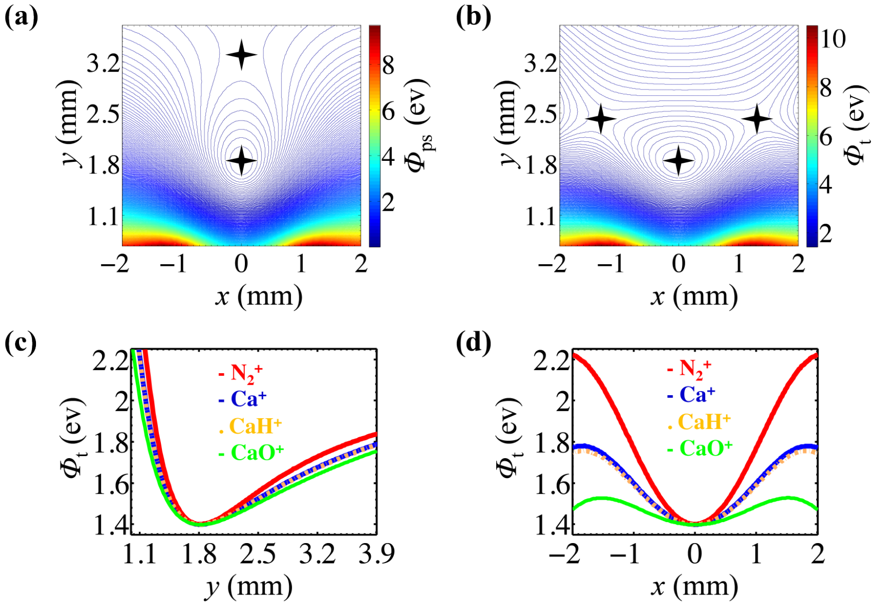

Figure 3.2: Calculated trapping potentials: (a) pseudopotential Φ_{ps} and (b) total potential Φ_{t} for Ca^+ ions in the (x, y) plane intersecting the trap center perpendicular to the trap axis, (c) and (d) one-dimensional cuts through Φ_{t} at the trap center for N_2^+, Ca^+, CaH^+ and CaO^+ along the y and x axes, respectively, illustrating the mass dependence of the trapping potential. See Figure 3.1 for the definition of the coordinate axes.

from the RF field leading to a segregation of ionic species in bicomponent Coulomb crystals (Section 4.1 and Refs. [54, 57, 76]). This situation is completely analogous to the one found in conventional linear RF traps [54]. Figure 3.2 (c) and (d) show one-dimensional cuts of Φ_{t} at the trap center along the y and x-axes for N_2^+, CaH^+, and CaO^+ ions in comparison with Ca^+. For N_2^+ and CaH^+ ions, the effective trap depths were calculated to be 261 meV and 104 meV, respectively. In the presence of static fields, the exact inverse relation between the ion mass and the trap depth is not valid, e.g., $\frac{D_{(\mathrm{N}_2^+)}}{D_{(\mathrm{Ca}^+)}} \neq \frac{m_{(\mathrm{Ca})}}{m_{(\mathrm{N}_2)}}$.

In Table 3.2, the multi-dimensional generalisation of the Mathieu stability parameters [114] (Section 2.1.2) for the present trap calculated for the operating parameters used in the experiments are given. In comparison to linear Paul traps in which $A_{xx} = A_{yy} = -0.5A_{zz}$, the values for the A_{ii} can be more easily engineered in SE traps in order to shape Coulomb crystals. The negative values

Table 3.2: Stability parameters for Ca^+ and N_2^+ calculated at V_{RF}=495 V, $\Omega_{RF}=2\pi\times8.0$ MHz and $V = \{V_1, V_2, ..., V_{12}\} = \{2.35, 2.35, 21.5, 21.5, -6.0, -6.0, -6.6, -6.6, -6.0, -6.0, 23.0, 23.0\}$ V.

	Q_{xx}	Q_{yy}	Q_{zz}	A_{xx}	A_{yy}	A_{zz}
$^{28}N_2^+$	0.1178	-0.1152	-5×10^{-4}	-22×10^{-4}	16×10^{-4}	6×10^{-4}
$^{40}Ca^+$	0.0824	-0.0806	-3×10^{-4}	-16×10^{-4}	11×10^{-4}	4×10^{-4}

of A_{xx} in Table 3.2 imply that the static voltages have effectively reduced the total trapping force in the x direction. $A_{yy} > 0$ yields a tighter trap in the vertical direction y. This effect is generated by the potential of the endcap electrodes which, besides providing confinement along the trap axis ($A_{zz} > 0$), also stiffen Φ_t in the vertical direction and must weaken it along the x axis due to the Laplace equation. As a result, the degeneracy of the radial modes of the ion motion is broken giving rise to non-spheroidal Coulomb crystals [104, 121] (see the crystals in Section 4.1). This is important for shaping Coulomb crystals for potential applications in quantum computation and quantum simulation [119]. Note that the formation of spheroidal crystals in SE traps only depends on the choice of static voltages, e.g., see the examples presented in Section 4.4.3 as well as in Ref.[121].

3.2 Technical implementations

3.2.1 Trap fabrication

The fabrication method of the six-wire SE trap was based on laser cutting the electrodes from a stainless steel foil performed by *Createch AG*[1]. The electrodes were machined into the central part of the foil with the edges still connected as in Fig. 3.3 (a) (i). The foil was sufficiently thick (0.5 mm) in order to suppress vibrations of the free-standing electrodes. The trap was then electro-polished and coated with a layer of gold with a nominal thickness of 2 μm which performed by *RERO AG*[2]. This procedure resulted in removing the chips seen in

---

[1] Gaswerkstrasse 67, CH-4900 Langenthal, Switzerland. www.createch.ch

[2] Hauptstrasse 96, CH-4437 Waldenberg, Switzerland. www.rero-ag.ch

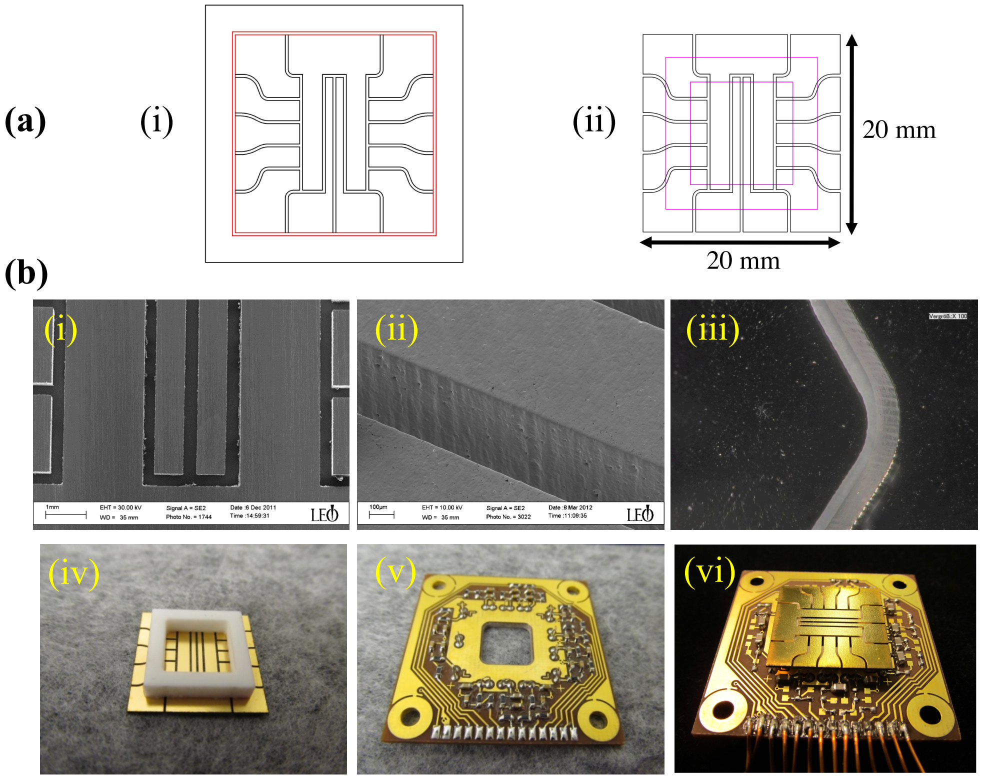

Figure 3.3: Illustration of the trap fabrication procedure. (a) Drawings of the trap geometry showing (i) the electrode pattern at the center while electrodes were connected outside the red rim in and (ii) the second cut while the electrodes had been fixed on the ceramic frame depicted in magenta. (b) (i) A SEM image of the structure after laser cut. (ii) A SEM image of the central gap (between electrode 1 and 2). (iii) An optical microscope image of a corner gap after electro-polishing as well as gold-plating. (iv) A picture of the backside of the structure exhibiting the ceramic frame with 10.5-mm inner width. (v) The PCB board containing the trap electronics with a 10-mm wide square hole at the center. (vi) The finished chip.

Fig. 3.3 (b) (i) from the trenches and providing sharp edges (Fig. 3.3 (b) (ii) and (iii)). Subsequently, the structure was glued onto a ceramic frame with an inner diameter of 10.5 mm (Fig. 3.3 (b) (iv)), and baked at ≈ 80 °C for about two hours to cure the epoxy used (electrically isolating epoxy, *EPO-TEK T7110*).

A second laser cut then removed the rim to separate the electrodes, generating the final geometry of the electrodes as in Fig. 3.3 (a) (ii). The trap and its ceramic mount were glued onto a vacuum-compatible printed circuit board (PCB), provided by *Multi-CB*[3], which contained the trap electronics and was milled out at the center (Fig. 3.3 (b) (v)) to allow backside loading of Ca (Section 3.2.4).

Figure 3.3 (b) (vi) displays the finished chip soldered on the 13 properly curved thin wires connecting electrodes to the filter board. This specific trap layout was chosen in order to avoid any dielectric surfaces in the vicinity of the trap center which could cause the build up of stray charges and patch potentials. This fabrication method was suggested by Iulia Georgescu for a prototype of a five-wire SE trap [184].

3.2.2 Doppler laser cooling of $^{40}\mathrm{Ca}^{+}$

Doppler laser cooling of Ca^{+} ions was achieved by three diode laser beams at 397, 866 and 854 nm addressing the $(4s)^2S_{1/2} \rightarrow (4p)^2P_{1/2}$, $(3d)^2D_{3/2} \rightarrow (4p)^2P_{1/2}$ and $(3d)^2D_{5/2} \rightarrow (4p)^2P_{3/2}$ transitions as depicted in Fig. 3.4 (a). Light at 397, 866 and 854 nm was produced from external cavity stabilized diode lasers (*Toptica Photonics, DL100*, and the later from *DL100 Pro*). A small fraction of the light was coupled to a wavemeter (*HighFinesse, WSU-30*) to determine the wavelength. A fiber switch allowed sequential reading of the wavelength of up to four lasers with a total cycle update rate of ≈ 5 s^{-1}. The wavelength was stabilized to within ± 2 fm by means of a proportional-integral-derivative (PID) feedback loop between the read-out from the wavemeter and the voltage applied to the piezo-electric element of the lasers (which tuned the wavelength by varying the grating angle) via a *LabVIEW* program and a digital-to-analogue-

---

[3] Business Centres, Holyrood Close, Poole BH17 7FJ, United Kingdom. http://www.multi-circuit-boards.eu

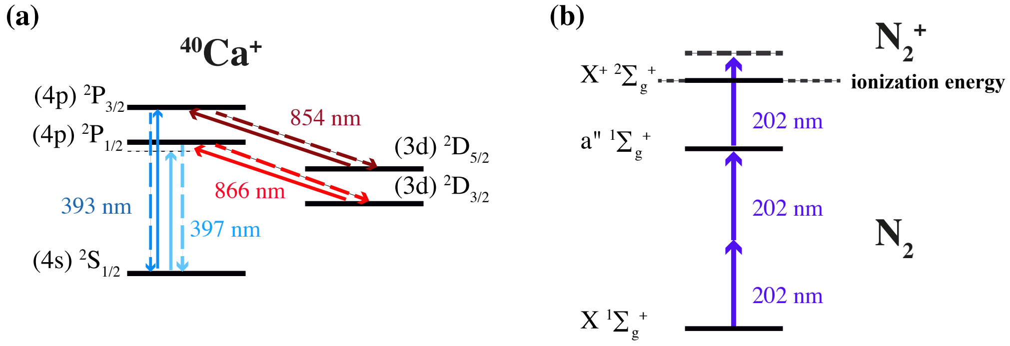

Figure 3.4: (a) Energy-level diagram for Doppler laser cooling and detection of $^{40}Ca^+$. (b) Resonance-enhanced [2+1]-photoioinisation scheme for N_2 to generate N_2^+. The electronic states involved are designated by their spectroscopic labels [176].

converter (DAC) card. In a typical experiment, a power of 0.5 - 1 mW for 397 nm, 0.7 mW for 866 nm, and 1.1 mW for 854 nm (measured at the ports of the vacuum chamber) was used. The 397 nm source was later on switched to a home-build diode laser operating similarly, although with an external laser-diode temperature controller (*Thorlabs, ITC4001*). All lasers propagated parallel to the surface and were superimposed at the trap center 1.82 mm above the surface.

The light scattered by Ca^+ ions during the cooling process was collected by a microscope (magnification 11.5×) and spatially resolved by an image-intensified charge-coupled-device (CCD) camera with a nominal resolution of ≈ 2 μm (the numerical aperture (NA) and working distance (WD) of the objective lens were 0.13 and 64 mm, respectively). An optical band pass filter (transmission window 340-600 nm) was placed between the microscope and the camera in order to suppress stray light reflected from the surface of the electrodes. The imaging system was set up perpendicular to the trap surface along the y axis and the focus adjusted to the central layer of the crystals in the (x,z) plane.

3.2.3 Photoionisation of N_2^+

The N_2^+ ions were produced above the surface of the chip by resonance-enhanced [2+1]-multi photon ionisation (REMPI) of N_2 via the $a'' \, ^1\Sigma_g^+$ intermediate electronic state of neutral N_2 (Fig. 3.4 (b)) [176]. N_2 gas was introduced into the vacuum chamber through a leak valve at partial pressures $< 6 \times 10^{-9}$ mbar. The frequency-tripled output of a Nd:YAG-pumped pulsed dye laser operating at a wavelength of 202 nm and a pulse energy of 80 μJ was used to carry out REMPI. The dye laser operated with a mixture of Rhodamine B and Rhodamine 101 (concentrations 0.17+0.04 $\mathrm{g\,l^{-1}}$), pumped by the second harmonic of a Nd:YAG laser at 532 nm with a power of ≈ 2 W. The loading rate of N_2^+ highly depends on the pulse energy at the trap center and was approximately 0.25 $\mathrm{s^{-1}}$ in a typical experiment.

3.2.4 Backside loading of the Ca neutral beam

When loading ions into a trap, it is important to avoid the deposition of material on the electrodes which causes the buildup of stray charges and short circuits in miniaturised traps [90, 125]. We used the central gap between the two central electrodes, i.e., electrode 1 and 2 in Fig. 3.1, for backside loading of Ca, as illustrated in Fig. 3.5, to avoid this problem. A beam of Ca atoms was produced by evaporation of metallic Ca from a resistively heated stainless steel tube at $\approx$ 200–300 °C placed underneath the central trap region. A 300-μm wide slit glued onto a (x,z) translation stage was adjusted underneath the central gap to operate as a skimmer.

The atom beam passed through the skimmer, the ceramic mount of the trap and finally the gap between the two central electrodes to reach the trap center where Ca^+ ions were produced by non-resonant photoionisation. In the first experiments focused on trapping atomic ions, neutral Ca was ionised by non-resonant multiphoton photoionisation using a focused pulsed 355 nm laser beam from the third harmonics of a Nd:YAG laser at $\approx$ 0.8 mJ per pulse at 10 Hz. In the second stage when the inclusion of N_2^+ ions was explored, Ca was photoionised by the 202 nm beam which was employed for the ionisation of nitrogen molecules (Section 3.2.3).

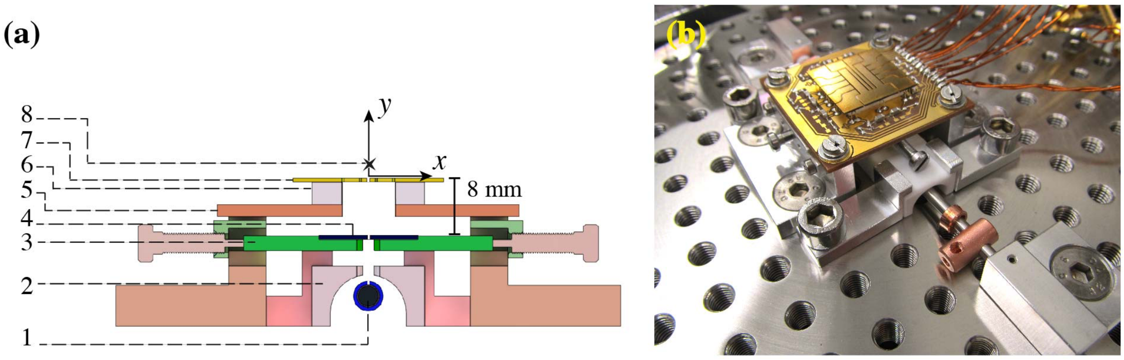

Figure 3.5: (a) A schematic of the trap and the oven assembly: 1 - The stainless steel tube containing Ca powder with a 0.5 mm wide slit on top. 2 - Ceramic heat shield. 3 - Adjustable (x,z) translation stage. 4 - 300 μm wide slit skimmer glued onto the translation stage. 5 - Filter board with a 10.5 mm wide square hole at the center. 6 - Ceramic trap mount. 7 - SE trap. 8 - Position of the trap center defining the height of trapping above the chip. (b) A photograph of the parts assembled inside the vacuum chamber.

3.2.5 The trap electronics

The RF drive for the trap was generated by a self-resonating LC circuit [185] with a resonance frequency at $\Omega_{\mathrm{RF}}=2\pi\times 8.0$ MHz and 400 to 600 V amplitude. The RF generator was adjustable for producing an output of 0-650 V and 3-15 MHz, powered by a DC power supply (*Fug, MCP 650*).

The static voltages applied to the trap electrodes were generated by an amplified, *LabVIEW*-controlled DAC card. The RC filters were used to suppress the RF voltages on the DC electrodes and to protect the amplification circuit from the RF voltage. As schematically shown in Fig. 3.6, 1 nF capacitors were placed inside the vacuum while the accompanying resistors were integrated in the amplifying circuit outside the chamber. The RF coaxial cable passed through the amplifier box (Fig. 3.7) and was introduced via the same electrical feedthrough into the vacuum chamber. Gaining and filtering the output of the DAC card in this way caused a large response time of 62 ms to ramp from 0 to 100 V (inferred from the simulation of the circuit). A *LabVIEW* program allowed addressing either each electrode individually or a set of electrodes served for a defined functionality, e.g., compensation of the stray field in the x direction.

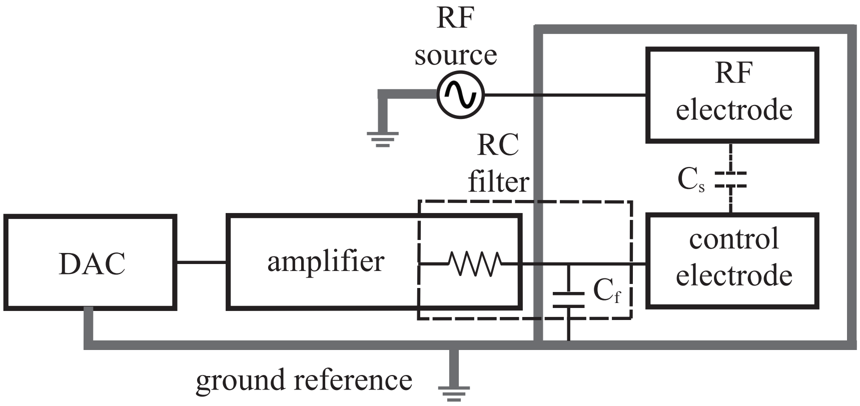

Figure 3.6: Figure showing the feeding, grounding, and filtering of a typical DC electrode in the present setup. The RF voltage coupled via a stray capacitor C_s to the control electrodes is filtered using low-pass RC filter while the resistors were placed outside of the vacuum chamber as a part of the amplifier circuit.

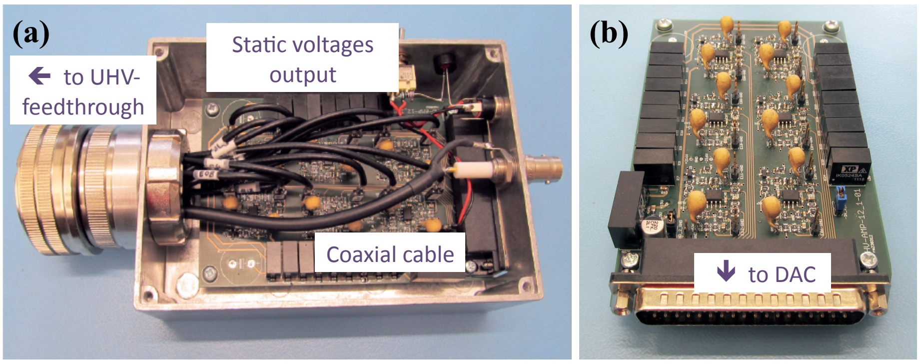

Figure 3.7: Photos of the amplifier circuit and its housing used to generate the static voltages in the experiment. The RF passes through the box via a coaxial cable. The sub-D connection was used for 12 channels from the DAC output.

3.2.6 Ultra-high vacuum

For the present experiment, ultra-high vacuum (UHV) (pressures $< 10^{-9}$ mbar) is required [54]. The main chamber was provided by *Kimball Physics* and features a 10-inch-diameter spherical octagon with eight CF40 ports (*MCF1000-SphOct-H2C8*). Once sealed, gas was removed from the chamber by a turbo-molecular pump (*Oerlikon, MAG W600*) at $600\,\mathrm{l\,s^{-1}}$ which is backed by a rotary pump (Oerlikon, TRIVAC D16B) at a pressure of $5{\times}10^{-4}$ mbar. Analysed by a residual gas analyser (Stanford Research Systems, RGA200), the remaining gas in the chamber was typically H_2O (because of its propensity to stick to the walls of the chamber) and H_2 (due to the outgassing of from the stainless steel chamber walls). To eliminate the H_2O, the entire chamber was heated to 200 °C, resulting in internal temperature of around 110 °C for about three days. To remove the H_2, a titanium sublimation pump (*Varian Tisub*) was employed which periodically releases titanium vapour. Titanium collected on the wall of the chamber acts as a getter pump, i.e., reacts with H_2 stuck on the walls and form a stable, solid product. This procedure results in the ejection of H_2 from the vacuum system. As a result, a vacuum of $< 5{\times}10^{-10}$ mbar was achieved.

3.2.7 Experimental set-up

Figure 3.8 is a photo of the experimental setup, showing the configuration of the laser beams and the hardware employed. The turbo-molecular pump was attached to a cross piece underneath the chamber.

A three-dimensional schematic of the experimental setup showing the trap, the oven assembly, imaging system, and laser beams with respect to the trap geometry is presented in Fig. 3.9. This laser configuration was used for producing spheroidal Coulomb crystals; however, for efficient Doppler cooling of planar crystals, a second 397 nm beam was additionally used co-propagating with the 866 nm beam using a dichroic mirror.

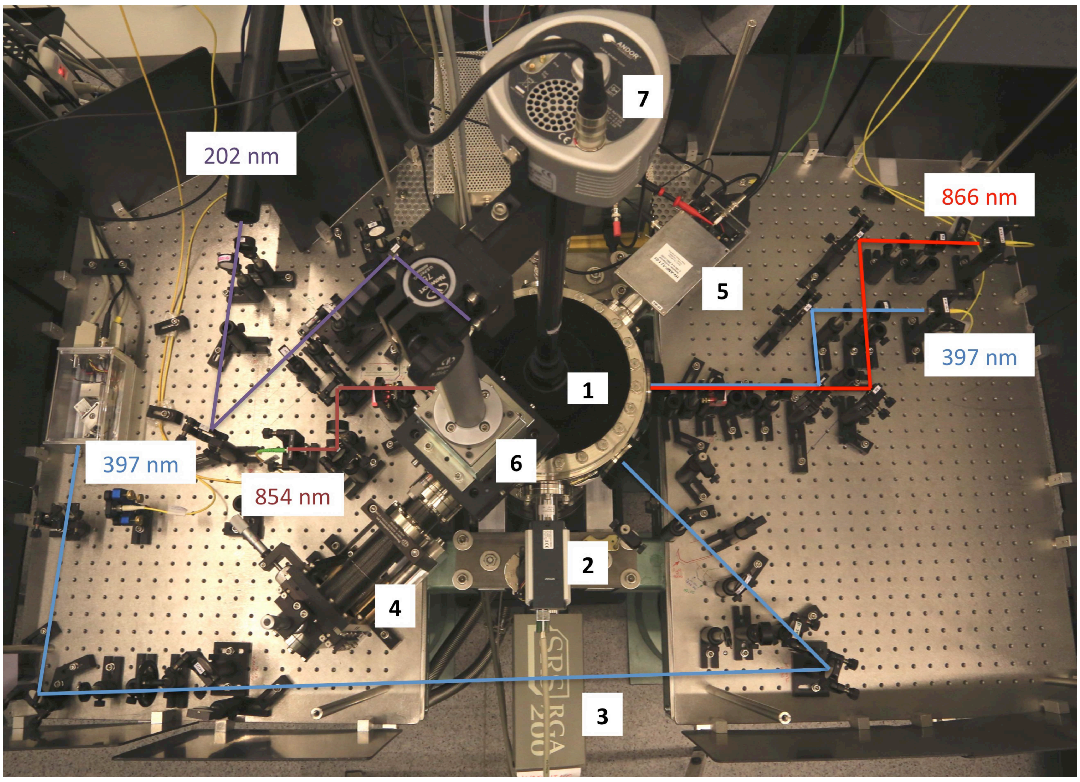

Figure 3.8: An augmented, labelled photo of the experimental setup. 1 - Vacuum chamber. 2 - Full-range pressure gauge. 3 - Residual gas analyser (RGA). 4 - Three-dimensional manipulator used to align lasers and to indicate the trap center by positioning a fiber as in Fig. 3.11. 5 - Amplifier box containing the out-vacuum trap electronics. 6 - Three-dimensional translation stage for the imaging system. 7 - Charged-coupled device (CCD) camera. The laser beams are described in Fig. 3.4.

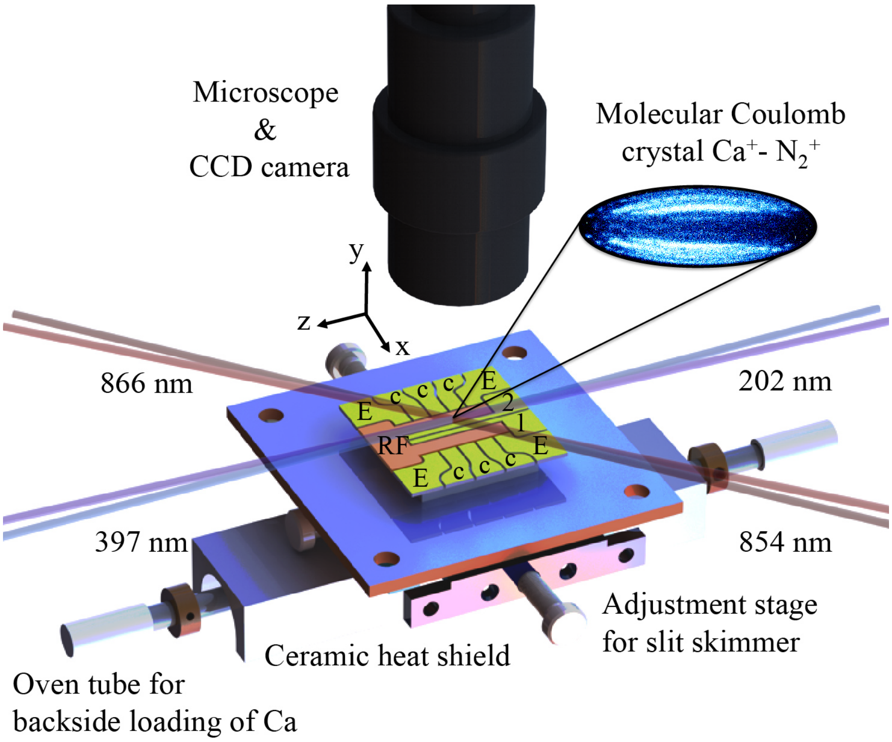

Figure 3.9: A three-dimensional schematic of the experimental setup and layout of the surface-electrode ion trap. The 397, 866 and 854 nm laser beams are for Doppler cooling of Ca$^+$. The 202 nm beam were used for the non-resonant ionisation of Ca as well as for [2+1] REMPI of N_2 molecules. The beams passing parallel to the chip surface were superimposed in the trap center 1.82 mm above the surface. The inset shows a false-colour fluorescence image of a Ca$^+$-N$_2^+$ bicomponent Coulomb crystal.

3.2.8 Measuring secular frequencies and trapping height

A sinusoidal time-varying electric potential was applied to excite the motional modes of ions leading to a drop of the ion fluorescence level at the resonant frequency, and hence providing a route for the determination of the trapping frequencies. This measurement was used to interrogate the validity of the modelled trapping potential (Section 3.1.2).

A *MATLAB* program was employed to interface the fluorescence image captured by the CCD camera and a function generator, such that the integrated fluorescence in a user-defined region-of-interest was recorded as function of drive voltage frequency. A drive voltage of 100–400 mV amplitude was applied to the control electrode 6 (Fig. 3.1) to excite the motional modes in the axial as well as transverse directions.

The results are shown in Fig. 3.10 as compared with the FEM calculations as well as the analytical calculations (Section 3.1.2). The axial frequency ω_z measured for several static configurations deviates by 5–6% from the values obtained from both models. The secular frequency ω_x deviates from FEM calculations by 11% which was attributed to the imperfect fabrication of the trap geometry, e.g., the central gap between electrode 1 and 2 (Fig. 3.1) was 322 μm according to the SEM image of the trap, as opposed to the 300-μm gap used in the FEM simulations.

The secular frequency measured for the vertical mode ω_y were in good agreement with the FEM calculations within 1.5 % relative error; however, there was a discrepancy of 11 % between experimental values and the analytical calculations as exhibited in Fig. 3.10. The reason for this is the underlying assumption in the gapless plane approximation that assumes the electrodes lie on an infinitely large grounded plane, which weaken the confinement along the vertical y axis. In addition, this effect resulted from zero boundary conditions specified infinitely far from the electrode surface in the vertical direction in the analytical model, whereas the FEM approach more closely describes the boundary conditions of the electrostatic configuration of the real trap (Section 2.6.1). These boundary conditions describe the grounded vacuum chamber as well as the board underneath the trap mount as used in the experiment. Consequently, the potentials

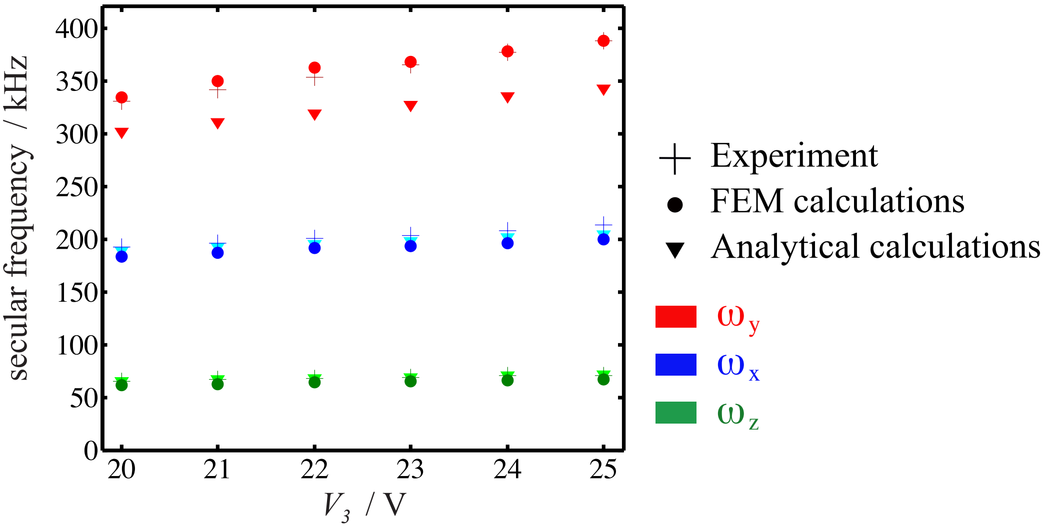

Figure 3.10: Comparison between the experimental and calculated values of the trapping frequencies for Ca^+ as a function of the endcap voltage V_3. See Figure 3.9 for the definition of the coordinate axes.

calculated analytically in those configurations exhibit less stiff confinement in the vertical direction y in comparison to those obtained from FEM calculations in which the trap was mounted above a given grounded plane.

To indicate the trapping height, a tip of a transparent fiber of 160 μm diameter elevated above the trap surface was illuminated by the laser beams. The fiber tip could be positioned with a precision of ±10 μm using the manipulator shown in Fig. 3.8. The trapping height drastically varies as a function of static voltages (Section 2.2.1). Figure 3.11 (a) and (b) exhibit the experimental results and calculated values as a function of the endcap-electrode voltage V_3 and the central-electrode voltage V_1. By subtracting 300 μm from the experimental values, they were found to agree with FEM calculations within the error bars. This implies a large systematic error arising from the initial positioning of the fiber above the surface. Therefore, this method was found to be unsuited for the determination of the trapping height in such experiments.

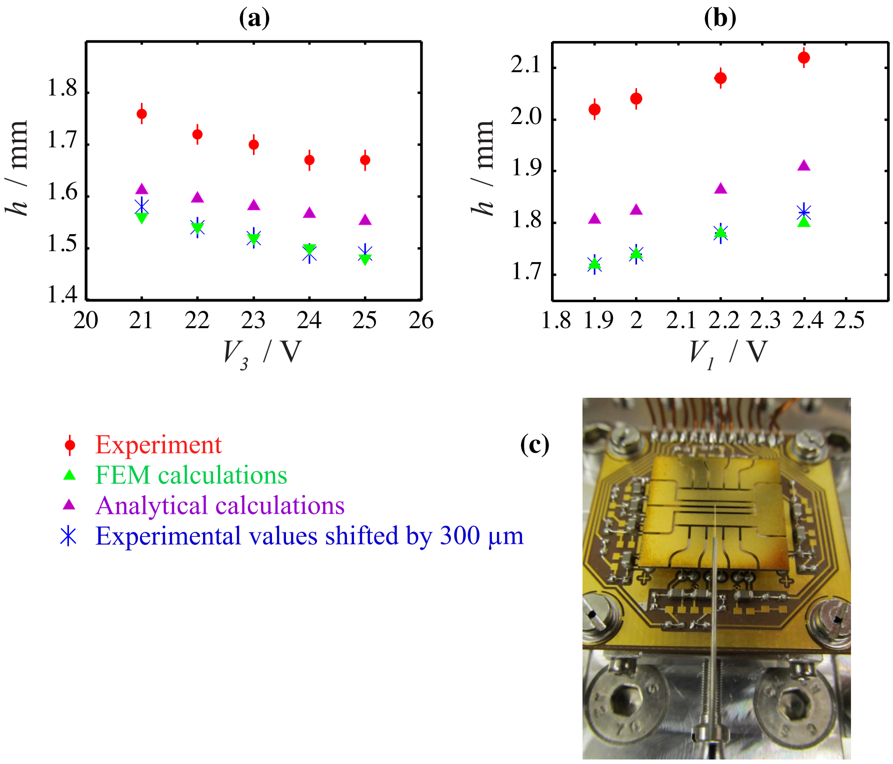

Figure 3.11: Variation of the trapping height h as a function of static voltages applied to (a) the endcap electrodes (V_3) and (b) the two central electrodes (V_1) (see Figure 3.1). The triangular markers used for calculations are larger than their error bars. (c) A picture showing the fiber elevated above the surface of the electrodes. The tip of the fiber was used to indicate the position of the trap center above the surface as superposed by the laser beams (Section 3.2.2 and 3.2.3).

Chapter 4

Experimental results and discussions

This chapter presents the experimental demonstration of sympathetic cooling of molecular ions in the six-wire SE trap developed, as well as a detailed discussion about the structural and energetic properties of Coulomb crystals obtained in this device [104, 105]. The configuration of trapping potentials generated by the surface electrodes enabled the formation of planar bicomponent Coulomb crystals and the spatial separation of the molecular from the atomic ions on the chip. Furthermore, the effects of trap anharmonicites on the properties of bicomponent crystals explored theoretically are presented, providing an insight to the similarities and differences for the crystals obtained in linear Paul traps and SE traps with different sizes. The structural and thermal properties of the Coulomb crystals were characterized using molecular dynamics (MD) simulations. As already discussed in Section 2.6.2, MD simulations presented in this work give an upper limit of the secular kinetic energies of ions due to the implementation of the heating forces as small force kicks in the calculations [177].

4.1 Sympathetically cooled molecular ions on the chip

For the present experiments with laser-cooled $^{40}\mathrm{Ca}^+$, N_2^+ (mass 28 amu) and CaH^+ (mass 41 amu) were chosen[1] as prototypical molecular ions with lighter and heavier masses, respectively. The method of the production of N_2^+ ions is discussed in Section 3.2.3. CaH^+ ions were produced by chemical reactions of trapped laser-excited Ca^+ ions with H_2 molecules leaked into the vacuum chamber. Figure 4.1 shows (a) experimental and (b, c) simulated images of typical Coulomb crystals imaged in the xz plane parallel to the surface of the chip. The molecular ions do not fluoresce and are only indirectly visible as dark areas appearing in the fluorescence images of the crystals (Section 1.2.1). In Fig. 4.1 (c), the sympathetically cooled molecular ions have been made visible in the simulated images for clarity. Column (i) in Fig. 4.1 shows a pure atomic Coulomb crystal containing 262 Ca^+ ions at a mean secular energy E_{sec}/k_B=23 mK, where the secular energy is defined as the thermal energy of ions without the micromotion (Section 2.1.1).

Although the shapes of the crystals projected onto the imaging plane (Fig. 4.1) are reminiscent of those obtained in conventional linear RF traps [54], these crystals are not spheroidal due to the lack of the degeneracy of the trap frequencies in the transverse (x, y) directions. For the present case, the principal trap frequencies were determined to be $\omega_x/2\pi = 171$ kHz, $\omega_y/2\pi = 272$ kHz and $\omega_z/2\pi = 83$ kHz. Note that this resulted from the particular choice of the static potential configuration (Section 3.1.3), and in SE traps spheroidal crystals can also be achieved (see Section 4.4.2 and 4.4.3 as well as Ref. [121])

The $\mathrm{Ca}^+{-}\mathrm{N}_2^+$ bicomponent Coulomb crystal shown in Fig. 4.1 (ii) (a) was obtained by loading N_2^+ into a Ca^+ Coulomb crystal. Based on MD simulations, we inferred that this crystal contains 50 N_2^+ ions sympathetically cooled to E_{sec}/k_B=43 mK in equilibrium with 180 Ca^+ at E_{sec}/k_B=33 mK. Due to the

---

[1] Nitrogen molecular cation is an interesting choice because it is one of the most extensively studied molecules in spectroscopy [101]. Metal hydride ions are useful for applications in quantum logic spectroscopy [102], frequency standards and black-body radiation (BBR) thermometry [103].

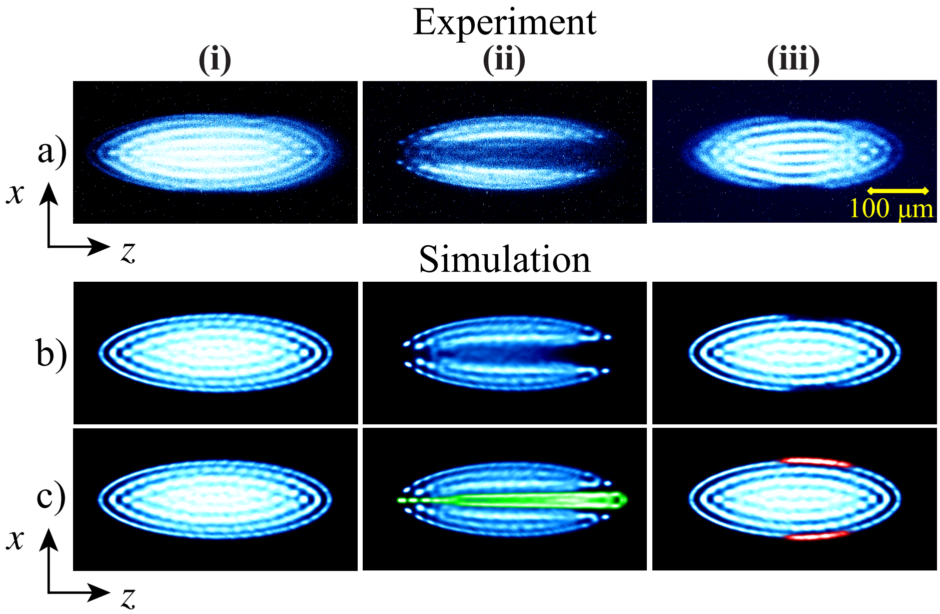

Figure 4.1: (a) Experimental and (b,c) simulated false-colour laser-cooling fluorescence images of bicomponent Coulomb crystals in the chip trap. In (c), the sympathetically cooled molecular ions were made visible in the simulations for clarity. Colour code: Ca^+: blue, N_2^+: green and CaH^+: red. (i) Pure atomic crystal containing 262 Ca^+ ions, (ii) 50 sympathetically cooled N_2^+ and 180 Ca^+ ions, and (iii) 7 sympathetically cooled CaH^+ and 200 Ca^+ ions.

tighter confining force for lighter ions (Section 3.1.3), N_2^+ ions localised closer to the central trap axis than the Ca^+ ions. The asymmetric shape of the N_2^+ crystal along the z-direction was caused by the unidirectional radiation pressure force acting on Ca^+ ions, as well as small asymmetries in the potential induced by the geometry of the RF electrodes (Fig. 3.1 and 3.9).

Column (iii) of Fig. 4.1 shows 7 CaH^+ ions at E_{sec}/k_B=28 mK sympathetically cooled by 200 Ca^+ ions at E_{sec}/k_B=24 mK. Heavy CaH^+ ions localise at the edges of the Ca^+ crystal. Sympathetically cooling of a larger number of CaH^+ ions was found to be difficult which was attributed to the reduced contact volume of CaH^+ with the laser-cooled Ca^+ ions at the extremities of the crystal, as well as the reduced trap depth for heavier species.

The flexibility in shaping the trapping potentials using the chip lends itself to a precise manipulation of the crystals to form structures which are challenging

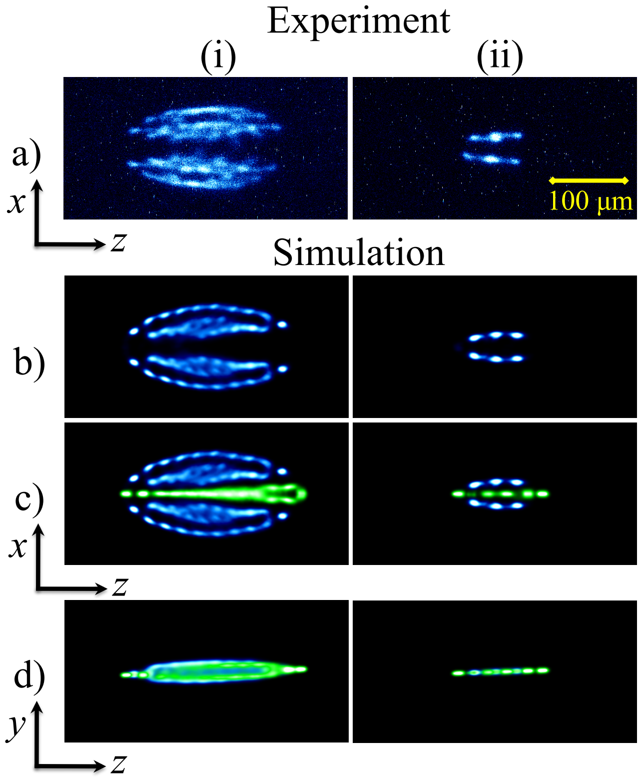

Figure 4.2: Ca^+−N_2^+ bicomponent Coulomb crystals in the chip trap at different trapping configurations. (a) Experimental and (b,c,d) simulated false-colour laser-cooling fluorescence images. N_2^+ ions were made visible in green in the simulations for clarity. In panel (d), a side view of simulated images in the yz plane perpendicular to the chip are shown. (i) 18 N_2^+ ions bisecting a near-planar Coulomb crystal with 50 Ca^+ ions. (ii) A string of 5 N_2^+ sympathetically cooled by two strings with 3 Ca^+ ions each.

to obtain in conventional electrode geometries. In the experiment shown in column (i) of Fig. 4.2, a near-planar bicomponent Coulomb crystal was formed with sympathetically cooled N_2^+ ions centred along the RF null line splitting the Ca^+ crystal in two halves. From the simulated side view of the crystal shown in Fig. 4.2 (i) (d), it can be seen that the crystal has a pancake-like shape and is at maximum only two layers of ions thick. In the experiment shown in column (ii) of Fig. 4.2, a completely planar structure was generated consisting of a string of 5 N_2^+ ions sympathetically cooled by two adjacent strings of 3 laser-cooled Ca^+ ions each. Such planar bicomponent structures have been proposed as a framework for quantum computation and simulation [186].

In the following, we focus on three important aspects: (1) the shape and energetics of the bicomponent crystals as a function of the crystal composition, (2) details of the experiments to spatially separate different ionic species in a crystal, and (3) the effect of trap anharmonicities on the structure of bicomponent crystals.

4.2 Structure and energetics of bicomponent crystals as a function of their composition

The number of sympathetically cooled N_2^+ ions in the crystals was controlled by varying the ionisation rate of neutral N_2 following the preparation of a pure Ca^+ crystal (Section 3.2.3). A set of experiments performed by loading varying numbers of N_2^+ ions into the trap is shown in Fig. 4.3. The molecular ions appear as a dark area in the centre of the crystals and have been made visible in green in the simulations for clarity. Slight discrepancies between the experimental and simulated images are attributed to machining imperfections of the trap electrodes which were not accounted for in the simulations. The crystals in the experiments shown in Fig. 4.3 (ii)-(vi) were composed of 3 % up to 28 % of N_2^+ ions as deduced from comparisons with simulated images. The uncertainty in the determination of the ion numbers amounted to ±1 for N_2^+ ions and ±2 (±5) for Ca^+ ions in small (big) crystals. Uncertainties arise from the fact that usually a range of simulated images with slightly varying ion numbers closely

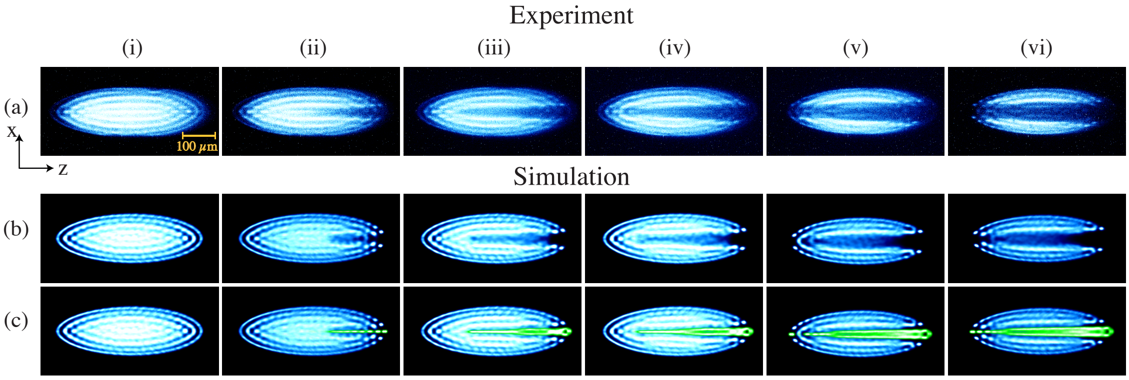

Figure 4.3: (a) Experimental and (b,c) simulated false-color laser-cooling fluorescence images of $Ca^+ - N_2^+$ bicomponent Coulomb crystals in the SE trap. In (c), the sympathetically cooled molecular ions were made visible in the simulations for clarity. Colour code: Ca^+: blue, N_2^+: green. (i)-(vi) The Coulomb crystals shown in (i) - (vi) contained 0, 8, 22, 28, 42 and 50 N_2^+ ions corresponding to percentages of 0, 3, 9, 12, 22, 28 % of the total number of ions.

match the experimental image [173, 180]. The asymmetric structure of the N_2^+ crystals along the z-axis resulted from the radiation pressure force acting on the Ca^+ ions caused by unidirectional laser cooling, as well as asymmetries in the RF force caused by the asymmetric geometry of the finite-sized RF electrodes (Fig. 3.1 and 3.9). During the loading phase, a small number of Ca^+ ions was lost because of collisions with neutral N_2 molecules.

The average secular energies (i.e., the ion energies without micromotion) of the ions in the crystals of Fig. 4.3 (i)-(vi) are shown in Fig. 4.4 which depend on the number of laser-cooled ions in relation to the number of sympathetically cooled ions. Increasing the number of N_2^+ ions resulted in higher average secular energies for both species. For instance, the crystal shown in Fig. 4.3 (ii) contains 8 sympathetically cooled N_2^+ ions at E_{sec}/k_B=30 mK in conjunction with 257 Ca^+ ions at E_{sec}/k_B=24 mK. For the crystal in Fig. 4.3 (vi), the average secular energy amounts to E_{sec}/k_B=43 mK for 50 sympathetically cooled N_2^+ ions with 180 Ca^+ ions at E_{sec}/k_B=33 mK. Across the series of crystals studied, the difference in average energy between the two species increased from 6 mK to 10 mK with increasing the ratio between N_2^+ and Ca^+.

The trends observed in Fig. 4.3 can be explained by an increasingly unfa-

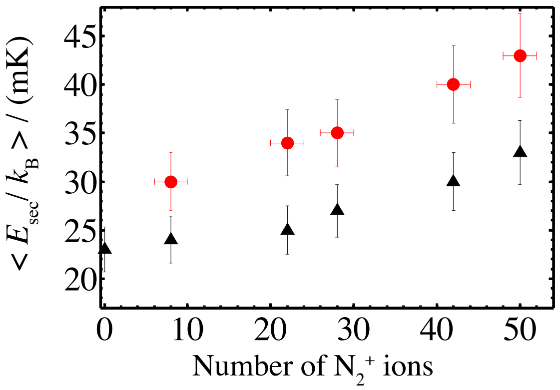

Figure 4.4: Average secular energies of laser-cooled atomic (Ca^+: black triangle) and sympathetically cooled molecular (N_2^+: red circle) ions plotted as a function of the number of sympathetically cooled N_2^+ ions in the crystals shown in Fig. 4.3 (see text for details).

vourable ratio of heating to cooling forces acting on the entire ion ensemble. As molecular ions are only indirectly cooled by Ca^+ ions, but are subject to the same heating processes (apart from photon recoil, i.e., RF heating and collisions with background gas), the average secular energy of the N_2^+ ions is higher relative to that of Ca^+ ions. The secular energies of both species depend on the absolute and relative numbers of different ions in the crystal. These results are in agreement with previous findings on bicomponent crystals in linear Paul traps [72]. Note that these results depend also on the spatial distribution of the ion subensemble with respect to the RF null line.

4.3 Spatial separation of ion species

If a trapped ion is subjected to a uniform static electric field $\mathbf{E}_{\rm DC}$ along the y axis, the average position of a single ion is displaced by $y_{\rm ion} \cong Q\mathbf{E}_{\rm DC} \cdot \hat{y}/m\omega_i^2$ [108], where ω_i is the secular frequency and $\hat{y}$ the unit vector along y. Ions with different masses exhibit different displacements due to the mass dependence of the pseudopotential although subjected to the same static field. In large bicomponent Coulomb crystals, such displacements can result in a complete

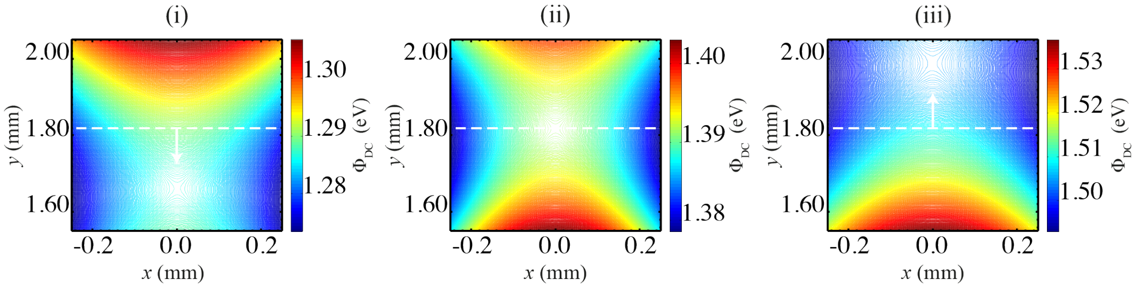

Figure 4.5: Static potential configurations $\Phi_{\rm DC}$ in the xy plane used for the spatial separation of the N_2^+ and Ca^+ ions. The dashed line indicates the position of the RF null line. In (i) and (iii), the minimum of the static potential was displaced below and above the RF null line, respectively. In (ii), the minimum of $\Phi_{\rm DC}$ coincides with the RF null line, corresponding to an axialized trapping configuration.

separation of species if the difference between the displacements for each species exceeds the spatial extension of the crystals. Note that in the present context, spatial separation refers to increasing the mean distance of the centres of atomic and molecular ion crystals, as opposed to the segregation of ionic species within perfectly axialized crystals [54, 57].

The static potential configurations used for demonstrating the spatial separation of ions are illustrated in Fig. 4.5. By applying additional voltage offsets of -0.3, 0.0 and 0.35 V on the two central electrodes, the height of the trap minima for both species was changed. The static fields generated along the y-axis were calculated to be 46 $\mathrm{V\,m^{-1}}(-\hat{y})$, 0 $\mathrm{V\,m^{-1}}$, 50 $\mathrm{V\,m^{-1}}(+\hat{y})$ at the centre of the trap across the three configurations shown in Fig. 4.5 (i)-(iii). Fig. 4.6 (i)-(iii) show the same Coulomb crystal under these three trapping conditions. In Fig. 4.6 (i) and (iii), a near-planar bicomponent crystal is shown in which the N_2^+ ions were spatially separated from the Ca^+ ions in the positive and negative y directions, respectively. In Fig. 4.6 (ii) the same crystal was centred on the RF null line.

Figure 4.7 (a) shows the extent of the spatial separation of the species in the experiments of Fig. 4.7 as extracted from the MD simulations. In the crystal shown in Fig. 4.6 (i), the average displacements from the RF null line $\langle y_{\rm ion} \rangle$ were obtained to be 50 μm for N_2^+ and 31 μm for Ca^+ leading to a separation of 19±2 μm. By pushing the ions above the RF null line as shown in Fig. 4.6(iii),

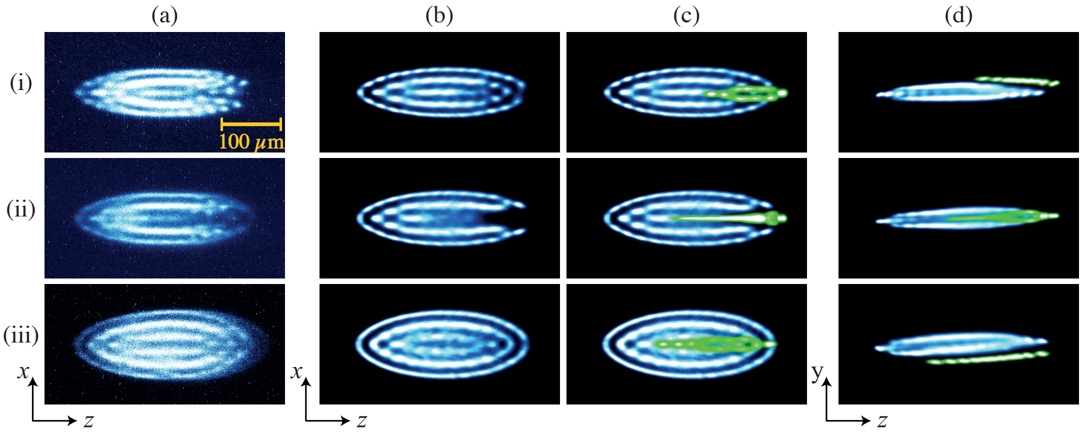

Figure 4.6: Demonstration of the spatial separation of $\mathrm{Ca^+}$–$\mathrm{N_2^+}$ Coulomb crystals into an atomic and molecular component. (a) Experimental and (b,c,d) simulated false-colour fluorescence images. In (c,d), the sympathetically cooled molecular ions were made visible in green in the simulations for clarity. In (d), side views of the simulated crystals are displayed showing the separation of the ion species. (i) The $\mathrm{N_2^+}$ crystal was placed above the $\mathrm{Ca^+}$ crystal while both were subjected to an electric field along the $-y$ direction and pushed underneath the RF null line. (ii) The crystal was axialized and the $\mathrm{N_2^+}$ and $\mathrm{Ca^+}$ crystals were centred on the RF null line. (iii) The $\mathrm{N_2^+}$ crystal was placed underneath the $\mathrm{Ca^+}$ crystal while both were subjected to an electric field along the $+y$ direction and pushed above the RF null line.

the layers of $\mathrm{N_2^+}$ and $\mathrm{Ca^+}$ ions were moved by 40 μm and 62 μm, respectively, resulting in an average separation of 22±2 μm.

As demonstrated in Fig. 4.7 (b), the spatial separation of sympathetically cooled $\mathrm{N_2^+}$ ions from laser-cooled $\mathrm{Ca^+}$ ions adversely affected the cooling efficiency because of the reduced contact volume between the two species. Moreover, the application of the uniform static field that changed the trapping height also altered the secular trapping frequencies. This can be seen from the variation of the aspect ratios of the crystals in Figs. 4.6 (a) (i)-(iii). The secular frequencies for $\mathrm{Ca^+}$ were calculated to be $(\omega_x, \omega_y, \omega_z)$=(186, 290, 83) kHz, (172, 273, 83) kHz and (156, 257, 84) kHz for the crystals shown in Fig. 4.6 (i), (ii) and (iii), respectively. Consequently, the secular kinetic energies of $\mathrm{Ca^+}$ ions $E_{\mathrm{Kin(i)}} \propto m u_{(i)} \omega_i^2$ (where $u_{(i)}$ is the amplitude of the ion's secular motion [108])

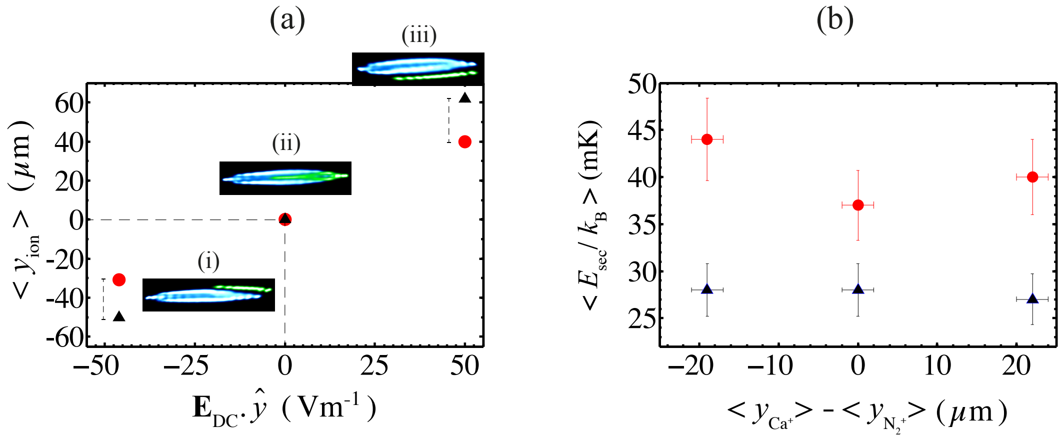

Figure 4.7: (a) Shifts of the average ion positions $\langle y_{\text{ion}}\rangle$ for Ca$^+$ and N$_2^+$ caused by an applied static field (Ca$^+$: black triangle, N$_2^+$: red circle) for the three crystals shown in Fig. 4.6. The error bars in the distances are smaller than the size of the symbols. (b) Average secular energies of both species as a function of distance between the atomic and molecular ions. The error bars reflect the uncertainty in the comparison of the simulated with the experimental images.

were also modified (Figure 4.7 (b)). For N$_2^+$ ions, the average secular kinetic energy calculated for the crystal above the RF null line is less than that for the crystal beneath the RF null line (labelled with (iii) and (i) respectively in Fig. 4.7) due to the contribution of both factors.

The static electric fields used to separate the ionic species caused significant excess micromotion. Ca$^+$ ions were subjected to wider micromotion amplitudes because of their farther displacements from the RF null line. We inferred that the average total energies of the ions have been increased by $\langle \Delta E_{\text{total}}\rangle/k_B$=3.5 K for N$_2^+$ and $\langle \Delta E_{\text{total}}\rangle/k_B$=7 K for Ca$^+$ ions in the case for the crystal pushed underneath the RF null line in Fig. 4.6 (i). For the crystals pushed above the RF null line in Fig. 4.6 (iii), $\langle \Delta E_{\text{total}}\rangle/k_B$=4.5 K and 13.5 K have been calculated for N$_2^+$ and Ca$^+$ ions, respectively. The higher energies compared to the conditions in Fig. 4.6 (i) were caused by the farther displacement of the ions from the RF null line in this case.

4.4 Anharmonicity effects on bicomponent Coulomb crystals

In the present context, the investigation of anharmonicity effects is of importance because of the following reasons:

(1) The miniaturization of the trap geometry potentially leads to the increase of anharmonic terms in the trapping potential [115].

(2) The asymmetry of the geometry in SE traps can cause significant odd-order terms in the direction perpendicular to the surface of electrodes. As discussed in Section 2.2.3, these higher-order components would cause adverse effects, for instance, the frequency shift of ions' motional modes that harm applications such as frequency standards. This results in an additional challenge in designing microfabricated SE traps. Due to the flexibility of planar electrode geometries, the trapping potentials in such traps can be engineered in order to suppress those terms.

(3) In experiments with a large number of trapped ions, anharmonicity effects could become particularly significant because different ions may experience different curvatures of the trapping potential at their equilibrium positions.

(4) In sympathetic-cooling experiments (e.g., mixed-species ion crystals), the equilibrium position of ions depends on the relative masses [115]. Therefore, ions of different mass-to-charge ratios experience different anharmonicities not only because of the mass dependence of the pseudopotential but also due to their differing equilibrium positions.

(5) Anharmonicities can be introduced deliberately using tailored control fields to engineer ion crystals with special properties [134, 135] or to selectively address transitions and coherently control the motional mode of ions [136, 137].

The effects of anharmonicity can be quantified in the framework of a power series expansion of the total trapping potential [115]:

$$\Phi_{\mathrm{t}}(x_i) = \sum_{n=2}^{\infty} \kappa_n x_i^n = \kappa_2 x_i^2 \left[1 + \sum_{n=3}^{\infty} \left(\frac{x_i}{\lambda_n} \right)^{n-2} \right], \tag{4.1}$$

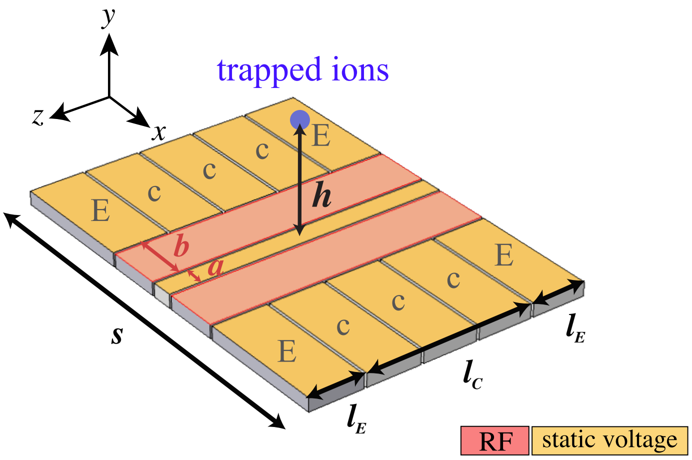

Figure 4.8: A schematic of a five-wire SE trap used to model the trapping potentials for the five study cases. a and b are the width of the central DC and RF electrodes, and h is the trapping height. The width and distance of the endcap electrodes (labelled with E) along the trap axis are indicated by l_E and l_C. The DC (RF) electrodes are not semi-infinite (infinite) along the x (z) direction, i.e., the overall size of the traps was restricted to $s = 50{\times}h$.

where

$$\lambda_n = (\kappa_n/\kappa_2)^{1/(2-n)}. \tag{4.2}$$

Here, $\mathit{\Phi}_{\mathrm{t}}$ refers to a one-dimensional cut through the total potential, κ_n are expansion coefficients and λ_n parameterises the length scale over which anharmonic terms of order n become comparable to the harmonic contribution. The larger λ_n, the less significant the corresponding anharmonic potential term and the longer the length scale over which anharmonicity manifests itself in the properties of ion crystals. Since anharmonic terms tend to be more pronounced in miniaturised traps which exhibit small values of λ_n, the question arises at which size of trap anharmonicities start to appreciably affect the properties of bicomponent crystals. This question is addressed using a theoretical study which enables the quantitative rationalization of the effects observed.

4.4.1 Design of the study cases

We employed SE traps of different sizes which feature systematically varying anharmonic potential terms and implemented MD simulations to study the properties of bicomponent Coulomb crystals in those traps. A five-wire SE trap, as schematically depicted in Fig. 4.8, was adopted and modelled in the gapless plane approximation using the SurfacePattern software [179]. The trapping height h was chosen as the characteristic length scale of the systems. The geometries were refined using the analytical model in Ref. [114], and were specified by (a, b, h) = (1975, 2332, 1800), (979, 1166, 900), (544, 648, 500), (217, 259, 200) and (109, 129, 100) μm. The overall size of the chip was chosen to be in a square of $50 \times h$. The consistent scaling of the entire geometry in this way enabled comparison between the results obtained.

The applied RF and static voltages must be chosen such that the harmonic trap frequencies were kept the same in all cases in order to render the harmonic part of the trap potentials comparable. In addition, radial frequencies in the xy plane need to be degenerate to enable a comparison with linear Paul traps [54].

Figure 4.9 (a) depicts the variation of the intrinsic depth D_{int} and the stability parameter Q_{xx} $(= -Q_{yy})$ for the SE trap with $h = 200\mu$m as a function of the RF voltage amplitude V_{RF} and frequency Ω_{RF}. As the ion-electrode distance varies over one order of magnitude in these five geometries, it is challenging to chose values of the V_{RF} and Ω_{RF} which lead to sufficiently small stability parameters and simultaneously a deep potential well. This is illustrated in Fig. 4.9 (c) in the V_{RF}-Ω_{RF} space in which there is no overlap between desired trapping configurations for SE traps of different scales (labelled with their characteristic height). Thus the RF frequency was fixed at Ω_{RF}=$2\pi \times 8.17$ MHz and Q_{xx}=$(-Q_{yy})$ = 0.3 while the trap depth was varied. Figure 4.9 (d) shows that this choice necessitates high (low) V_{RF} values for big (small) traps.

To determine the static voltages (i.e., V_i to apply to the ith DC electrodes; endcap, central, and control electrodes shown in Fig. 4.8), the Lagrange multi-

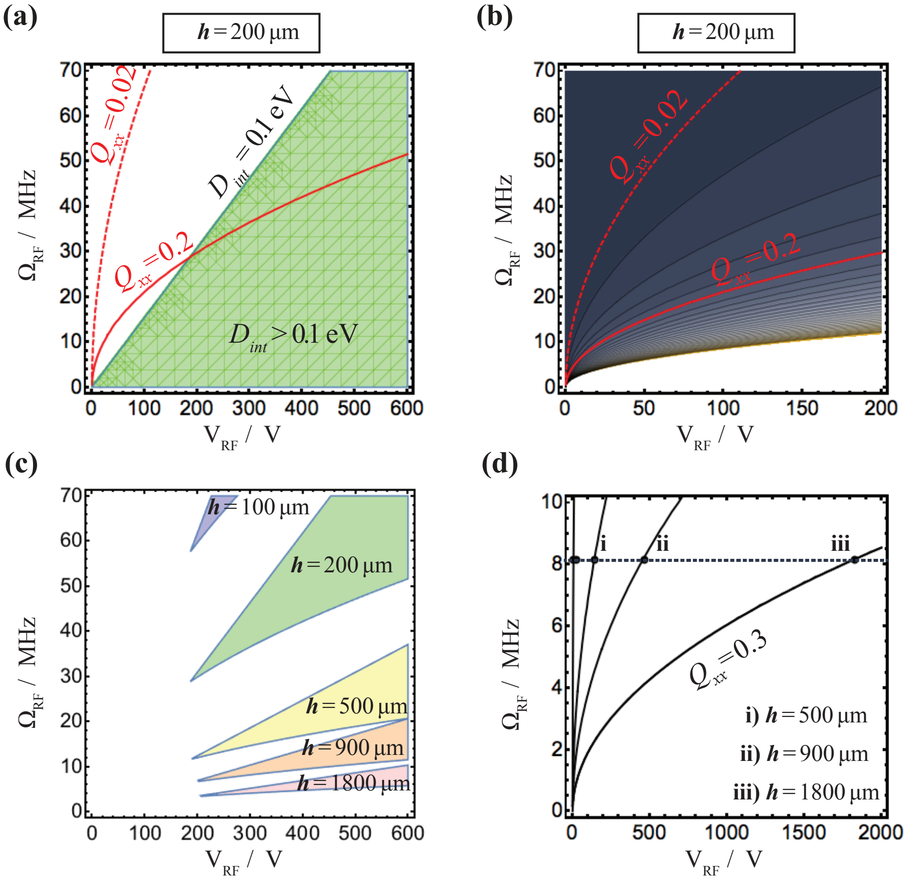

Figure 4.9: Illustration of the relation between the intrinsic depth D_{int} and the stability parameter Q_{xx} for the SE traps designed as a function of the RF voltage amplitude $V_{\rm RF}$ and frequency $\Omega_{\rm RF}$. In (a), the region in which $D_{int} > 0.1$ eV is in green, and $Q_{xx} = 0.2$ and $Q_{xx} = 0.02$ are shown with solid and dashed lines, respectively, also illustrated in (b) separately for clarity. In (c), the intersection area representing $D_{int} \geq 0.1$ eV and $Q_{xx} \leq 0.2$ for the five SE traps is displayed (labelled with their trapping height h). As the trap size scales over one order of magnitude optimal operational RF voltages do not overlap in the $V_{\rm RF}$-$\Omega_{\rm RF}$ space. (d) shows the chosen values of $V_{\rm RF}$ while $\Omega_{\rm RF}$ is fixed at 8.17 MHz.

plier method was used which is formulated as:

$$\begin{cases} \text{maximise:} \quad f = \sum_i V_i^2, \\ \text{subject to:} \quad \begin{cases} g_1 &= \sum_i V_i \nabla \phi_{i,\mathrm{dc}} = 0, \\ g_2 &= \sum_i \frac{\partial^2 \phi_{i,\mathrm{dc}}}{\partial z^2} - \alpha = 0, \\ g_3 &= \sum_i \frac{\partial^2 \phi_{i,\mathrm{dc}}}{\partial x^2} - \sum_i \frac{\partial^2 \phi_{i,\mathrm{dc}}}{\partial y^2} = 0, \\ g_4 &= \frac{q^2 V_{\mathrm{RF}}^2}{2m\Omega_{\mathrm{RF}}^2} \left(\frac{\partial^2 \phi_{\mathrm{RF}}}{\partial y^2} \right)^2 - \frac{\alpha}{2} - \beta = 0. \end{cases} \end{cases} \tag{4.3}$$

The target function f is proportional to the power consumption. m and q are the mass and charge of the trapped ions, and V_{RF} and Ω_{RF} denote the RF amplitude and frequency, respectively. ϕ_{RF} and ϕ_{DC} denote the RF and DC-electrode-potential basis function. α and β are defined as:

$$\begin{aligned} \alpha &= m\omega_z^2, \\ \beta &= m\omega_x^2 = m\omega_y^2. \end{aligned} \tag{4.4}$$

Hence the multiple constraints given in Eqn. 4.3 represent the following requirements:

g_1- Static electric fields at the trap centre must vanish to ensure an axialized trapping configuration.

g_2- The axial trap strength is specified by α to generate a desired axial secular frequency (z is the coordinate along the trap axis (Fig. 4.8)).

g_3- The radial confinement must be degenerate in order to enable comparison between Coulomb crystals in SE and Paul traps (xy is the transverse plane (Fig. 4.8)).

g_4- The ratio of β to α, known as the anisotropy parameter [117], must be specified to determine the spatial distribution of ions with respect to the RF null line. In this way, the aspect ratio of the crystals [57] obtained in different SE as well as Paul traps is identified which allows comparison between total energies of ions (i.e., thermal energies of ions including the micromotion).

The secular trapping frequencies are given by:

$$\begin{aligned} \omega_j &= \frac{1}{\sqrt{m}} \sqrt{\frac{q^2}{2m\Omega_{\mathrm{RF}}^2} \left(\frac{\partial^2 \phi_{\mathrm{RF}}}{\partial {x_j}^2} \right)^2 + q \sum_i V_i \frac{\partial^2 \phi_{i,\mathrm{dc}}}{\partial {x_j}^2}} \\ &= \frac{\Omega_{\mathrm{RF}}}{2} \sqrt{\frac{Q_{jj}^2}{2} + A_{jj}} \quad . \end{aligned} \tag{4.5}$$

As a result, the voltages calculated by solving Eqn. 4.3 lead to an identical harmonic contribution in all cases specified by $\omega_y = \omega_x = 840$ kHz and $\omega_z = 300$ kHz. The stability parameters were $A_{zz} = -2A_{yy} = -2\ A_{xx} = 5.4 \times 10^{-3}$ (Section 2.1.2), highlighting the degeneracy of the radial modes under these trapping conditions for all SE traps.

4.4.2 Characterization of anharmonic contributions

Figure 4.10 (a) shows one-dimensional cuts through the total potential Φ_{t} along the vertical (y) axis for the different traps calculated for the trapping conditions as discussed in the previous section (solid lines). For comparison, a harmonic potential with the same harmonic trapping frequencies is also shown. A visual comparison of Φ_{t} with the harmonic potential illustrates the increasing degree of anharmonicity with decreasing the trap size (see the potentials near their minima for the smallest three traps in the inset). This is quantified in Fig. 4.10 (b) which shows λ_{3y}, the λ_3 parameter for Φ_{t} along the y-axis, obtained by a fit of Eqn. 4.2 to Φ_{t}. λ_{3y} scales linearly with the trapping height (as can also be shown from Eqn. 4.2) ranging from $\approx -34\mu$m to $\approx -614\ \mu$m for the smallest to the largest trap studied, respectively. The insets display λ_{3y} for different molecular-ion species. The mass dependence of λ_{3y} results from different strengths of the pseudopotential Φ_{ps} for the different species.

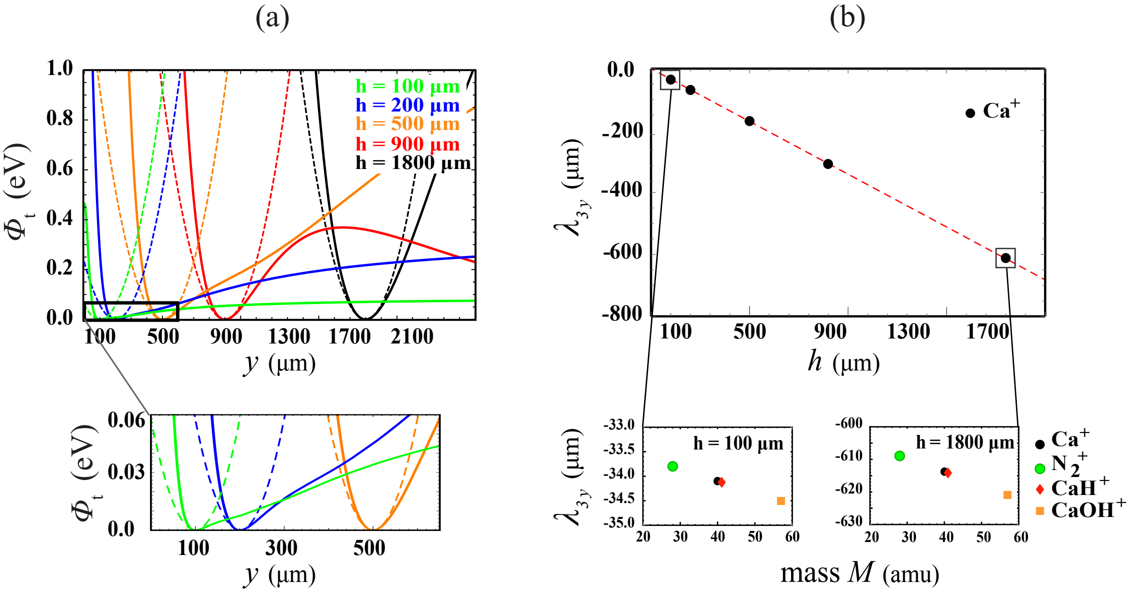

Figure 4.10: (a) One-dimensional cuts through the total trapping potential Φ_t for Ca$^+$ along the vertical (y) axis through the trap centre for SE traps with different trapping heights h and identical harmonic frequencies (solid lines). The dashed lines show a harmonic potential yielding the same secular frequencies. The inset shows a magnified view of the potentials near the trap centre of the smallest traps. (b) Anharmonicity parameter along the y axis λ_{3y} for the same traps. The insets display λ_{3y} for different ion species in the traps with $h = 100$ μm and 1800 μm.

4.4.3 Structural and energetic properties of bicomponent crystals

The MD simulation implemented has already been discussed in detail in Section 2.6.2. The trapping force was calculated from analytical gradients of the trapping potentials approximated by power series expansions using a three dimensional fit to the numerically computed RF and static potentials near the trap centre for each trap. In this treatment all possible higher-order and cross terms were considered up to the 4^{th} order terms.

In Fig. 4.11 (a)-(d), MD simulations of bicomponent crystals containing 50 Ca^+ ions and 10 sympathetically cooled ions for three different molecular species in SE traps of four different sizes (labelled by their trapping heights h) are presented. The ions form spheroidal crystals with spatial extensions of $D < 30$ μm in the xy plane. The panels display "snapshots" of ion configurations obtained near the end of the simulation period. For comparison, the analogous crystals obtained in a large linear Paul trap with the same harmonic secular frequencies (Fig. 4.11 (e)). The only weakly anharmonic, larger SE traps exhibit crystal structures resembling the ones in the linear Paul trap. In contrast, the more anharmonic, smaller traps show an asymmetric segregation of ionic species which becomes more pronounced with decreasing trap size. This asymmetric segregation is a consequence of the increasingly anharmonic trap potential in the vertical direction for smaller traps (Fig. 4.11 (a)). This effect is particularly pronounced for heavy sympathetically cooled ions like $CaOH^+$ (see bottom panel in Fig. 4.11 (a-e) with comparatively weak pseudopotentials in the vertical direction. We note that special care was taken to ensure that the minima of Φ_t and Φ_ps coincided for all crystals in order to avoid artefacts in the simulations resulting from imperfect axialization.

The quantification of the observed effect is enabled by a comparison between the smallest λ_n and D the spatial extension of the Coulomb crystals formed in a trap. The choice of identical secular frequencies in all three directions for all geometries led to similar spatial extensions of the crystals obtained. Therefore, these calculations enabled conclusive comparisons. The effect arising from the number of trapped ions which specifies the size of the crystal also must be

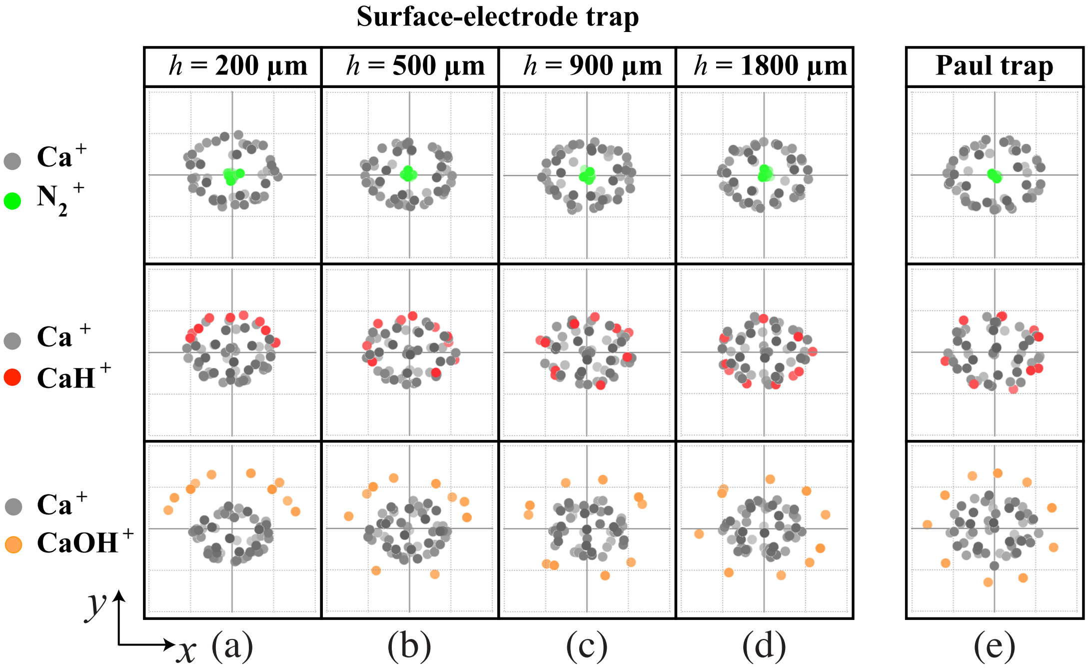

Figure 4.11: (a)-(d) MD simulations of bicomponent crystals containing 50 Ca^+ ions and 10 molecular ions in SE traps with different trapping heights from Fig. 4.10. The figures show snapshots of the ion positions viewed along the z axis and taken near the end of the simulation period. The λ_{3y} values calculated for trapping potentials in (a)-(d) are -68, -170, -307, -614 μm, respectively. (e) For comparison, the same crystals have also been simulated in a linear Paul trap. The vertical and horizontal lines in the figures indicate separations of 10 μm.

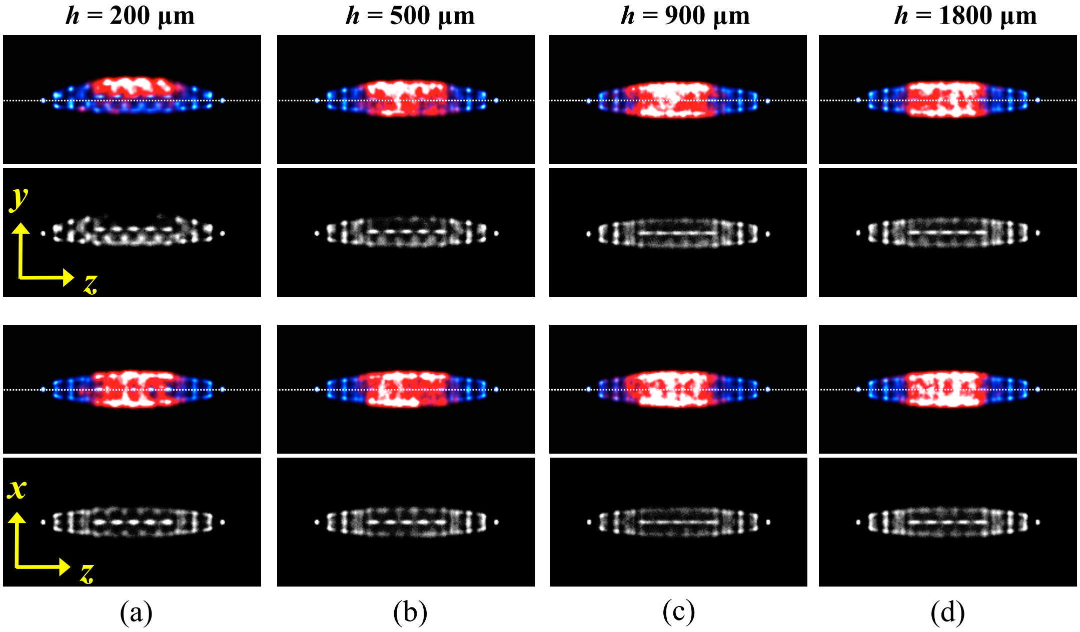

Figure 4.12: Images reconstructed from ion trajectories obtained from molecular dynamics (MD) simulations for 50 Ca^+ ions and 10 CaH^+ ions in the SE traps studied (Fig. 4.10), labelled with their trapping height h. The sympathetically cooled molecular ions in the mixed-species crystals are shown in colour images. Colour code: Ca^+: blue and CaH^+: red. The laser-cooled ions are also separately displayed in black and white images for clarity. The top (bottom) panel shows the crystals in the yz (xz) plane perpendicular (parallel) to the electrode surface. The white dotted line help guide the eye. See Fig. 4.8 for the definition of the coordinate axes.

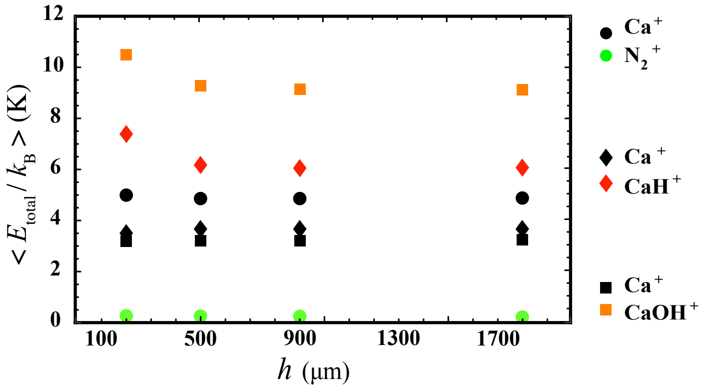

Figure 4.13: Average total kinetic energies of the Coulomb-crystallised ions in SE traps with different trapping heights shown in Fig. 4.11

considered.

The structural effects in the yz plane and xz plane are illustrated in Fig. 4.12 for the case of 10 CaH^+ and 50 Ca^+ laser-cooled ions. These images were reconstructed from the ion trajectories obtained from MD simulations, whilst assuming the same imaging system as in our experiments (Section 3.2.2), and the position of ions were averaged over the last 1000 RF periods (Section 2.6.2). In addition to the segregation of different ionic species (Fig. 4.11), the asymmetry of the trapping force leads to the stiffening of the crystal along the side parallel to the electrode plane (top panel Fig. 4.12 (a)). Because λ_{3x} is five times larger than D, the asymmetries have no evident effect in the yz plane parallel to the surface of electrodes (bottom panel Fig. 4.12 (a-d)).

The effects described above relate to the strength of anharmonic terms as a function of the size of the SE structures at fixed harmonic frequencies. One should also note that such effects also depend on the trapping conditions, e.g., RF frequency and amplitudes, as well as static control fields. These have not been characterized in the present study.

The average total kinetic energies of the Coulomb-crystallised ions in Fig. 4.11 are displayed in Fig. 4.13. The total kinetic energies are dominated by the contribution from the ion micromotion and therefore from their distance from the RF null line. The energies of the different ion species are essentially the same in the traps with $h = 900$ μm and 1800 μm. As these traps can be regarded as harmonic for the sizes of the crystal of Fig. 4.11, the ion kinetic energies are only weakly affected by potential anharmonicities. However, for the smaller traps with $h = 500$ μm and 200 μm, an increase in ion energies can be observed particularly for heavy sympathetically cooled species. This effect is a consequence of the increasing role of anharmoncity with decreasing trap size which displaces heavy sympathetically cooled species farther from the RF null line (see, e.g., Fig. 4.11 (a) for $CaOH^+$) and therefore exhibit wider micromotion amplitudes.

4.5 Anharmonicity in the six-wire SE trap

The characteristics of the comparatively large trap used in the present experiments were similar to the one with trapping height $h = 1800$ μm characterised in Figs. 4.10 to Fig. 4.13. Anharmonicity parameters λ_n (Eqn. 4.2) were calculated from power series fitted to one-dimensional cuts through the total potential $\Phi_{\mathrm{t}}(x_i)$ in a region of 400 μm around the trap centre. The parameters along the y axis were obtained to be $\lambda_{3y}= -750$ μm and $\lambda_{4y}= 890$ μm. The anharmonicity parameters along the x and z axes were about two orders of magnitude larger. Moreover, the voltage configurations used in the experiments resulted in Coulomb crystals with typical extensions <100 μm along the most asymmetric direction y so that anharmonic effects did not play a role in our experiments. This is illustrated in Fig. 4.14 which depicts the region of validity of the harmonic approximation for the present trap in relation to the size of a typical large crystal in our SE trap. Thus, for practical purposes the trap used in the present study can be regarded to be harmonic in a good approximation.

4.6 Summary and conclusions

This chapter has presented an investigation of the structural and energetic properties of bicomponent Coulomb crystals in a SE ion trap. Crystal shapes and ion energies were characterized by comparisons of experimental laser-cooling fluorescence images with MD simulations. Methods for spatially separating the ion

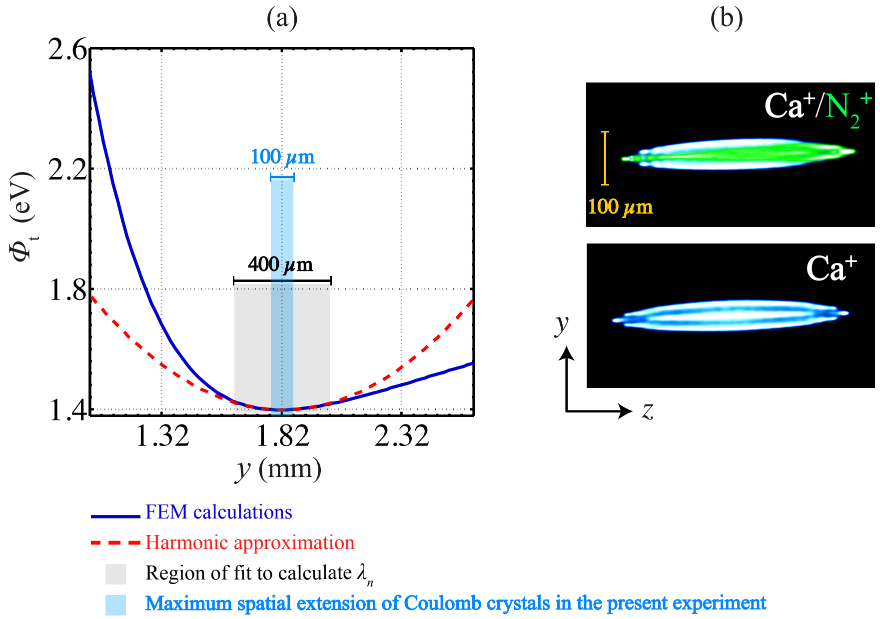

Figure 4.14: (a) Validity of the harmonic approximation in the present SE trap. (a) One-dimensional cut through the total potential Φ_t for Ca^+ ions along the vertical direction y near the trap centre. The anharmonicity parameters λ_n and trapping force coefficients were calculated in a region of 400 μm around the trap centre. (b) Side view of a typical large crystal containing 262 Ca^+ ions (bottom), 180 Ca^+ and 50 N_2^+ ions (top) showing a maximum spatial extension <100 μm along the vertical direction.

species in our experiments using static control fields were detailed and the effect of the separation on the crystal shapes and ion energies were discussed.

The effects of trap anharmonicities on the shapes and energies of bicomponent crystals were explored. Anharmonicity can have pronounced effects on the structure of bicomponent crystals. It was concluded that anharmonicities appreciably affect the crystal properties in small to medium-sized traps when the spatial extension of ions becomes comparable to the smallest anharmonicity parameter, but can be neglected in large, millimetre-sized traps such as the one used in our experiments. However, using sufficient degrees of freedom offered by two-dimensional geometry as well as applied voltages, the trapping potential can be engineered so that anharmonic terms are effectively eliminated. The trap geometry and the applied voltages can be designed to suppress such effects.

Moreover, the present study demonstrates that anharmonicity in the trapping potentials can deliberately be engineered to spatially separate ion species in bicomponent crystals.

Chapter 5

Design of a multi-functional surface-electrode ion trap

5.1 Highly integrated experiments on a single-layer chip

This chapter discusses the design of a multi-functional surface-electrode RF ion trap that has been developed to enable experiments with cold molecular ions using a monolithic chip device. The goal was motivated by the opportunity of integrating multiple trapping zones, the possibility of precisely shaping, as well as fabricating, electrodes, and the scalability of the structure in microfabricated SE traps. Therefore, the chip was designed to enable the performance of various tasks such as loading and preparation of ions, mass spectrometry, spectroscopy, reaction studies, and manipulation of the structure of Coulomb crystals in a monolithic miniaturized device using precisely shaped trapping potentials. The chip features carefully engineered ion channel intersections that enable transporting sympathetically cooled molecular ions in the form of bicomponent Coulomb crystals.

The key elements that must be realized for developing such a chip are the design and optimisation of junctions (Section 2.5.2). This work focuses only on surface-electrode junctions, benefiting from the flexibility of planar structures and capitalizing on the potentials offered by such new trapping architectures.

Furthermore, SE junctions can also be divided into two classes: first those designed to enable the proper intersection of quadrupolar ion channels using multi-dimensional trap arrays featuring three- or four-fold symmetry [90, 156–159, 187], and second those which facilitate smooth reshaping of trapping fields along one-dimensional arrays, referred to as field-modifying junctions [151].

The chip consists of quadrupolar and octupolar SE traps and two optimised SE junctions. The first is a cross between four quadrupolar channels, while the second is a connection between a quadrupolar channel and an octupolar region. Figure 5.1 illustrates the layout of this chip. In the following, the optimisation of the electrode geometry is discussed and it is concluded with the final design of the chip.

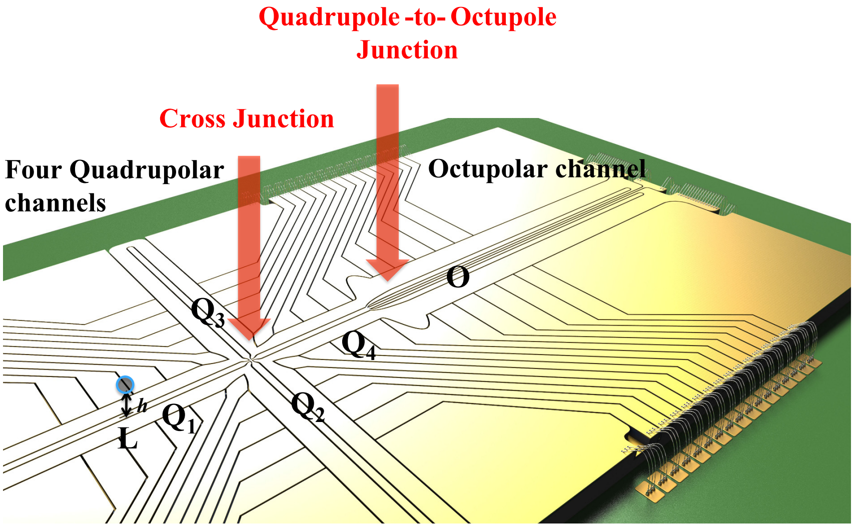

Figure 5.1: The overall layout of the multi-functional ion trap chip. **L** indicates the loading zone where ions are trapped at a height of h above the surface. The four quadrupolar channels are labelled with $\mathbf{Q}_1$, $\mathbf{Q}_2$, $\mathbf{Q}_3$, and $\mathbf{Q}_4$, and are connected via a cross junction. A quadrupole-to-octupole field junction along the fourth quadrupolar arm transforms the trapping field into an octupolar region **O**.

5.2 Multi-objective optimisation of the structure

The concepts and tools used to optimise the geometry of the chip are discussed in this section. In the context of ion trapping, the optimisation of trap geometries has been applied to: junction structures for enabling cross shuttling and reordering ions [90, 156], ion trap lattices as for quantum simulators [123, 188, 189], electrode configurations for fast separation of ions [91] as well as for minimising anharmonicities and improving trap stiffness [134], DC electrodes for adiabatic transport [190]. In this study, the focus is on the first category.

Transporting ions through SE junctions requires the minimisation of several factors: the height of pseudopotential barriers (see Section 2.5.2) and gradients, the variation of the trapping height, and the variation of axial secular trapping frequencies along ion channels. Therefore, it becomes indispensable to consider a multi-objective optimisation (MOO) process that deals with all requirements simultaneously.

Solving a typical MOO consists of the following steps [191]. First, a number of independent parameters are chosen to define a feasible design space. Second, the constraints are specified. Third, merit functions which represent physical quantities are determined. At this stage, numerical or analytical methods are decided upon. The main task is then conducted by an optimisation algorithm which searches for a global minimum within the design space by systematically changing parameters. These elements are specified in conformity with the geometry optimisation of the chip and are subsequently discussed in 5.2.1, 5.2.2, 5.2.3, and 5.2.4.

A two-step optimisation process was applied to each component that has been assembled on the final chip. In the first optimisation, the potential generated by SE electrodes was calculated using *SurfacePattern* package [179] based on analytical calculations in the "gapless plane" approximation (see Section 2.6.1). These calculations were performed in a close collaboration with Roman Schmied who also developed a *Mathematica* routine for the optimisation of the junctions. The high efficiency of these calculations in terms of time and memory consumption enabled many iterations, and hence, some of the generic aspects of junction geometries were explored. More importantly, the solutions obtained served as starting points for further optimisation as described below.

Due to weakly confining potentials at ion channel intersections the effect of gaps can not be neglected, and therefore, re-optimisation of the structure in the presence of the gaps was essential. Thus the geometries obtained from the first optimisation served as starting points for the second in which electric potentials generated by three-dimensional structural models including gaps were simulated using finite element method (FEM) in *COMSOL* [182] (Section 2.6.1), while the post-processing was performed in *MATLAB* using the *LiveLink*^{TM}*forMATLAB* module. The above mentioned terminology is extensively used to refer to these two distinct calculations.

5.2.1 Design space

In this study, the design space refers to a set of parameters defining RF electrode geometries to be used in optimisation processes. This section focuses on the design space of the cross junction in the first optimisation; however, the developed toolbox can be simply generalized to the other calculations presented. As illustrated in Fig. 5.2, RF electrode shapes in a typical cross junction can be specified by sets of control points. The numbers and locations of these points were varied according to the three methods used.

The first approach utilized four control points where two points on each perimeter are connected simply via a line as depicted in Fig. 5.2 (i). This straightforward choice of only four parameters facilitated many iterations of optimisation processes and despite a low number of degrees of freedom led to reasonable solutions (see Section 5.3.2).

In the second approach (Fig. 5.2 (ii)), the inner and outer RF electrode edges were broken up into several line elements. The locations of the control points at which these line elements are connected were used as optimisation parameters and linked via a given distance Δ and length L. We began with four control points and increased them up to 20 points while aiming for improved results and/or for properly shaped electrodes without acute angles. Careful attention must be paid when increasing the number of degrees of freedom because it does not necessarily result in better solutions because of the higher probability of

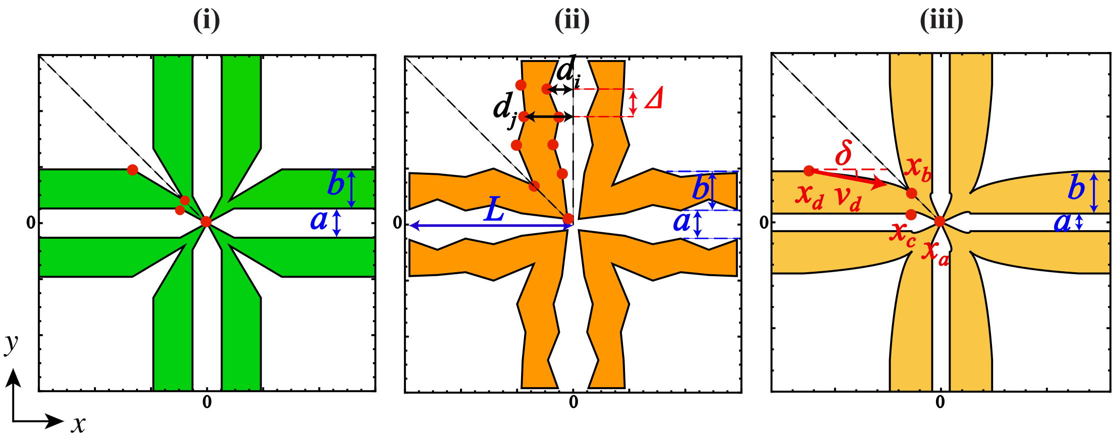

Figure 5.2: Parametrisation of the cross junction geometry for the first optimisation processes. In (i-iii), the RF electrodes are shown in colour, the red points indicate the control points, and a and b are the width of central DC and RF electrodes, respectively. The control points on the inner and outer perimeter are connected via lines in (i), line elements defined by d_i, their distance $\mathit{\Delta}$, and involved length L in (ii), and splines in (iii). In (iii), each red point assigned with its abscissa represents three degrees of freedom, and thereby, the geometry was fully defined by $\{x_d, a/2+b, v_d, \delta\}$, $\{x_c, a/2, v_c, \gamma\}$, $\{x_a, x_a, v_a, \alpha\}$, and $\{x_b, x_b, v_b, \beta\}$ (see Fig. 5.3 for details). Note that only one eighth of the geometry was parametrised due to four-fold rotational symmetry combined with reflection in every cross junction as highlighted by dashed lines.

getting trapped in local minima.

This method of parametrisation has been widely used [90, 151, 156, 158, 159, 192]. However, the electrode structure obtained might exhibit very sharp features arising from underdetermined geometrical constraints. At a given height z above the surface, the Fourier components of the surface potential exponentially decrease with z on the length scale of electrode dimensions [124], and consequently, sharp elements which are much finer than z have no clear influence on the trapping field. Such sharp structures, see Ref. [156, 158], might hinder precise manufacturing and would reduce breakdown voltages through the bulk or surface flashover.

Figure 5.2 (iii) illustrates the third approach used to mitigate such issues by using splines to define the design space. A detailed description given in Fig. 5.3 shows that the number of control points on each perimeter were increased to

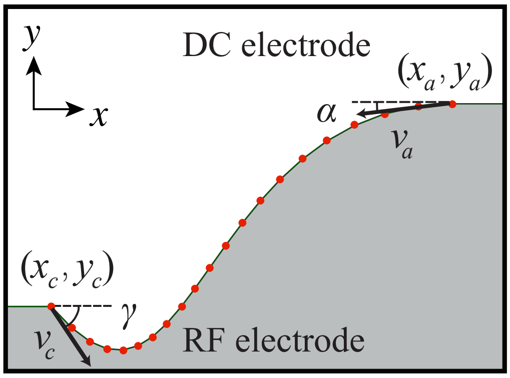

Figure 5.3: A schematic of a spline forming an RF electrode edge. The locations of 21 control points shown in red are given by 8 parameters $\{x_a, y_a, V_a, \alpha\}$, $\{x_c, y_c, V_c, \gamma\}$, which are the positions of the initial and final points, and the amplitude as well as the orientation angle of the first derivatives at these points.

21 while they are bound to a spline specified by eight parameters. Because of reasons of symmetry, the number of parameters for each spline was eventually reduced to six, and thus the geometries of the cross junction were given by 12 parameters. This method of parametrisation was found to be sufficiently flexible as well as efficient and was mainly used in the first optimisation.

The parametrisation of geometries in the second optimisation was chosen with two to four parameters specifically chosen for each part and is presented with obtained results in each section.

5.2.2 Constraints

An important theme of any optimisation problem is the way in which the design space is restricted, i.e., the determination of constraints. Proper constraints facilitate search procedures and improve results by avoiding impractical electrode structures as discussed in the previous section. Constraints can be categorized as:

(1) Physical constraints: defined by the laws of physics and symmetries, such as the Laplace equation.

(2) Geometrical constraints: defined by possible trap structures.

(3) Practical (or user) constraints: defined by practical limits such as breakdown voltages and manufacturing methods.

(4) Application constraints: defined by the user based on particular applications. Designing certain trapping frequencies and accommodating design constraints arising from the combination of different functionality are two examples of this category.

In the first optimisation, the constraints were set to avoid sharp edges and overlaps of the electrodes. Care should be taken not to restrict the design space too rigorously at this stage. In the second optimisation which deals with real structures, we focused more on the user and application constraints.

5.2.3 Objective functions and weighted sum method

A key aspect of the optimisation processes demonstrated in this work is a multi-objective optimisation. A variety of objective functions can be considered [90, 156, 158, 192], and the question arises about which physical quantities are relevant when designing for certain applications. The SE junctions that has been experimentally tested thus far were optimised with respect to the following objectives [90, 156, 158, 159]:

(1) Pseudopotential barriers
(2) Pseudopotential gradients
(3) Variation of the trapping height
(4) Variation of the curvature of trapping potentials

In the following, we justify the necessity of utilizing each of these objectives in accordance with requirements for shuttling bicomponent Coulomb crystals, whilst it is notable that these functions are not independent, necessitating a MOO.

(1) As discussed in Section 2.5.2, straight RF electrodes intersecting at right angles yield non-confining trapping potentials perpendicular to ion paths, i.e., substantial pseudopotential barriers that impede ion transport [155]. Thus, the suppression of these barriers is crucially important in general for any intersection. In addition, ions of different masses are subject to different pseudopotential barriers. Note that the position of pseudopotential minima, where the RF field

vanishes, solely depends on the trap geometry, and therefore, is identical for all ion masses. Consequently, the segregation of laser-cooled and co-trapped sympathetically cooled ions may occur which would potentially lead to insufficient sympathetic cooling and large loss rates of molecular ions. Therefore, the height of pseudopotential barriers was the most important quantity to be minimised and was treated with large weighting factors in our calculations.

(2) The axial pseudopotential gradient that causes ion heating must be suppressed for reliable shuttling of qubits [90, 156–159], since at intersections where noise on the RF potential is present axial motional modes of ions might be excited. Thus, for applications in quantum computation, the minimisation of the pseudopotential gradient is prevalent. This quantity has been used although not with the top priority in accordance with our application.

(3) In principle, there are two important reasons to control the variation of the trapping height. First, weakly confining potentials at SE intersections might cause ions to fall onto the surface. This issue can be mitigated by using static fields such that ion channels are deliberately formed closer to the surface. This is at the expense of moving the trapping minima away from the pseudopotential null at the center such that the static potential forces ions to circumnavigate the junction center [158]. This technique is unsuited for bi- and multi-component Coulomb crystals because of the drastic segregation of ionic species under the influence of such a static field (Section 4.3). Second, the goal was the transportation of molecular ions together with co-trapped laser cooled atomic ions in the presence of cooling beams, and thus, variations of the trapping height larger than that of two times the beam waist should be avoided.

(4) Another approach to near-motional-ground state shuttling of ions is to minimise the variation of the axial potential curvature [159]. This objective function is again of importance for applications in quantum information processing, and hence, was not used in the calculations.

Therefore, the objective functions were given by:

$$F_1 = \varPhi_{\text{ps}} \mid_{min(\varPhi_{\text{ps}})}, l \in [-l_{max}, 0] \tag{5.1a}$$

$$F_2 = \parallel \frac{\partial \varPhi_{\text{ps}}}{\partial l} \mid_{min(\varPhi_{\text{ps}})} \parallel^2, l \in [-l_{max}, 0] \tag{5.1b}$$

$$F_3 = \parallel (z \mid_{min(\varPhi_{\text{ps}})}) - h \parallel^2, l \in [-l_{max}, 0] \tag{5.1c}$$

Here, F_i (i=1, 2, 3) denotes the ith objective function, $\varPhi_{\text{ps}}$ is the pseudopotential, l is the coordinate along the ion channel, l_{max} is the coordinate of the initial trapping zone, and h is the intended trapping height.

A relatively fast and easy-to-implement method of solving MOO problems is the weighted sum method in which a so-called scalarized function U is minimised [193]:

$$\begin{aligned} U &= \sum_{i}^{n=3} w_i[\xi_i F_i(d_1, ..., d_m)] \\ &= \{w_1\xi_1, w_2\xi_2, w_3\xi_3\} \cdot \{F_1, F_2, F_3\} \end{aligned} \tag{5.2}$$

Here, w_i>0 (i=1, 2, 3) is the weighting factor for the ith objective function F_i which determines a comparative contribution specifing the user's preference. More importantly, the $lower - bound$ transformation method [193], was used to ensure F_{1-3} have similar order of magnitude, and so, are comparable in numerical calculations. Thereby, the transformation coefficient ξ_i (i=1, 2, 3) was given by:

$$\xi_i = \frac{1}{F_i^0}, \tag{5.3}$$

where F_i^0 = minimum $\{F_i(d_1, ..., d_m)\}$. As highlighted by Eqn. 5.2, it is important to notice a subtle distinction between using weights to determine the user's preferences and using weights to transform objective functions. Although these two numbers can be multiplied to form a single scaling coefficient for each objective function, these two types of weights have separate roles and are determined in different ways. ξ_i is calculated using Eqn. 5.3 by computing the minimum of each objective function individually, while w_i is an arbitrary value systematically varied in the interval [0,1] to set the relative importance of the objectives.

It is beneficial to use normalized (non-dimensional) objective functions F_i. Consider a total trapping potential in the pseudopotential approximation while DC electrodes are grounded:

$$\begin{aligned}\Phi_{\mathrm{total}}(x,y,z) &= \Phi_{\mathrm{ps}} + \Phi_{\mathrm{DC}} \\ &= \frac{q^2 V_{\mathrm{RF}}^2}{4\ m\Omega_{\mathrm{RF}}^2}\ \|\nabla\phi_{\mathrm{RF}}\|^2 + \underbrace{q\sum_i^n V_i\phi_{i,\mathrm{DC}}}_{0} \\ &= \frac{q^2 V_{\mathrm{RF}}^2}{4\ m\Omega_{\mathrm{RF}}^2}\ \frac{1}{h^2}\ \underbrace{\|\nabla\Theta_{\mathrm{RF}}\|^2}_{\text{geometrical factor}}\ .\end{aligned} \tag{5.4}$$

Here, m and q are the mass and charge of the trapped ions, and V_{RF} and Ω_{RF} denote the RF amplitude and frequency respectively. $\phi_{\mathrm{RF}}(\phi_{\mathrm{DC}})$ denotes the RF(DC)-electrode-potential basis function. Note that the non-dimensional geometrical factor $\|\nabla\Theta_{\mathrm{RF}}\|^2$ depends solely on the electrode structures and so a non-dimensional pseudopotential can be written as:

$$\widetilde{\Phi}_{\mathrm{ps}} = \frac{\Phi_{\mathrm{ps}}}{\frac{q^2 V_{\mathrm{RF}}^2}{4\ m\Omega_{\mathrm{RF}}^2 h^2}} = \frac{\Phi_{\mathrm{ps}}}{\Phi_{\mathrm{ps0}}} = \|\nabla\Theta_{\mathrm{RF}}\|^2.$$

Based on this formalism, the objective functions in Eqns. 5.1 can be expressed as:

$$F_1(\widetilde{d}_1,...,\widetilde{d}_m) = \widetilde{\Phi}_{\mathrm{ps}}\ |_{min(\widetilde{\Phi}_{\mathrm{ps}})}, \widetilde{l}\in[-l_{max},0] \tag{5.5a}$$

$$F_2(\widetilde{d}_1,...,\widetilde{d}_m) = \|\ \frac{\partial\widetilde{\Phi}_{\mathrm{ps}}}{\partial\widetilde{l}}\ |_{min(\widetilde{\Phi}_{\mathrm{ps}})}\|^2, \widetilde{l}\in[-l_{max},0] \tag{5.5b}$$

$$F_3(\widetilde{d}_1,...,\widetilde{d}_m) = \|\ (\widetilde{z}\ |_{min(\widetilde{\Phi}_{\mathrm{ps}})}) - 1\ \|^2, \widetilde{l}\in[-l_{max},0], \tag{5.5c}$$

Here, the length parameters denoted with tilde are normalized by the trapping height h. As can be clearly seen from Eqns. 5.5(a-c), the objective functions, and hence, solutions of the optimisation are independent of the mass of ions as well as the trapping parameters. The trapping height, which is a characteristic length of the system, can be substituted in the final result. As a result, the geometries obtained present universal SE structures applicable to any mass or set of trapping parameters.

5.2.4 Optimisation algorithms

In MOO, a single set of parameters that simultaneously minimises all objective functions usually does not exist, hence, a *Pareto optimal* solution is searched among many possible solutions [191]. We performed optimisation processes based on direct search algorithms, also referred to as zeroth-order methods, which are asymptotically slower but more accurate than gradient-based ones. In the first optimisation, built-in algorithms were used in Mathematica, namely, "Simulated Annealing", "Differential Evolution", and "Nelder-Mead" algorithms [194], while in the second the search was performed by the simplex algorithm, trial and error, and scanning relevant design spaces.

5.3 Cross junction

5.3.1 Optimisation of quadrupolar channels

First of all, the geometries of RF rails in an infinite quadrupolar channel must be optimised. A 5-wire design with equal width RF electrodes is specified by the width of the central DC electrode a and that of RF electrodes b. These two parameters are linked via the trapping height at which the RF field vanishes given by $h = \frac{a}{2}\sqrt{1+2\frac{b}{a}}$. The optimal ratio value of $\frac{b}{a}$ can be calculated for a given a while maximising the trapping depth in the absence of control static fields (referred to as the intrinsic depth, that is, the value of pseudopotential at escape points) [114]. Due to the importance of the trapping height as a constraint in many experiments, Wesenberg optimised the intrinsic depth as well as the trap strength of SE traps for a given trapping height [124, 195]. In the present study, the curvature of the quadrupole field, which is proportional to the second derivatives of the RF potential at the trapping height in the plane perpendicular to the channel, were maximised [123]. Table 5.1 presents a

Table 5.1: Optimised electrode configurations for a typical 5-wire SE trap.

Reference	a	b/a	h	f
[114]	fixed	**1.19**	0.92 a	$\Phi_{\mathrm{ps}} \|_{escape}$
[124, 195]	$\frac{1}{1.43}\ h$	**3.68**	fixed	$\Phi_{\mathrm{ps}} \|_{escape}$
[123], this work	$(2\sqrt{2}-2)\ h$	**2.41**	fixed	$\frac{\partial^2 \phi_{\mathrm{RF}}}{\partial z^2} \|_h$

detailed comparison between these three calculations, highlighting the fact that the optimal $\frac{b}{a}$ in a five-wire design highly depends on the optimisation approach.

5.3.2 Optimisation of the cross junction using an analytical model

In light of the discussion presented in Section 5.2, the results of the first optimisation of the cross junction are demonstrated. The geometries, as given in Fig. 5.4 and Fig. 5.5, were selected from over 160 calculations in which design spaces, weighting factors, and/or optimisation algorithms were varied.

The solution shown in Fig. 5.4 (i) was selected from a set in which the constraint given in Table 5.1 was released, i.e., the ratio $\frac{b}{a}$ served as an optimisation parameter. The obtained structures feature narrow RF electrodes sharply tapered towards the center with much smaller values of $\frac{b}{a}$ than those given in Table 5.1, as seen in the sample result in Fig. 5.4 (i) (a). These solutions exhibit substantially suppressed pseudopotential barriers, but considerably shallower intrinsic depth in far channels. It can be correctly argued that the well-suppressed barriers arise from a small ratio $\frac{b}{a}$, and correspond to a general reduction of the pseudopotential over the region, while, the ratio of the pseudopotential barrier height to the trap depth in far channels remains the same. Such a choice of an electrode ratio can be seen in *Cross Junction* [158] and *Satellite Trap* design [159]. In comparison, for the given ratio $\frac{b}{a} = 3.68$ (Table 5.1), the optimised junction exhibits higher pseudopotential barriers while the trapping depth in the far channel was calculated to be almost three times greater, see Fig. 5.4 (ii) (a-c).

To assess the minimisation of pseudopotential barriers, a suppression factor is defined as the ratio between the height of the suppressed barriers and either those of the straight junction or the intrinsic depth in far channels. In either way, this factor is independent of the ratio $\frac{b}{a}$. Thus, it is advisable to fix the ratio $\frac{b}{a}$ to an optimised value, as discussed in 5.3.1, and use the degrees of freedom in the vicinity of the center to repress barriers. This approach was employed in this study with $\frac{b}{a}$ set to 2.414 (Table 5.1), see also the example result in Fig. 5.4 (iii).

More flexibility for altering electrode geometries was offered by the line element design space with 5 to 21 control points. Consequently, optimised geometries exhibited lower barriers, as can be seen in Fig. 5.4 (iv). In addition, the geometry shown in Fig. 5.4 (iv) shows a particularly important feature given by the four tiny DC patches near the center. This is in agreement with the *X junction trap* designed by Bjeorn Lekitsch, who proposed the idea of combining an octupolar cross junction with a quadrupolar one to suppress pseudopotential barriers effectively by means of incorporating such diagonally-located, small DC patches [187, 196]. However, that solution was found by trial and error, while the presented result was directly obtained from straightforward single-objective optimisation process using 11 parameters. Note that the implementation of such DC patches requires vertical interconnect accesses (VIAs) [197].

As discussed in Section 5.2.1, most calculations were performed using the spline design space (Fig. 5.2 (iii) and Fig. 5.3). Example results are shown in Fig. 5.5 (i)-(iv). The transformation coefficients were calculated to be $\{\xi_1, \xi_2, \xi_3\} = \{1.59\times10^{-6}, 6.1\times10^{-12}, 1\times10^{-4}\}$ associated with pseudopotential barriers and gradients, and the trapping height variation, respectively. The corresponding weighting factors $\{w_1, w_2, w_3\}$ can be set differently for each given interval along the ion channel. This leads to a dramatically increased number of possible alternatives, however, no significant improvement was achieved. Figure. 5.5 (ii) provides an example, in which the objective functions were weighted differently in two intervals. Therefore, weighting factors were set as a constant value along the channel in each calculation. Notice that the minimisation of pseudopotential barriers occurred at the cost of large trapping height variation and vice versa. For this reason, it is important to properly scan weighting factors. In conclusion,

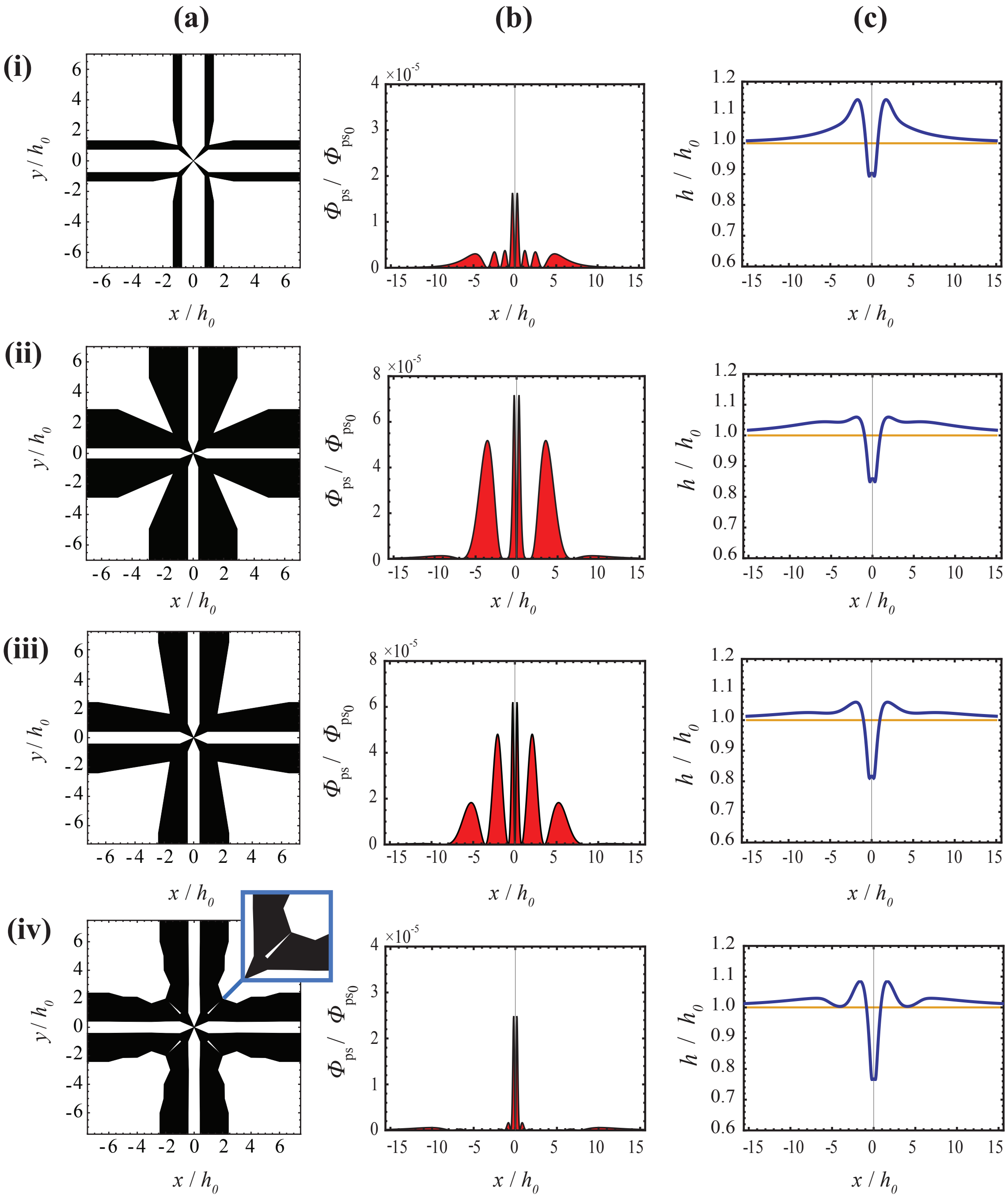

Figure 5.4: (i-iv) Results of the first optimisation. (a) Optimised geometries. (RF (black) and DC (white) electrodes). (b) Pseudopotential barriers along ion channels. (c) The height of trapping. Note that the units were normalized. Parametrisation of the electrodes were based on the line design space in (i-iii) and line elements design space in (iv). The inset in (iv) magnifies a diagonally located DC patch.

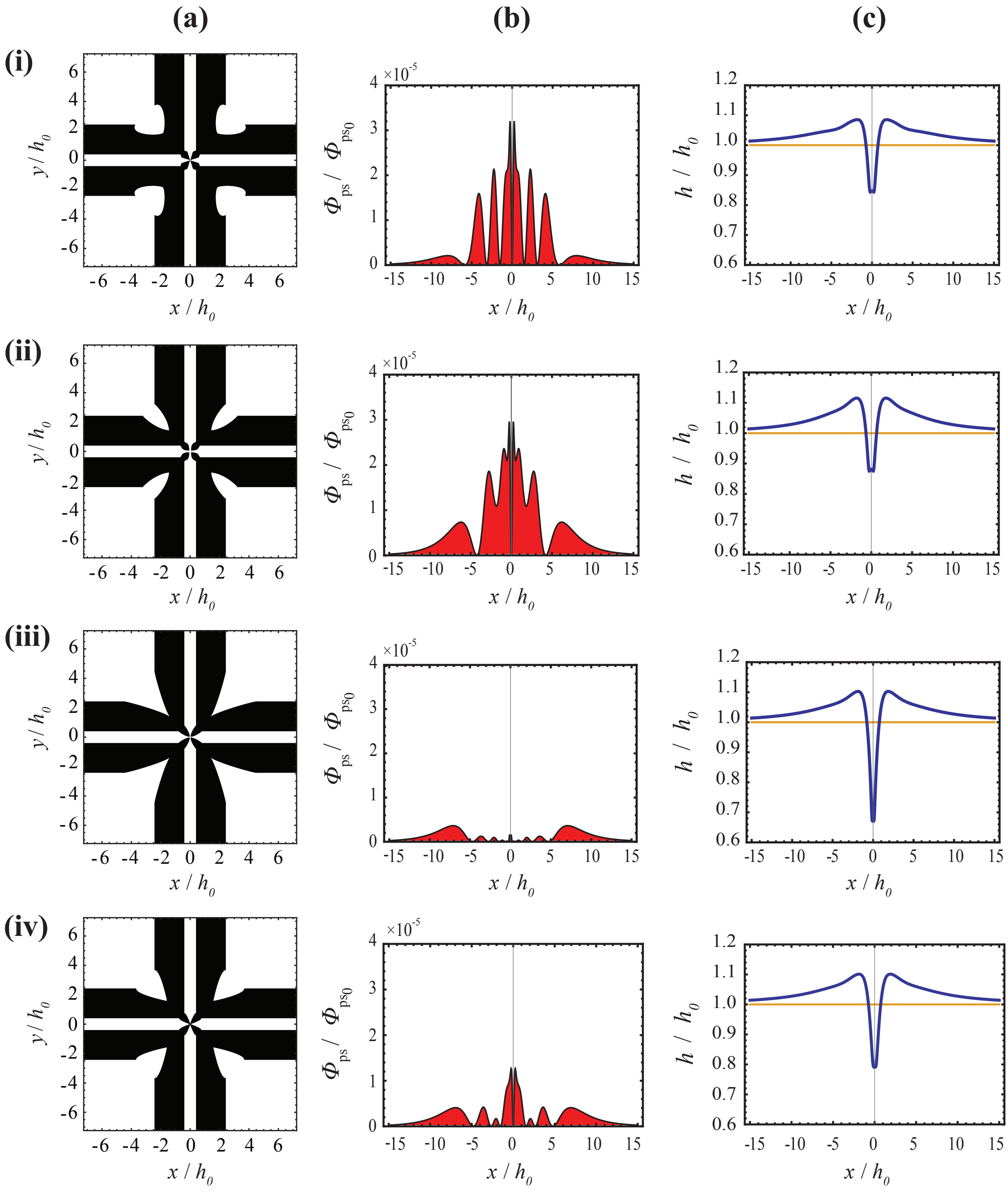

Figure 5.5: (i-iv) Results of the first optimisation. (a) Optimised geometries (RF (black) and DC (white) electrodes). (b) Pseudopotential barriers along ion channels. (c) The height of trapping. Note that the units were normalized. Parametrisation of the electrodes were based on the spline design space in (i-iv). The weighting factors $\{w_1, w_2, w_3\}$ for (i)-(iv) were {0.25, 0.25, 0.5}, { {0, 0.5, 0.5}, {0.4, 0.2, 0.4} }, {0.375, 0.625, 0}, {0.2, 0.6, 0.2}, see text for details.

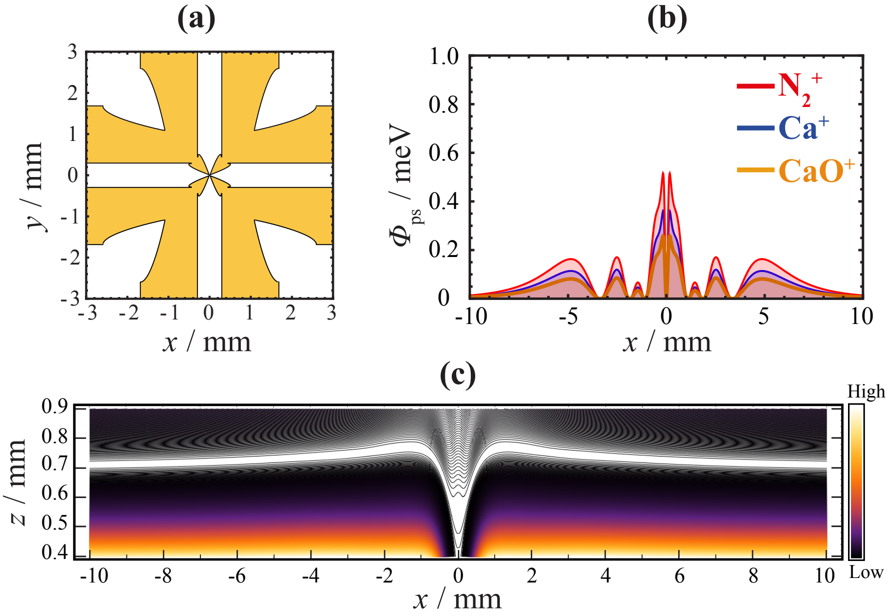

Figure 5.6: (a) The cross junction geometry obtained from the first optimisation (RF (yellow) and DC (white) electrodes). (b) The pseudopotential barriers along the ion channel for N_2^+, Ca^+, and CaO^+. (c) The pseudopotential profile for $^{40}Ca^+$ in the (x,z) plane. The white path corresponds to isopotential contours of Φ_{ps}<0.8 meV.

the two structures shown Fig. 5.5 (iii) and (iv) were used as starting points for the second optimisation.

The solution in Fig. 5.5 (iv) was adapted to h=700 μm (Fig. 5.6 (a)), and the trapping potential was evaluated for the RF voltage $V_{RF(0-peak)}$=300 V and the RF frequency $\Omega_{RF}=2\pi \times 10.0$ MHz. In this case the highest barrier for $^{40}Ca^+$ is 0.36 meV, corresponding to a suppression factor of 614 with respect to the depth of 221 meV in the far channel, and of 125 with respect to the the straight intersection barriers. Additionally, the pseudopotential barriers for N_2^+ and CaO^+ along the channel are presented in Fig. 5.6 (b) showing, e.g., the barrier difference 0.2 meV in case of N_2^+ and Ca^+. The trapping height varies around 200 μm above the surface, see Fig. 5.6 (c).

The non-confining characteristic of trapping potentials at the intersection region also manifest itself in a drastic change of Q_{yy} and Q_{zz} parameters, defined in Section 2.1.1. Figure 5.7 illustrates the calculated values in the case presented

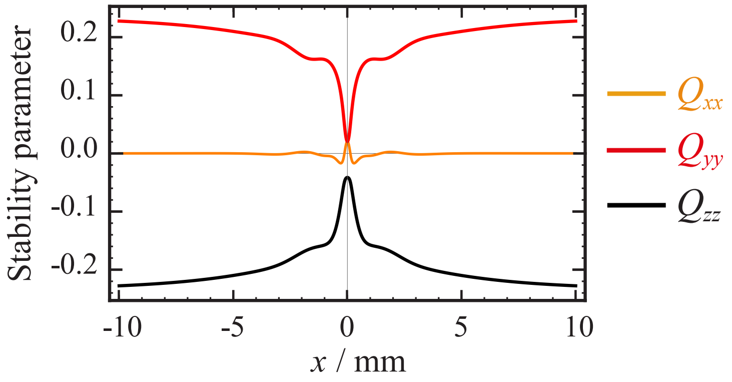

Figure 5.7: Stability parameters along the ion channel calculated for the junction shown in Fig. 5.6 (a).

in Fig. 5.6 using the same trapping parameters as indicated above.

The optimised geometries shared in the following generic aspects: first, RF electrodes tend to taper towards the center with very fine structure but never connected, and second, the characteristics of the intersection were extremely sensitive to any small modification at the center. The conclusion is that potential models in which gap effects are neglected are not sufficient to describe such junctions. Furthermore, the implementation of such optimal geometries is mainly restricted by the fabrication limitations (Section 6.2).

5.3.3 Second optimisation and characterization of a central bridge

The previous section provides an insight into the optimisation of the cross junction using the gapless plane approximation. Figure 5.8 (a) shows the optimal geometry with the inclusion of 120-μm wide gaps. Due to the 330-μm-diameter hole at the center, the pseudopotential exhibited a spatially broad, almost non-confining trapping region along z at the center as in Fig. 5.8 (b). Therefore, the challenge was to increase the stiffness of the trapping potential in this region so that the channel height variation and pseudopotential barriers simultaneously fulfil the requirements specified in Section 5.2.3.

Figure 5.10 shows an optimised geometry with a 30-μm wide DC bridge as

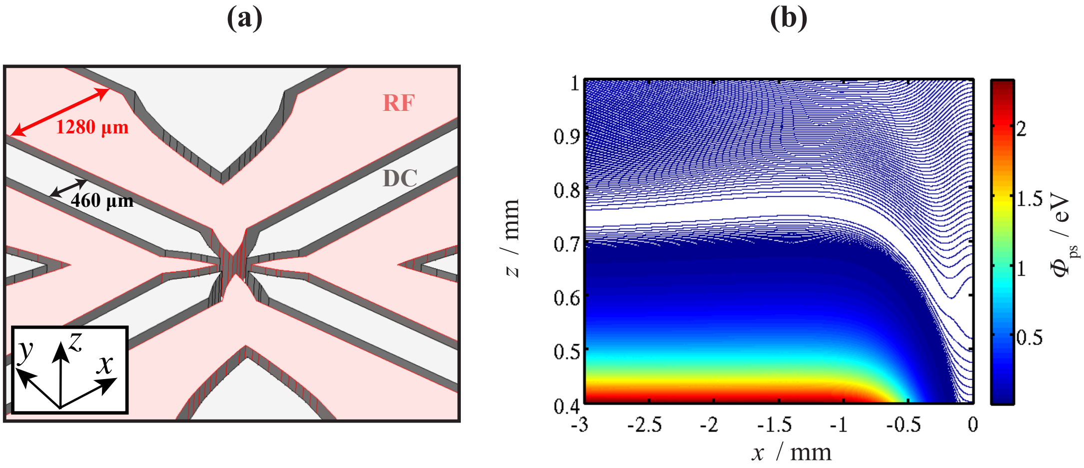

Figure 5.8: (a) The geometry of the cross junction obtained from the first optimisation after introducing gaps. (b) The pseudopotential in the (x,z) plane extracted from finite element analysis. The isopotential contours are separated by 1 meV and the central one indicates the 1-meV potential.

well as the corresponding pseudopotential for $^{40}\mathrm{Ca}^{+}$ at the RF voltage $\mathrm{V}_{\mathrm{RF(0-peak)}} = 300$ V and the RF frequency $\Omega_{\mathrm{RF}} = 2\pi \times 10.0$ MHz. It can be seen that such a bridge resolves the issue with the non-confining potential at the center. However, to increase mechanical stability of the structure and more importantly to avoid the risk of damaging fine features when applying voltages, the width of the bridge must be increased.

To address this issue, we investigated the incorporation of a central bridge with carefully refined geometry. To explore the consequences of this modification, over 120 geometries were modelled using FEM. Bridges formed by merging the tips of RF electrodes at the center cause extremely high pseudopotential barries as in Fig. 5.9 (a). This would lead to ions falling into the chip as displayed in the trapping height variation, see Fig. 5.9 (b). In this case, the RF field cannot be cancelled out at the center due to the lack of the symmetry in the vertical direction z. This situation is opposed to three-dimensional junctions, e.g., demonstrated in Ref. [145], where the RF bridge were located symmetrically above and below the ion channel. For this reason, the bridge must be constructed primarily from DC electrodes. Figure 5.9 displays the calculations

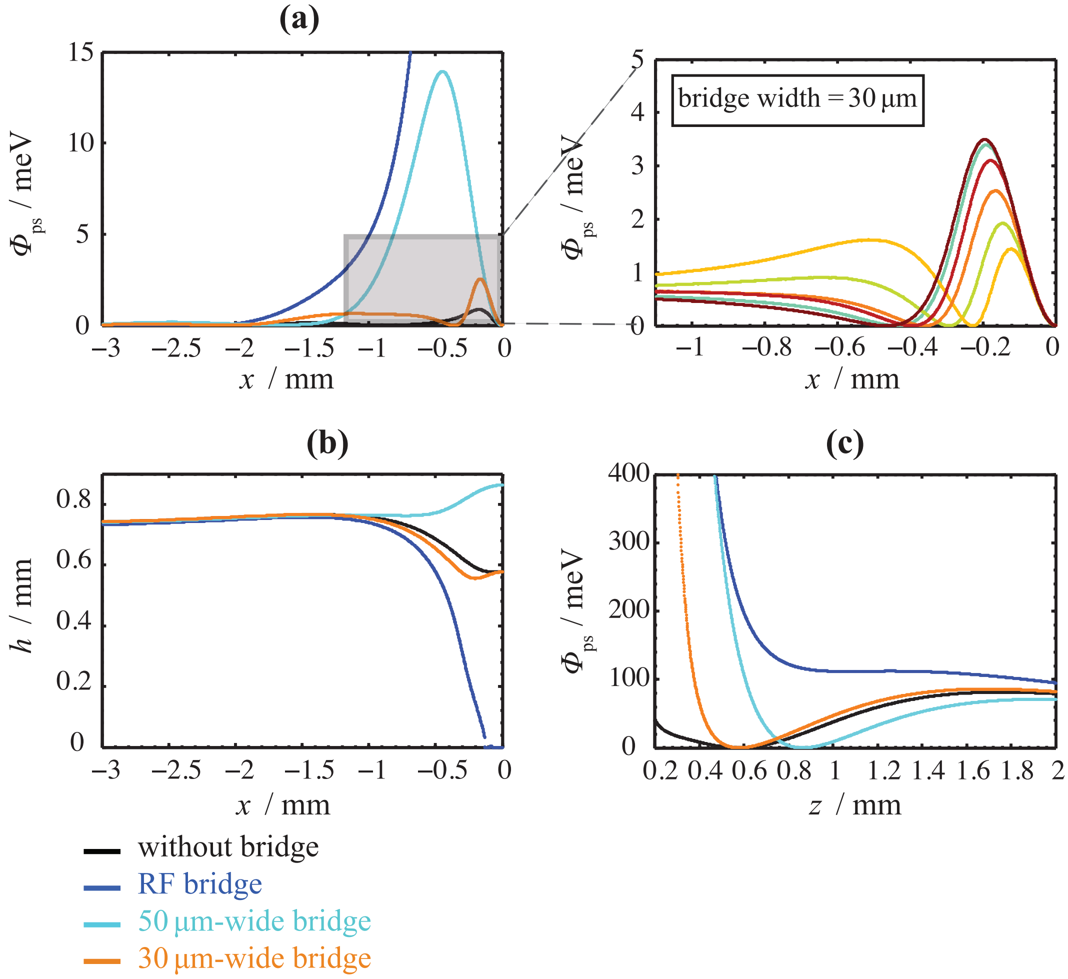

Figure 5.9: Characterization of the central bridge incorporated to the cross junction. (a) Pseudopotential barriers along ion channels. The inset shows a magnified view of the pseudopotential barriers calculated for a set of 30-μm wide DC bridges. (b) The variation of the trapping height. (c) One-dimensional cuts through pseudopotentials along the z axis at the center of each junction. In (a-c) the black curve is related to the structure without a bridge (Fig. 5.8), the dark blue curve shows calculations for a trial structure with a RF bridge, and the light blue and orange curves illustrate calculations for the structures with a 50-μm and 30-μm wide DC bridges, respectively.

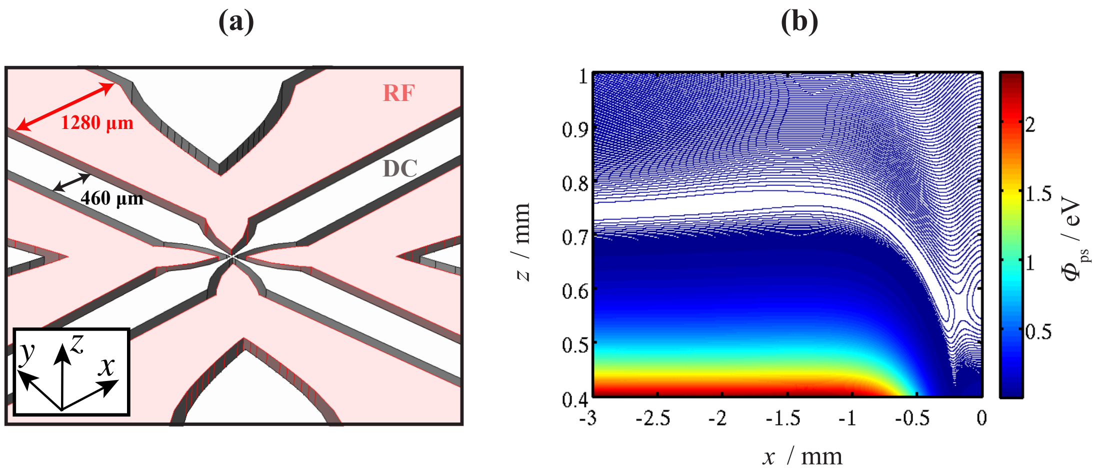

Figure 5.10: (a) The optimised geometry of the cross junction with a 30-μm wide DC bridge incorporated at the center. (b) The pseudopotential in the (x,z) plane deduced from finite element analysis. The isopotential contours are separated by 1 meV and the central one indicates the 1-meV potential.

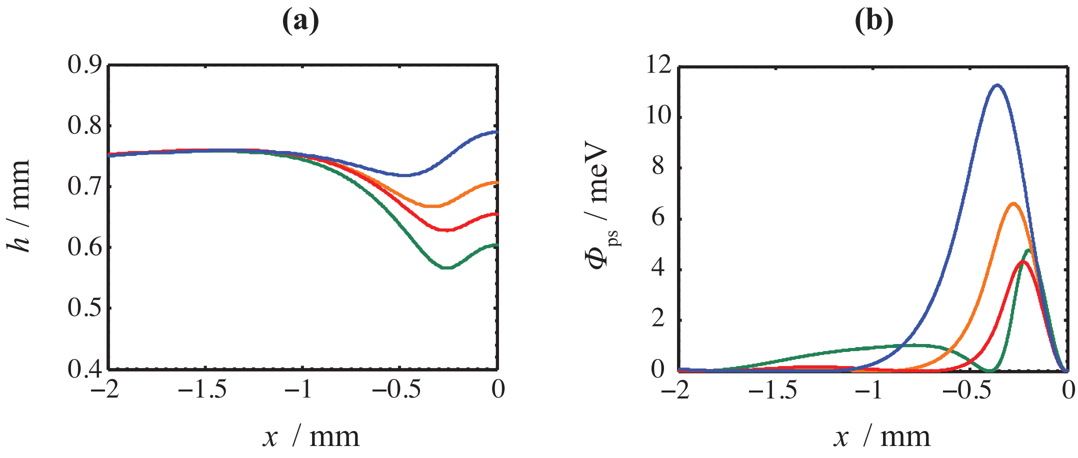

Figure 5.11: Results of finite element method calculations for four trial cross junction geometries, selected from over 40 designs, featuring a fixed 70-μm wide DC bridge at the center. (a) The variation of the trapping height. (b) Pseudo-potential barriers along ion channels.

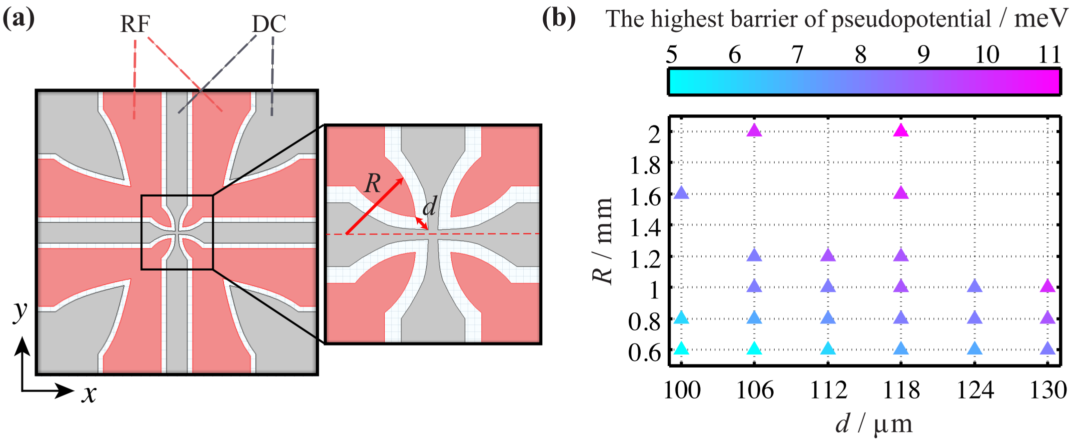

Figure 5.12: (a) Parametrisation of the RF electrodes in the vicinity of a fixed 70-μm wide DC bridge at the center of the cross junction. R and d indicate the radius of the bent structure and the width of the central gap, respectively. (b) Density plot of the highest barrier of pseudopotentials for varying geometries specified by d and R.

for several trial geometries indicating that pseudopotential barriers as well as the trapping height are very sensitive to the bridge width. For exmple, a 50-μm wide bridge causes 14 meV barriers, considerably lower than for the structures with a 30-μm wide bridge, as in Fig. 5.9 (a).

The bridge width was fixed to 70 μm, suitable for the fabrication method (Section 6.2), and the geometry was parametrised in the vicinity of the center. Further refinement was achieved by trial and error, and employing the simplex algorithm. These calculations enabled the suppression of pseudopotential barriers by a factor of three while the trapping height was controlled in a range of ±10%, see Fig. 5.11. Also, pseudopotential barriers reduce as the size of the gaps in the vicinity of the junction center decreases. This has been verified by the correlation between the radius of the bent RF electrodes R and the width of the central gap d shown in Fig. 5.12. Based on these calculations, the optimal geometry of the cross junction was concluded as presented in Fig. 5.13 (a), featuring a confining trapping potential perpendicular to the ion channel at the intersection (Fig. 5.13 (b)).

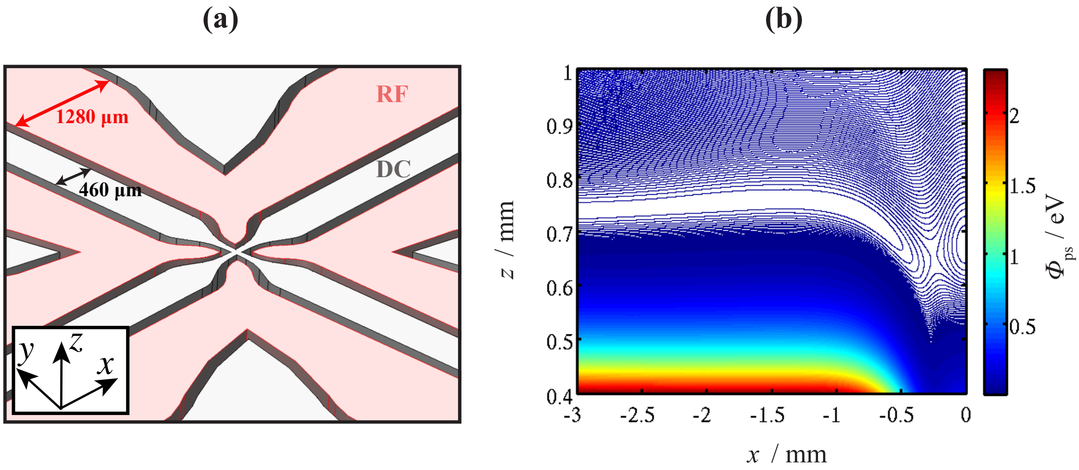

Figure 5.13: (a) The optimised geometry of the cross junction with a 70-μm wide DC bridge. (b) The pseudopotential in the (x,z) plane extracted from finite element analysis. The isopotential contours are separated by 1 meV and the central one indicates the 1-meV potential.

5.3.4 Conclusions

The characteristics of the main results for the cross junction discussed in the previous section are presented in Fig. 5.14. First and foremost, it has been shown that incorporating an optimised DC bridge at the center of the cross junction significantly increases the strength of trapping potentials (Fig. 5.14 (a)). As the bridge widens, the pseudopotential barriers drastically increase, and therefore, further calculations were done to enable using a 70-μm wide DC bridge. The final result exhibits barrier < 5.5 meV for $^{40}\mathrm{Ca}^{+}$ (Fig. 5.14 (b)). Further decrease of barriers was challenging due to the practical limitations (Section 6.2). The increase of the trap stiffness in the optimised bridge manifests itself in the greater Q_{zz} parameter (z is the direction perpendicular to the SE structure), i.e., improved by a factor of two, see Fig. 5.14 (c). The ion channel elevated at a well-controlled height over the whole path as displayed in Fig. 5.14 (d).

Finally, it should be noted that there is a mass dependence of the barriers as illustrated in Fig. 5.15 for several ion species. Although the barrier heights are five times larger than those of the the structure without a bridge, the stiffness of the tap at the intersection center is greatly increased, which is of importance

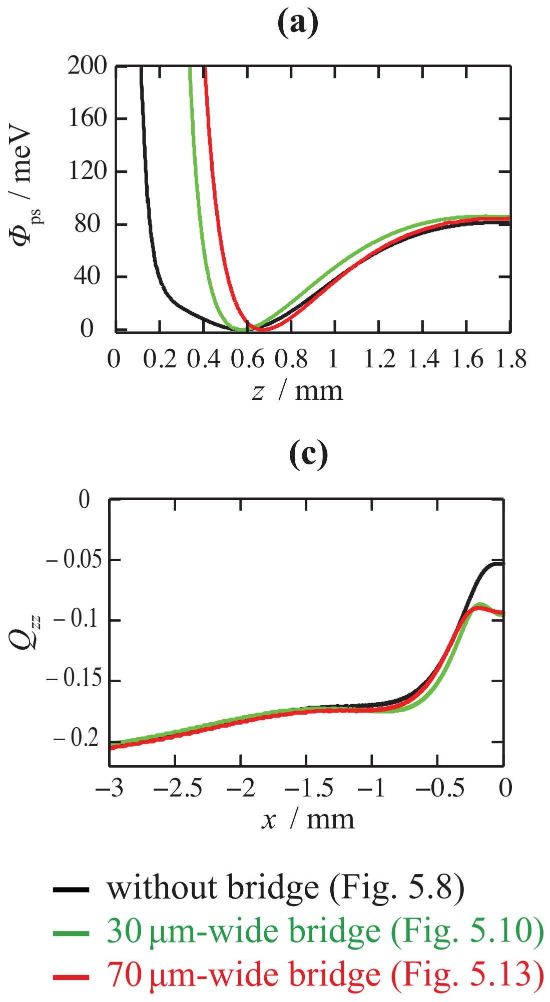

Figure 5.14: Comparison between the results deduced from the second optimisation. (a) One-dimensional cuts through pseudopotentials along the z-axis at the center of the junction. (b) The pseudopotential barriers, (c) the variation of the Q_{zz}, and (d) the variation of the trapping height along ion channels. The corresponding structures are depicted in Fig. 5.8, 5.10, and 5.13.

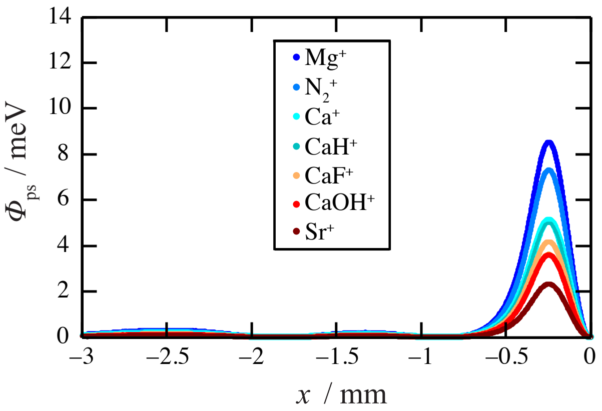

Figure 5.15: Pseudopotential barriers for various ion masses along the channel for the optimised cross junction presented in Fig. 5.13.

for minimising ion loss rates during shuttling.

5.4 Optimisation of the surface-electrode octupolar channel

A linear, octupole SE trap was one of the key elements to be integrated on the multi-functional chip (Section 5.1). Thus, the question arises again about the optimal electrode configuration that enables maximum trapping strength at a given height. Here we address this question and present a detailed characterization of such a structure. As in the previous section, the first and second optimisation are given subsequently.

5.4.1 First optimisation based on analytical calculations

To find the optimal geometry of a SE octupole trap, the following three approaches were considered. In the first approach, the *OptimalFinitePattern* routine from the *SurfacePattern* package was used to calculate the geometries yielding hexapole, octupole, and decapole potentials. In principle, the code computes an optimal surface geometry for a set of given local constraints, i.e., fixed values of the potential and derivatives at a certain point. Furthermore, the solutions re-

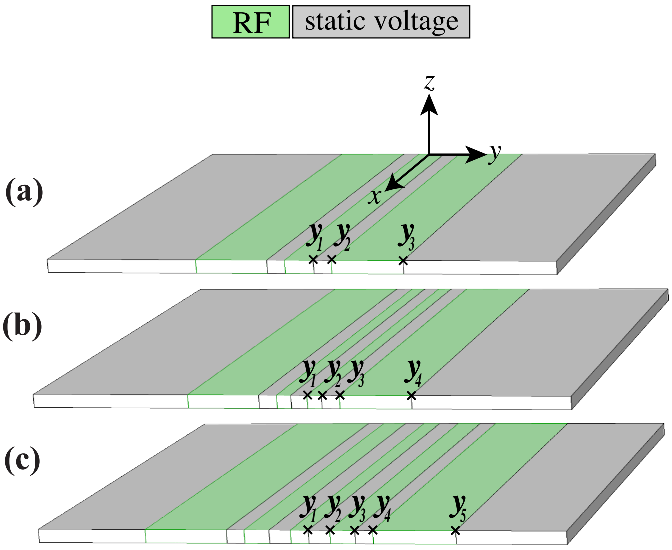

Figure 5.16: Schematics of the translationally symmetric surface-electrode multipole traps showing (a) seven-, (b) nine-, and (c) eleven-wire geometries. In (a-c), y_i (i=1,..,5) indicates the lateral position of the electrode edge (not to scale).

turned can maximise these values with optimised trapping strength. The rapid convergence to a unique solution is guaranteed by the relaxed Linear Programming (LP) method [198]. The geometries obtained for the hexapolar, octupolar, and decupolar channels were symmetric 7-, 9-, and 11-wire structures, repectively, as shown schematically in Fig. 5.16. The solutions provided a reasonable estimation of the position of the electrode edges. Fig. 5.17 shows the corresponding pseudopotentials evaluated for $^{40}\mathrm{Ca}^+$, $V_{\mathrm{RF}}=400$ V, and $\Omega_{\mathrm{RF}}=2\pi\times10.0$ MHz at 1 mm trapping height. Higher order multipoles offer spatially broader field-free regions, suited for applications such as spectroscopy and reaction studies (Section 2.3). However, the trapping depth rapidly decreases as the order of the multipole grows (Fig. 5.17 (a) and (b)).

In the second approach, assuming that symmetric configurations are superior solutions for ideal SE multipoles, the exact width of the optimum electrodes was analytically calculated. The strength of the RF potential at a given height h

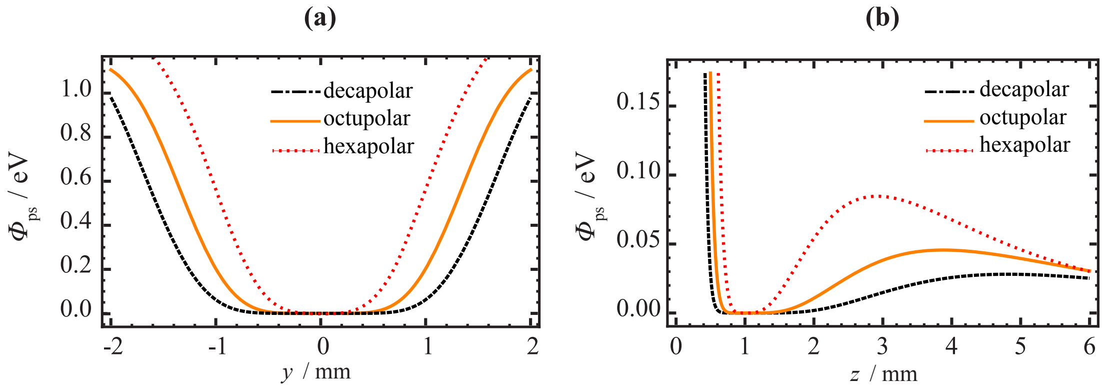

Figure 5.17: Pseudopotentials calculated for optimal hexapole, octupole, and decapole fields corresponding to seven-, nine-, and eleven-wire geometries, respectively. (a) and (b) show one-dimensional cuts along the y and z axes, respectively.

was maximised while the lower order multipole components were set to zero:

$$\begin{cases} \text{maximise:} & \left.\dfrac{\partial^n \phi_{\mathrm{RF}}(y_1, \ldots, y_m)}{\partial z^n}\right|_h \\ \text{subject to:} & \left.\dfrac{\partial^{i+j+k} \phi_{\mathrm{RF}}(y_1, \ldots, y_m)}{\partial x^i \partial y^j \partial z^k}\right|_h = 0 \quad (i{+}j{+}k{=}1,\ \ldots,\ n\text{-}1). \end{cases} \tag{5.6}$$

Here, ϕ_{RF} is the RF electrode basis function, n denotes the order of the multipole potential, and m is the number of degrees of freedom which is identical to the number of RF wires (Fig. 5.16). For the optimal 9-wire geometry, the solution of Eqn. 5.6 is given by $\{y_1, y_2, y_3, y_4\} = h \times \{-1-\sqrt{2}+\sqrt{2\,(2+\sqrt{2})}, 1-\sqrt{2}+\sqrt{4-2\sqrt{2}}, -1+\sqrt{2}+\sqrt{4-2\sqrt{2}}, 1+\sqrt{2}+\sqrt{2\,(2+\sqrt{2})}\} \cong h \times \{0.19891,$ $0.66818,\ 1.49661,\ 5.02734\}$. Fig. 5.18 demonstrates perfect agreement between the solution obtained from LP using the *OptimalFinitePattern* code and that calculated by solving Eqn. 5.6.

The third approach was based on conformal (or angle-preserving) mapping of conventional cylindrical trap geometries to strip electrodes on a plane. Thus,

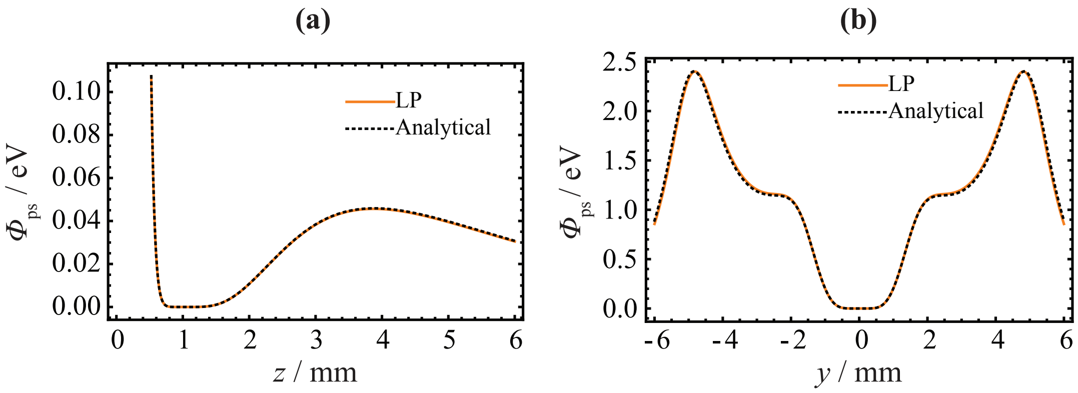

Figure 5.18: Comparison between the pseudopotentials calculated for the two optimal 9-wire designs: one obtained from analytical calculations, dashed line, and the other one deduced from optimiser code *OptimalFinitePattern* using Linear Programming (LP), in orange, both implemented in *Mathematica* [123, 169, 179]. (a) and (b) show one-dimensional contours along the y and z axes, respectively.

optimal electrode geometries of translationally symmetric SE multipoles, and analytical expressions of depth, and strength can be derived [124]. As illustrated in Fig. 5.19, the configuration is parametrised by the angle of θ_w extended by each strip as seen from the cylinder center, and an azimuthal angle θ_0 of the center of one strip. The strength of a nth-order guide α^n, defined as $\frac{\partial^n \phi_{\mathrm{RF}}}{\partial z^n}$, is formulated as [124]:

$$\alpha^n = 2^{-n}\frac{2}{\pi}\sin(\frac{n\theta_w}{2})\frac{V}{h^n}e^{-in\theta_0}, \tag{5.7}$$

where V is the applied voltage to strips. Thereby, the maximum value of $|\alpha^n|$ is reached for $\theta_w = \frac{\pi}{n}$. Figure 5.19 depicts the configuration of an optimal octupole trap showing maximum strength, where θ_w=$\pi/4$ and θ_0=$\pi/4$. In this case, the position of the electrode edges were calculated to be $\{y_1, y_2, y_3, y_4\} = h \times \{\tan\left(\frac{\pi}{16}\right), \tan\left(\frac{3\pi}{16}\right), \cot\left(\frac{3\pi}{16}\right), \cot\left(\frac{\pi}{16}\right)\} \cong h\times\{0.19891, 0.66818, 1.49661, 5.02734\}$. These solutions are exactly identical to those found from the second approach. Thus, all three approaches generate the same result.

Due to the broken symmetry in SE traps, an ideal multipole field is naturally prohibited, i.e., other multipoles additionally contribute to the trapping potential. Hence, a nth-order SE multipole is ideal if the lower order terms

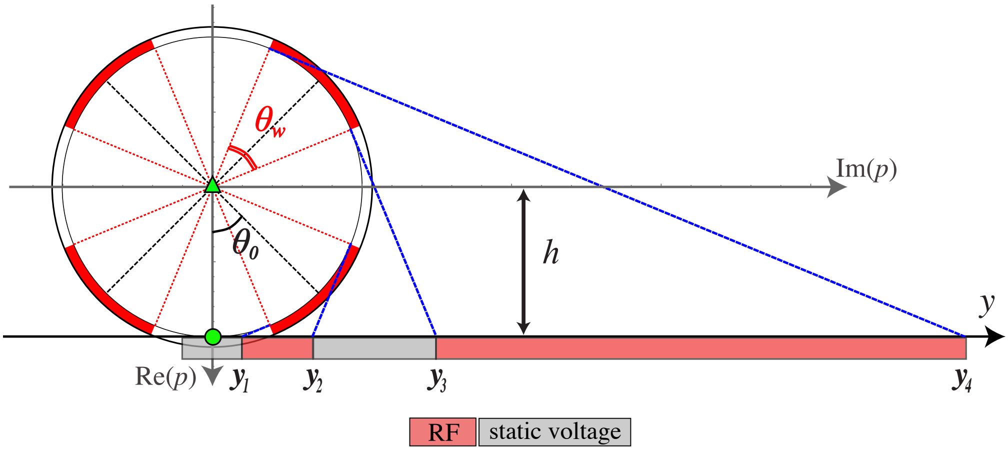

Figure 5.19: The graphical representation of conformal mapping of the optimal octupole surface-electrode trap. The green triangle and the circle indicate the trap center and the point on the electrode plane right below the trap center, respectively, and h is a given trapping height. The geometry is specified by θ_w and θ_0. The configuration illustrates the optimal octupole of maximum strength for the analytical solution $\theta_w = \pi/4$ and $\theta_0 = \pi/4$. The blue lines are the circle's tangents extended to the y axis which give the electrode edge positions $\{y_1, y_2, y_3, y_4\}$. Because of the rotational symmetry negative y values are not shown.

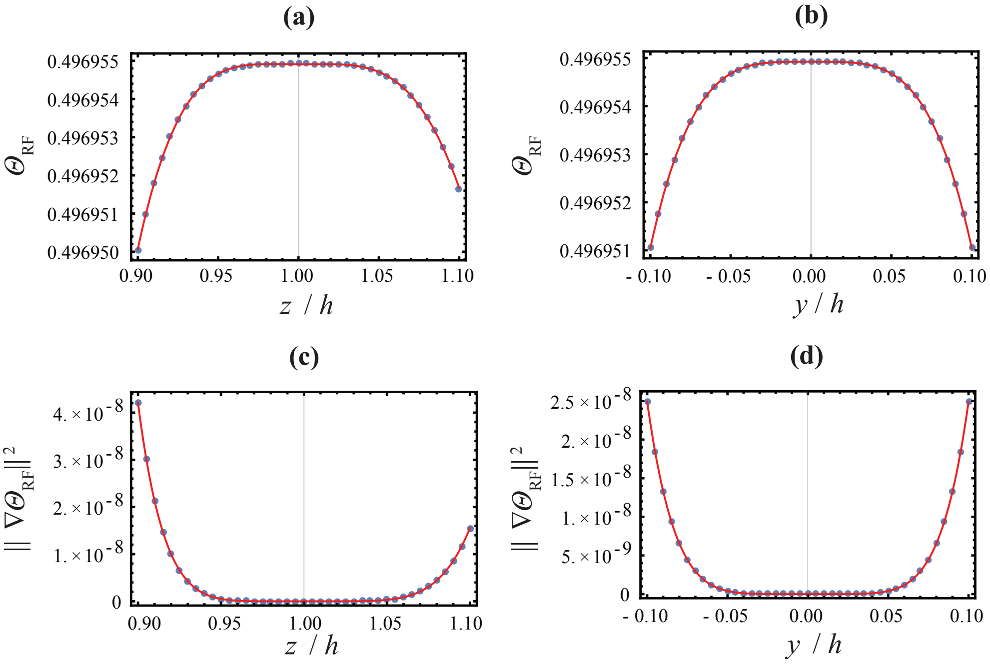

Figure 5.20: (a-b) RF electrode basis functions and (c-d) normalized pseudopotentials for the optimised octupolar surface-electrode geometry shown in Fig. 5.19. The circles are simulations, and the red curves are fits to power series demonestrating ρ^4 dependency for Θ_{RF} and ρ^6 dependency for $\|\nabla\Theta_{\mathrm{RF}}\|^2$.

dominating at the trapping center are well suppressed. Figure 5.20 shows one-dimensional cuts through the RF basis function and the normalized pseudopotential as well as fits to power series in the interval $[-0.1 \times h, +0.1 \times h]$. In analogy to three-dimensional multipole traps, the RF potential and pseudopotential of an octupole channel vary with ρ^4 and ρ^6, respectively (Section 2.3). Here, the contribution of the decapole term which drops with ρ^8 was appreciable, and therefore, the octupole term which varies with ρ^6 is prevalent near the center. In Fig. 5.20 (a) and (b), the RF potential exhibits negative strength both in the plane and out of the plane which is explained by non-zero θ_0, while the pseudupotential is a nearly square-shape three-dimensional well.

5.4.2 Second optimisation based on FEM using simplex algorithm

The optimal SE octupole geometry as discussed in the previous section was analysed using FEM with the inclusion of gaps. The result showed a non-vanishing RF field at the trapping center which yield three pseudopotential minima, see Fig. 5.22(i). Consequently, ions would be driven to unwanted regions, those in which atomic ions are not efficiently cooled by lasers. The problem is pronounced in the vertical direction (5.22(i) (c)), and would cause Coulomb crystals exhibiting unwanted, disordered structures. Thus, the influence of gaps must be taken into account in the optimisation. Attempts to compensate that force by the application of static fields would be inadequate because the effect is solely caused by incorporating gaps to the geometry and is independent of operational voltages.

Thus to deal with the influence of the gaps, an analytical treatment of the gaps to the second order of the gap aspect ratio (Section 5.4.3) was employed by Roman Schmied [169]. Additionally, the obtained geometry was modelled using FEM as shown in Fig. 5.22(ii) (a-c). The result showed that the trapping potential still suffered from barriers at the central region.

The important insight was that the gap effects cannot be analytically treated in SE multipoles, because the cancellation of the RF field results from many surface elements, and hence, the channel is very sensitive to any small change in the geometry. To address this issue, an optimisation process was established such that RF potentials obtained from FEM were used to generate objective functions numerically to be applied in an optimisation process conducted by the Nelder-Mead algorithm in *MATLAB*. The developed code utilized the *LiveLink*^{TM}*forMATLAB* module to create data for post processing in each iteration. In these calculations, the gap size was fixed to 120 μm, and the geometry was parametrised by the width of electrodes d_1, d_2, d_3, and d_4 as schematically shown in Fig. 5.21. It is notable that the accuracy of the gapless model is maximum when the electrode dimensions are measured from the center of one gap to the center of another, and not from the true edge of electrodes. The merit function was given by:

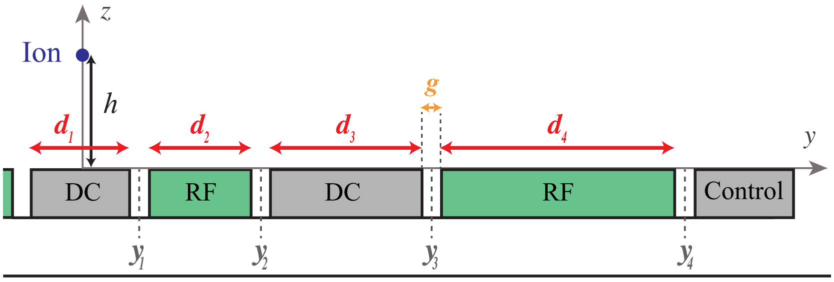

Figure 5.21: A schematic of the electrode configuration for a 9-wire surface-electrode octupole trap showing the parameters used in the first and second optimisation. The change of variables is given by $\{d_1, d_2, d_3, d_4\}$=$\{2y_1 - g,\, y_2 - y_1 - g,\, y_3 - y_2 - g,\, y_4 - y_3 - g\}$.

$$F(d_1, d_2, d_3, d_4) = \lambda_1 f^{(1)} + \lambda_2 f^{(2)} + \lambda_3 f^{(3)} - \lambda_4 f^{(4)}, \tag{5.8}$$

where the objective functions $f^{(n)}$ were formulated as $f^{(n)} = \frac{d^n f(d_1,d_2,d_3,d_4)}{dz^n}$. Here, the λ_i $(i = 1, 2, 3, 4)$ stands for the weighting factor including transformation coefficients discussed in Section 5.2.3. To simplify the calculations, we considered only the derivatives with respect to the vertical direction z. Also note that the Laplace equation links potential derivatives, and thus, in a translationally symmetric guide as investigated here, the derivatives with respect to the lateral direction y were implicitly affected in the calculations. The result demonstrated successful suppression of the residual fields at the center. Fig. 5.22(iii) (a-c) shows a large, field-free area of less than 0.1 meV potential.

A one-dimensional cut through the lateral axis y and a 6th-order polynomial regression fit to this data is presented in Fig. 5.23. It can be clearly seen that the contribution of quadrupole and hexapole terms are insignificant, and the potential well is dominated by the octupole term.

5.4.3 Effects of the gaps

This section discusses the influence of gaps on a linear octupolar channel in a quantitative fashion. The gap aspect ratio $\frac{t}{g}$, as illustrated in Fig. 5.24, was

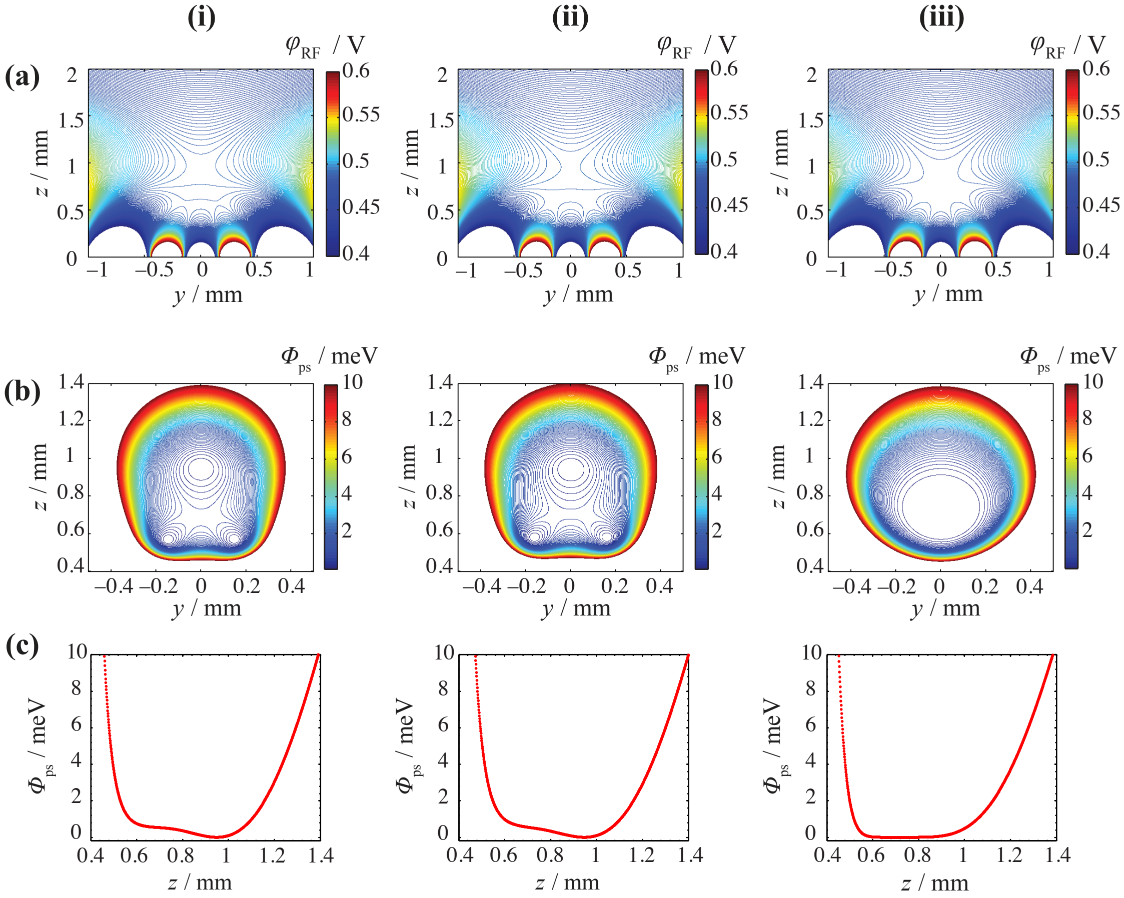

Figure 5.22: Results of the optimisation of the octupolar channel using three methods: (i) the optimised geometry was obtained from analytical calculations based on gapless plane approximation, (ii) the same as (i) but the gap effects were taken into account to the second order [169], and (iii) the geometry obtained from multi-objective optimisation processes using finite element methods (see text for details). (a) Contour plots of RF basis functions in the (y, z) plane, (b) isopotential contour plots of pseudopotentials calculated for Ca^+, and (c) One-dimensional cuts along the z-axis in the vicinity of the center of channels.

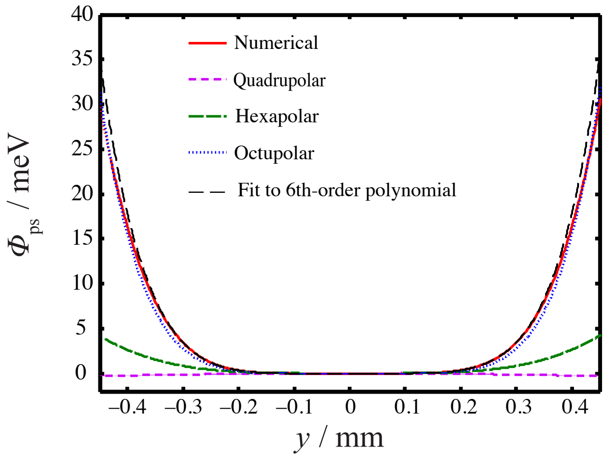

Figure 5.23: One-dimensional contour through the pseudopotential of the optimised octupolar channel illustrating the contributions from the quadrupole, hexapole, and octupole terms along the y-axis.

used to characterize the effect. The aspect ratios were discretely altered for the octupole trap geometry optimised numerically at t = 550 μm and g =120 μm. Figure 5.25 presents the RF and pseudopotential generated by those structures. For the structures featuring $\frac{t}{g} \geq 4$ the changes were found to be insignificant, see Fig. 5.25 (d-g) (i) and (ii). In contrast, for those of $\frac{t}{g} \leq 3$, the channel has been strongly degraded (Fig. 5.25 (a-c) (i) and (ii)).

This can be more clearly seen in one-dimensional cuts through the pseudo-

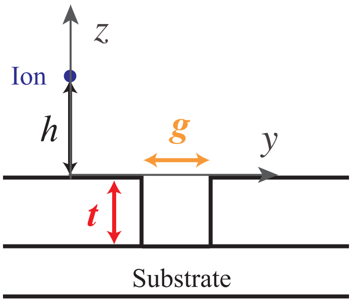

Figure 5.24: A schematic of a gap structure showing the aspect ratio $\frac{t}{g}$. g and t are the inter-electrode spacing and the trench depth, respectively, and h is characteristic trapping height.

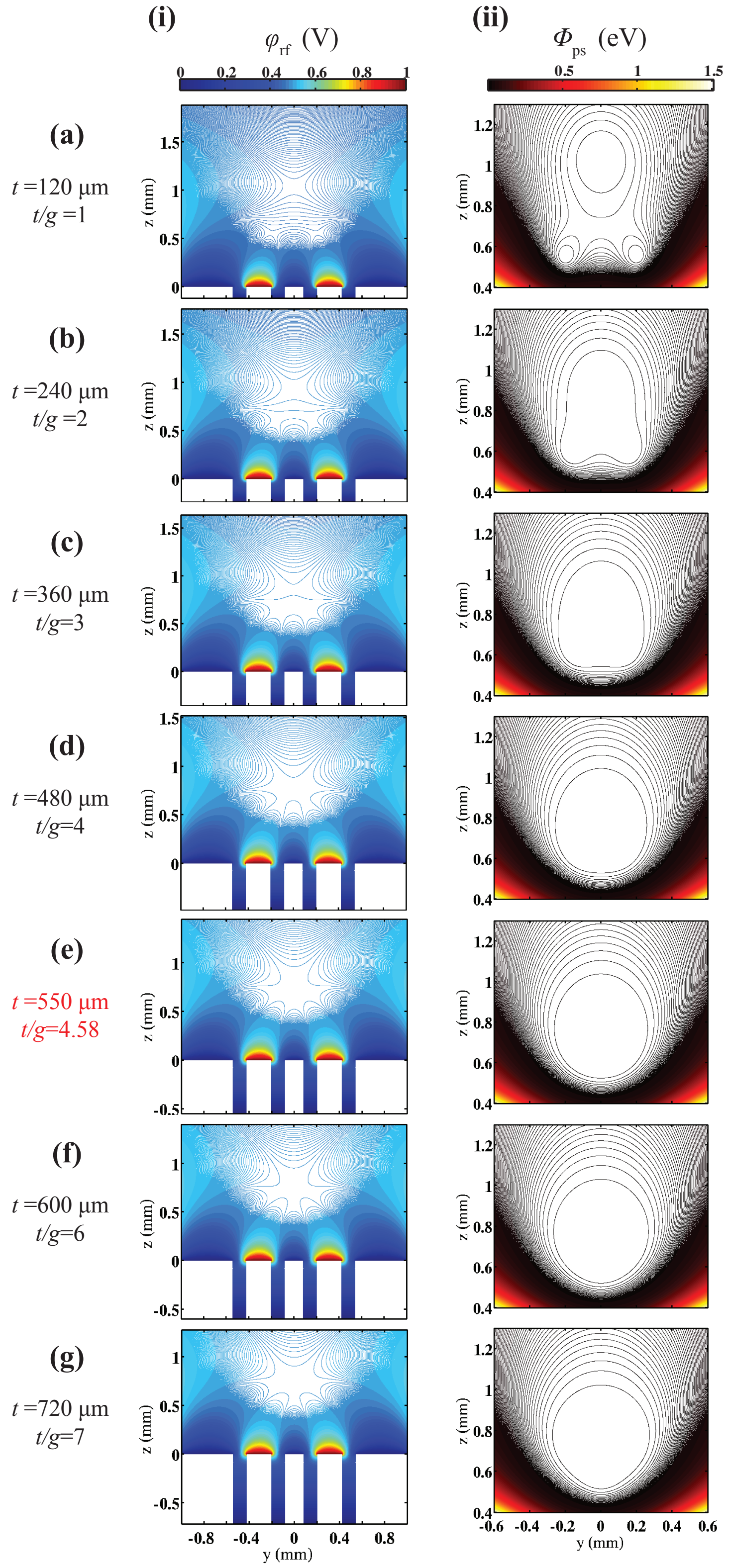

Figure 5.25: Variation of the octupolar channel profiles as a function of the trench depth obtained from finite element analysis. (i) Contour plots of RF basis functions, and (ii) pseudopotentials for Ca$^+$ calculated. The isopotential contours are separated by 1 meV and the central one indicates the 1-meV potential. Note that in (a-g) the width of the electrodes were fixed at the optimised values obtained for $\frac{t}{g}$=4.58. The aspect ratio was discretely altered from 1 in (a) to 7 in (g).

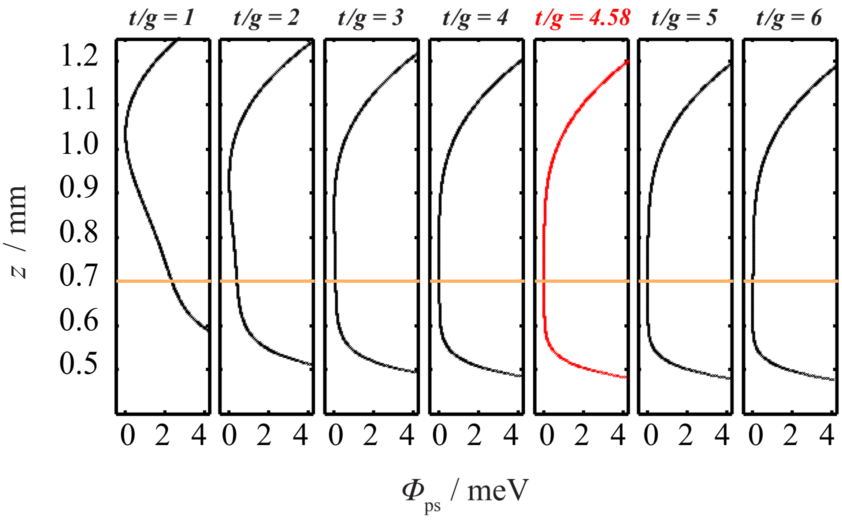

Figure 5.26: One-dimensional cuts through the pseudupotentials presented in Fig. 5.25 along the vertical axis z. The red curve represents the optimised configuration. The orange line indicates the elevation of 700 μm above the surface. Optimised channel is indicated in red. As the aspect ratio $\frac{t}{g}$ decreases, the first derivative of the pseudopotential is enhanced.

potentials along the vertical axis z (Fig. 5.26). In case of $\frac{t}{g}$=1, i.e., $t = 120$ μm, the minimum of the pseudopotential has been dramatically shifted to 1.034 μm. The explanation is provided by understanding the distinct role of the gap polarization and interpolation potentials that alter the surface potential. The surface potentials at the gap locations were extracted from FEM calculations for the cases shown in Fig. 5.25 (a-g). These results were compared to the interpolation potential that was analytically calculated for infinity thin electrodes following Ref. [169], see Fig. 5.27. The deviation of the surface potential from the interpolation potential arises from the polarization potential scaling with the gap aspect ratio. The effect is pronounced in the octupolar channel because of the sensitivity of the field-free region to the variation of the surface potential.

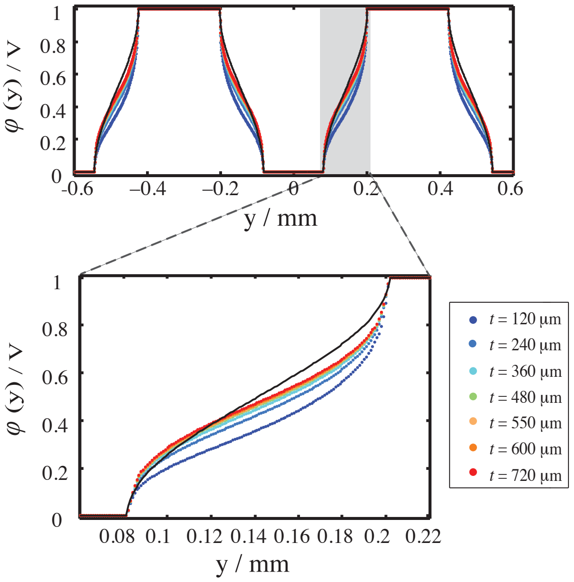

Figure 5.27: Surface electric potentials $\phi(y)$ computed for the structures shown in Fig. 5.25. The black line shows the analytically calculated gap interpolation potential. The inset shows a magnification of $\phi(y)$ in the closest gap to the trapping center.

5.4.4 Conclusions

The structure of a SE translationally symmetric octupole trap was optimised, and the influence of gaps on the trapping potential was explored. Based on these calculations, we inferred that the characteristics of the channel are a sensitive function of electrode width as well as inter-electrode spacing. The effect manifests itself in a considerable change of optimal electrode widths as presented in Table 5.2. Therefore, in the design of SE multipole guides the validity of the gapless plane approximation must be questioned, particularly in the case of low gap aspect ratios as well as in electrode structures comparable to the gap size. As a result, the optimal structures numerically computed for $t = 350\mu$m and $t = 550\mu$m are dissimilar.

Table 5.2: The optimised geometries of the linear SE octupole trap.

Optimisation algorithm	Potential modelling method	Electrode width [μm]			
		d_1	d_2	d_3	d_4
Linear Programming, numerical optimisation	analytical in gapless plane approx.	158	208	460	2352
Numerical optimisation, including gap effects to 2-nd order	analytical in gapless plane approx.	165	214	463	2368
Nelder-Mead	FEM for t = 550 μm	163	222	462	2375
Nelder-Mead	FEM for t = 350 μm	165	221	478	2332

5.5 Quadrupole-to-octupole field junction

To design an quadrupole-to-octupole field junction, which smoothly converts the quadrupolar potential to an octupolar one along one of the cross junction arms, similar calculations were performed using the tools developed for the cross junction (Section 5.2). The result obtained from the first optimisation was analysed using FEM, which assured that no further refinement was required in this case.

5.5.1 First optimisation based on analytical calculations

For the first optimisation, the geometry of the quadrupole-to-octupole junction was parametrised using three splines as discussed in Section 5.2.1, corresponding to 18 parameters. The solutions obtained converged to two surface patterns: those with a gradually enlarging RF electrodes, and those featuring rather complicated patterns, indicated with **J1** and **J2** in Fig. 5.28 (a), respectively. The different functionality of **J1** and **J2** is exhibited by the corresponding pseudopotential profiles. Figure 5.28 (b) illustrates the corresponding pseudopotentials for **J1** and **J2** calculated for ^{40}Ca^{+} at the RF voltage V_{RF}=300 V and the RF frequency Ω_{RF}=2π × 10.0 MHz, where the far quadrupolar channel minimum is elevated at 700 μm. **J1** was obtained from optimisation processes in which pseudopotential barriers were treated with large weighting factors. Such a pat-

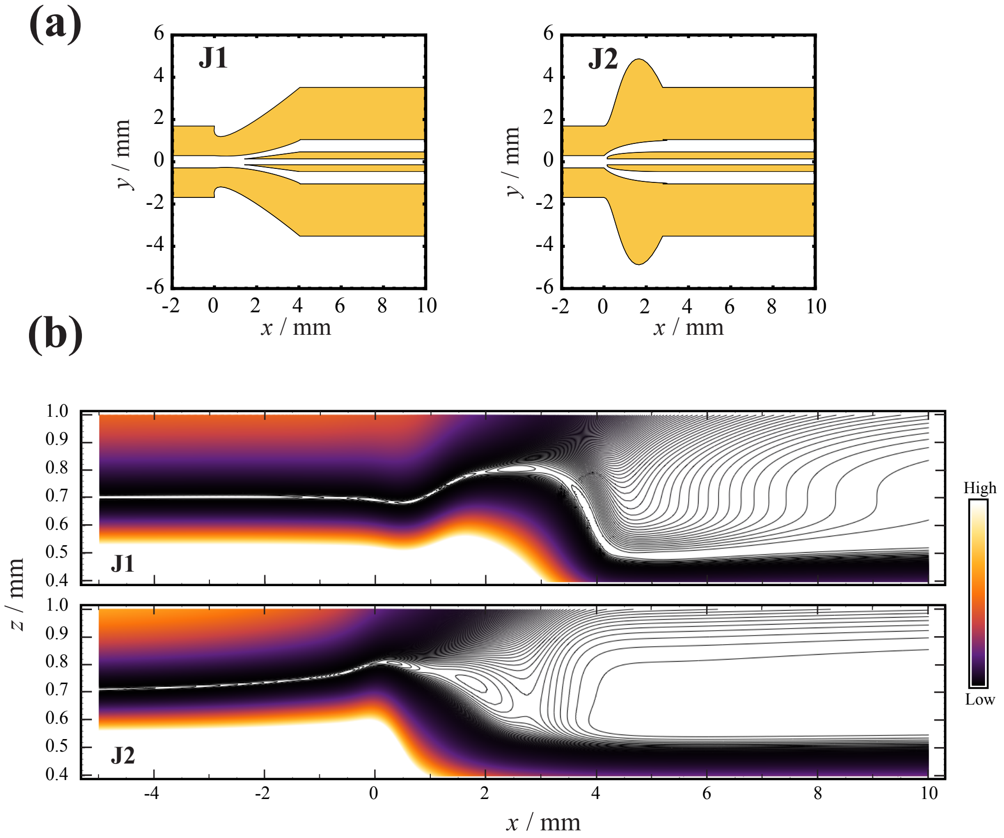

Figure 5.28: (a) Octupolar-to-quadrupolar junction geometries obtained from the first optimisation (RF (yellow) and DC (white) electrodes). (b) The pseudo-potential contour plots for **J1** and **J2**, illustrating variation of the potential profile along the ion channels.

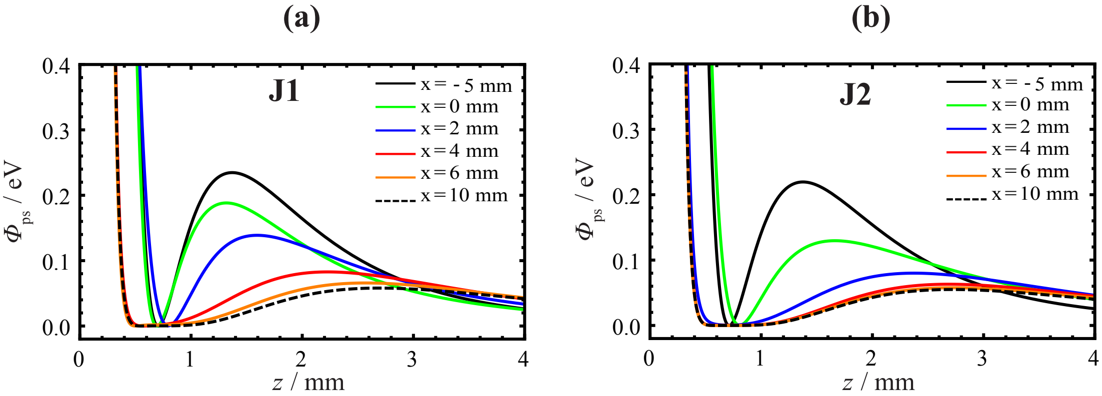

Figure 5.29: One-dimensional cuts through pseudopotentials for (a) **J1** and (b) **J2** along the vertical axis *z*, calculated at different spots along the ion channels as specified by the legends. For example, considering the contour at x= 2 mm in **J1** and **J2** the quadrupolar contribution is more prevalent in **J1** as compared to **J2**; however, in **J2** the octupolar contribution dominates.

tern can also be intuitively envisioned for an quadrupole-to-octupole junction, rendering a slow spatial variation of the trapping potential to match the two extremes. In contrast, it is evident that this transformation occurs in much shorter distance using **J2**.

One-dimensional contours of the pseudopotential at six various positions along the ion path for **J1** and **J2** are depicted in Fig. 5.29(a) and (b), respectively. The octupolar potential is formed in **J1** in 10 mm from its center, while this is only 4 mm in case of **J2**, i.e., the shuttling path was effectively reduced. The pseudopotential barriers calculated at the position of pseudopotential minima for the two structures is compared for N_2^+, Ca^+, and CaO^+, see Fig. 5.30. Although the pseudopotential barriers in **J2** are approximately two times larger, this is offset by the shorter shuttling distance, and hence has a lower loss rate of ions, making it the preferable geometry. It is worth noticing that in this type of junction ions are linearly shuttled along one-dimensional trapping arrays.

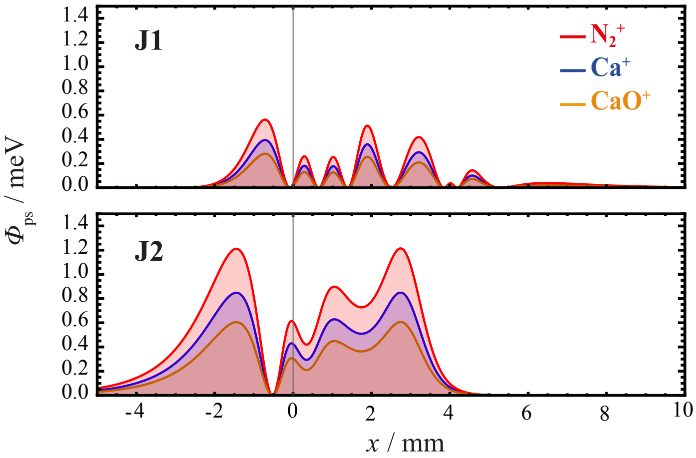

Figure 5.30: The pseudopotential barriers along the ion channel for N_2^+, Ca^+, and CaO^+ for the optimised junctions **J1** and **J2**.

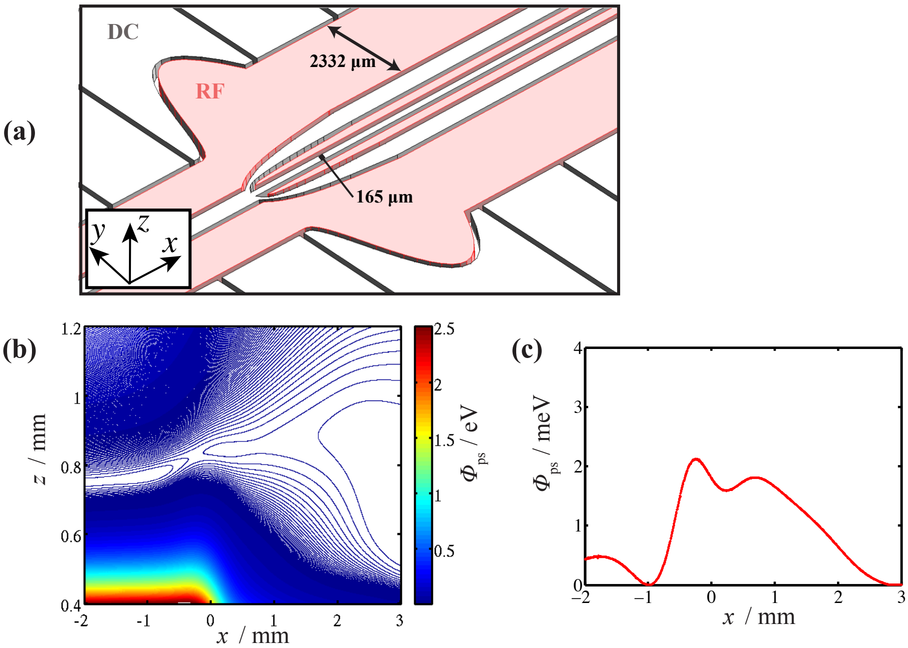

Figure 5.31: (a) The optimised geometry of the quadrupole-to-octupole field junction. (b) The pseudopotential in the (x,z) plane obtained from finite element analysis. The isopotential contours are separated by 0.001 eV and the central one indicates the 0.001-eV potential. (c) The pseudopotential barriers along the ion channel for Ca^+.

5.5.2 Finite element analysis of the quadrupole-to-octupole field junction

Figure 5.31(a) shows the structure of **J2** after incorporating 120 μm-wide gaps as well as slight refinements mainly to avoid sharp angles and overly narrow features. The result of the FEA is presented in Fig. 5.31 (b) illustrating smooth transitions between the octupole and quadrupole channel. The pseudopotential calculated for $^{40}\mathrm{Ca}^{+}$ at $\mathrm{V_{RF}}$=300 V and $\Omega_{\mathrm{RF}}=2\pi \times 10.0$ MHz shows barriers $<$ 2.2 meV (Fig. 5.31 (c)). These results ensure that the junction forms a smooth ion channel between the quadrupolar and octupolar regions, and thus, no further optimization was required.

5.6 Summary

The geometry of the chip has been developed by assembling the individually optimised components as discussed in this chapter. In Fig. 5.32 the overall view of the chip with the components is presented. The final size of the chip was decided considering two factors. First, the optimum distance required for decoupling the two junctions was calculated to be $14\times h$ (the trapping height), which is 9.8 mm in this case. Second, the total length of the electrodes was chosen such that the truncation effects were effectively eliminated.

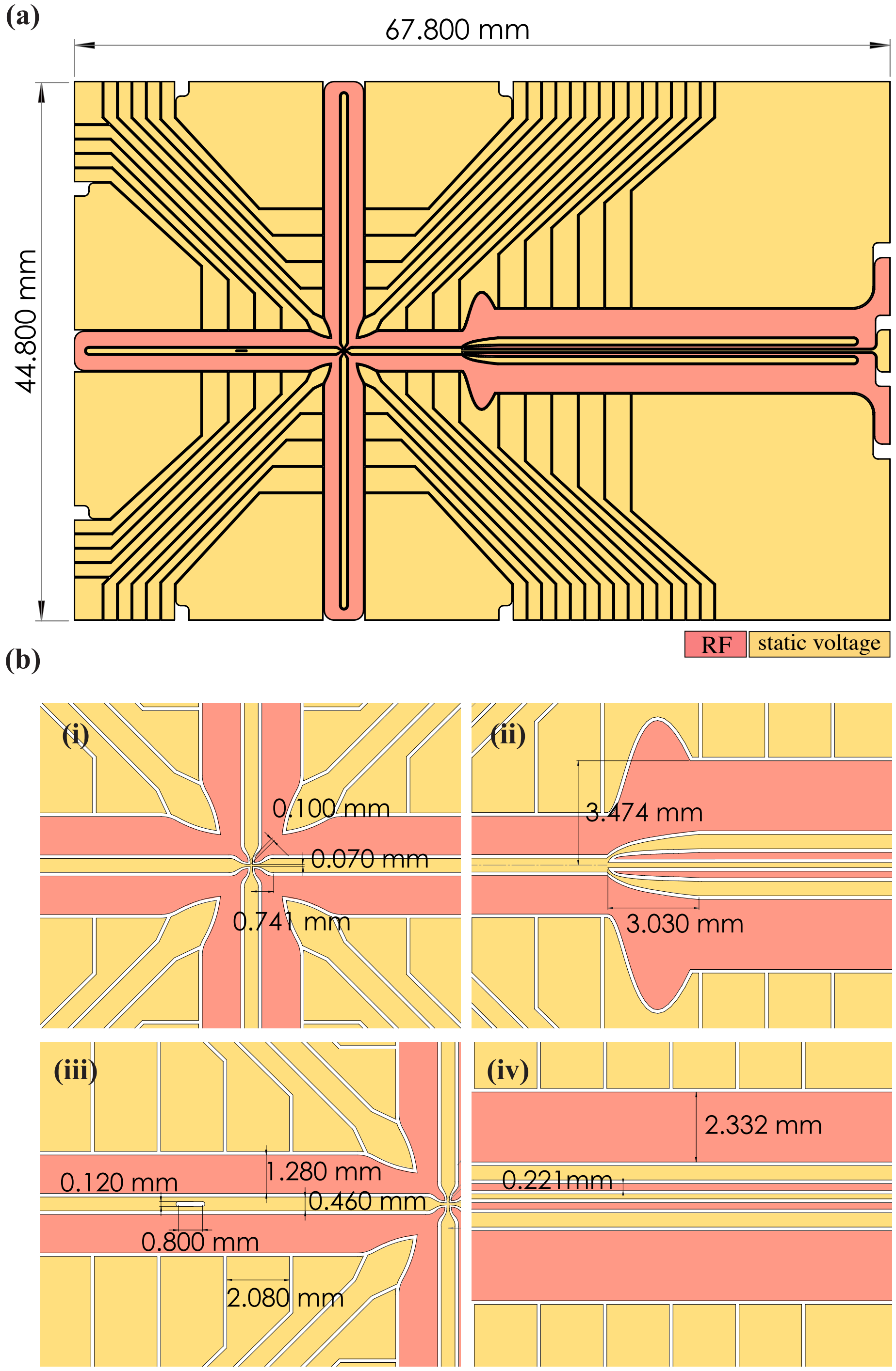

Figure 5.32: (a) The overall view of the chip. (b) The components as the design detailed in this chapter. (i) The cross junction, (ii) the quadrupole-to-octupole field junction, (iii) quadrupolar channel and the backside loading slot, and (iv) octupolar channel.

Chapter 6

Manufacturing

This chapter discusses the method for the fabrication of the multi-functional chip described in the previous chapter. As presented there, optimized features of the trapping potential (i.e., the suppressed pseudopotential barriers and gradients, as well as the controlled trapping height) are very sensitive to changes in the electrode geometry. Therefore, it is crucial to employ a high-precision fabrication technique so that the scale of any geometrical imperfections is negligible compared to the ion-electrode distance. Recent advancements in micro-electro-mechanical systems (MEMS) technology offer new possibilities for precise manufacturing of miniaturised traps [85]. The chip is constructed in collaboration with the Swiss Center for Electronics and Microtechnology *CSEM*[1].

6.1 Technical aspects

6.1.1 Substrate

The choice of trap substrate is important for a number of reasons. Microfabricated ion traps have been manufactured using various substrate materials which can broadly be classified into two categories: dielectric or semiconductor. An important theme in designing RF ion-trap chips is the power dissipation caused by RF losses which depends on the trap material and its dimensions [85].

---

[1] Rue Jaquet-Droz 1, CH-2002 Neuchâtel, Switzerland. http://www.csem.ch

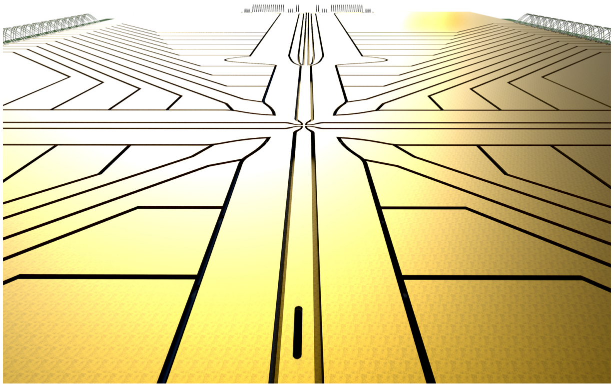

Figure 6.1: Schematic of the chip showing the backside loading slot through a central electrode of one of the quadrupolar arms. The width of the slot is 120 μm.

Traps with dielectric substrates such as sapphire or fused quartz [90, 181, 199–202] exhibit low RF loss, and electrodes are formed by standard lithographic techniques [203] on top of the substrate. The main disadvantage is that these materials are difficult to pattern and high-aspect-ratio electrodes are required to mitigate issues with exposed dielectrics. This becomes even more demanding when providing a slot for backside loading, which is often used in SE traps (Fig. 6.1). For instance, the most difficult part in the fabrication of the state-of-the-art chip demonstarted in Ref. [90] was found to be mechanical drilling of loading slots in a quartz substrate [204]. Alumina (Al_2O_3) wafers have been widely used in layer traps [205, 206], as well as in a three-dimensional X-junction [153] and T-junction [152]. These wafers exhibit excellent dielectric properties from DC to GHz frequencies as well as good thermal conductivity and can be precisely machined with picosecond lasers[2]. However, they are not suitable for our single-layer, large-size chip (44.8 mm×67.8 mm area, see Fig. 5.32) because of a number of reasons; the high stiffness of the alumina wafers leads to high risk of cracking and issues with mounting and vibration of free-standing electrodes. In addition, laser machining necessitates a fixed gap size for the entire geometry, and thus is not useful for the present design (Section 5.3.3 and, e.g., Fig. 5.12).

Another important feature which has been sought after since the advent of

---

[2] Fachhochschule Nordwestschweiz, Klosterzelgstrasse 2 CH-5210 Windisch, Switzerland. http://www.fhnw.ch/technik/ippe/dienstleistung

miniaturised traps is the capability of the trap fabrication method for including semiconductor technology [96, 207, 208]. In particular, using degenerate silicon[3] (i.e., silicon-on-insulator SOI) as the trap substrate [127, 208–210] or as trap electrodes [94, 211] opens up new possibilities such as the application of high voltages on microfabricated traps.

Another important consideration with regards to the substrate of SE traps concerns the implementation of experiments at low temperatures, i.e., in cryostat setups [210, 212–215]. Cryogenic cooling of ion traps is a key technique in high-precision spectroscopy, cold chemistry, and reaction studies [51, 138]. Moreover, quantum information processing (QIP) and quantum computation based on trapped-ion processors greatly benefit from this technique due to the suppression of anomalous heating, and hence, improving the coherence time of qubits [214, 216–219].

The substrate of the multi-functional chip is a high-purity float-zone silicon wafer[4] which features specifically high resistivity $>1000\,\Omega$-m. These wafers exhibit a low loss tangent[5] $\approx 10^{-3}$ in temperatures around 300 K, as well as below 20 K (i.e., freeze-out range) according to the temperature dependence of the mobility of charge carriers [220, 221]. A simulation of electro-thermal effects caused by the RF power dissipated on some chips showed that these wafers can be safely used in the RF frequency range of few tens of megahertz [222]. As a result, the device will be operational at room temperature, as well as at temperatures $< 20\,\mathrm{K}$. More importantly, arbitrary electrode geometries with

---

[3] degenerate or highly doped semiconducor acts as a conductor because the number of electrons in the conduction band approches that of a metal.

[4] High-purity, high-resistivity polished silicon wafers, crystal No. 43-0463-10, provided by Topsil Semiconductor Materials A/S, Siliciumvej 1 DK-3600 Frederikssund, Denmark. www.topsil.com

[5] The time-harmonic form of Maxwell-Ampère equation for an insulator with a complex permittivity $\epsilon = \epsilon' + \mathrm{i}\epsilon''$ [167], is formulated as:

$$\nabla \times \mathbf{H} = [(\sigma + \omega\epsilon'') - \mathrm{i}\omega\epsilon']\mathbf{E},$$

where σ is the conductivity of the material and ω is the angular frequency of the applied RF field. The ratio of the conduction to displacement current densities is commonly defined as loss tangent:

$$\tan\delta = \frac{\sigma + \omega\epsilon''}{\omega\epsilon'}.$$

high-aspect-ratio gap structures can be precisely manufactured (Section 6.2).

6.1.2 RF phase shift

For designing RF electrodes, pads, and connections, it is vital to avoid RF phase shifts which cause ion micromotion [108, 125, 223]. In the presence of a phase shift ϕ_{RF}, the total RF field at the trap centre does not vanish, and is given by:

$$\begin{aligned} E_{\mathrm{RF}}\mid_{\mathrm{h}} &= E_0\cos(\Omega_{\mathrm{RF}}t) - E_0\cos(\Omega_{\mathrm{RF}}t + \phi_{\mathrm{RF}}), \\ &= E_0(\cos(\Omega_{\mathrm{RF}}t) - \cos(\Omega_{\mathrm{RF}}t)\cos(\phi_{\mathrm{RF}}) + \sin(\Omega_{\mathrm{RF}}t)\sin(\phi_{\mathrm{RF}})), \end{aligned}$$

where E_0 and Ω_{RF} denote the RF field amplitude at the trap centre generated by one RF electrode and the RF frequency. By using the small-angle approximation for $\cos(\phi_{\mathrm{RF}})$ and $\sin(\phi_{\mathrm{RF}})$, one obtains:

$$E_{\mathrm{RF}}\mid_{\mathrm{h}} \approx E_0\phi_{\mathrm{RF}}\sin(\Omega_{\mathrm{RF}}t). \tag{6.1}$$

The response of the ion to this field can be found by assuming $x = x_{0\mu\mathrm{m}}\sin(\Omega_{\mathrm{RF}}t)$:

$$\begin{aligned} qE_{\mathrm{RF}}\mid_{\mathrm{h}} &= m\ddot{x}, \\ qE_0\phi_{\mathrm{RF}}\sin(\Omega_{\mathrm{RF}}t) &= m(-\Omega_{\mathrm{RF}}^2)x_{0\mu\mathrm{m}}\sin(\Omega_{\mathrm{RF}}t), \\ \Rightarrow x_{0\mu\mathrm{m}} &= -\frac{qE_0\phi_{\mathrm{RF}}}{m\Omega_{\mathrm{RF}}^2}, \end{aligned} \tag{6.2}$$

where $x_{0\mu\mathrm{m}}$ is the micromotion amplitude and m is the mass of the ion. The frequency modulation of the laser field due to the Doppler shift in the rest frame of the laser-cooled ion is given by $\mathbf{k}\cdot\mathbf{x}_{0\mu m} = \beta\cos(\Omega_{\mathrm{RF}}t)$ [108], where $\mathbf{k}$ is the wave-vector of the laser beam and β is the depth of modulation. The value of β must be sufficiently small to allow efficient laser cooling (e.g., <0.25 [125], see Section 2.2.2). Consider a path length difference $\Delta = 1$ cm between two RF electrodes. For $\Omega_{\mathrm{RF}} = 2\pi \times 20$ MHz, this yields a phase shift,

$$\phi_{\mathrm{RF}} = 2\pi \times \frac{\Delta}{\lambda_{\mathrm{RF}}} = 360^\circ \times \frac{0.01\mathrm{m}}{15\mathrm{m}} = 0.24^\circ.$$

This causes $x_{0\mu\mathrm{m}} = 62$ nm for $^{40}\mathrm{Ca}^{+}$ which is subjected to $E_0 = 9.6\times10^4\,\mathrm{V\,m^{-1}}$ (Eqn. 6.2). By assuming the maximum overlap between the micromotion direction and the k-vector of the laser beam, one obtains $\beta = \frac{1}{\sqrt{2}} \times |\mathbf{k}|x_{0\mu\mathrm{m}} = 0.67$.

This issue is avoided by applying the RF voltage to the chip via only one pad and all RF electrodes are connected in this design (Fig. 5.32). In this way, any geometrical difference between the paths supplying potential to the RF electrodes is avoided. Furthermore, RF electrodes might be coupled differently to the electical ground because the resistors and capacitors used are not exactly identical. This effect can dominate the RF phase shift in extreme cases [223]. Therefore, resistances and capacitive couplings must be measured at the desired RF frequency once the chip has been fabricated.

6.2 Fabrication method

The fabrication technique is based on standard lithographic methods and deep reactive ion etching (DRIE) of silicon wafers (Section 6.1.1) [203, 225]. Figure 6.2 schematically displays the sequence of this procedure [224]. Electrode geometries are patterned on a 675μm-thick wafer using a photoresist mask and DRIE (Fig. 6.2 (i-iii)). DRIE is a highly anisotropic etching process based on reaction with plasma (e.g., SF_6 is often used for silicon) which enables the construction of deep trenches and high-aspect-ratio structures [212, 226]. The side walls of the trenches are sightly sloped ($\approx 2^\circ$) forming undercuts in the structure (Fig. 6.2 (iii)). Consequently, dielectric surfaces which can be charged by lasers are eliminated. Then the photoresist is stripped and structure dimensions are fine tuned. Subsequently, a 2-3 μm layer of SiO_2 is grown by thermal oxidation. The structure is mechanically milled on the backside (Fig. 6.2 (vi)) to provide access for backside loading together with a slot through a central electrode of one of the quadrupolar arms (Fig. 6.1). The conductive top structure is formed by first evaporation of a adhesion layer (0.04 μm titanium) and then deposition of gold[6] with a nominal thickness of 1-μm. At this stage, the Au flux is directional so that the slightly sloped, vertical side walls are not coated

---

[6] Gold is a popular choice for ion traps because of its high work function as well as inertness [227].

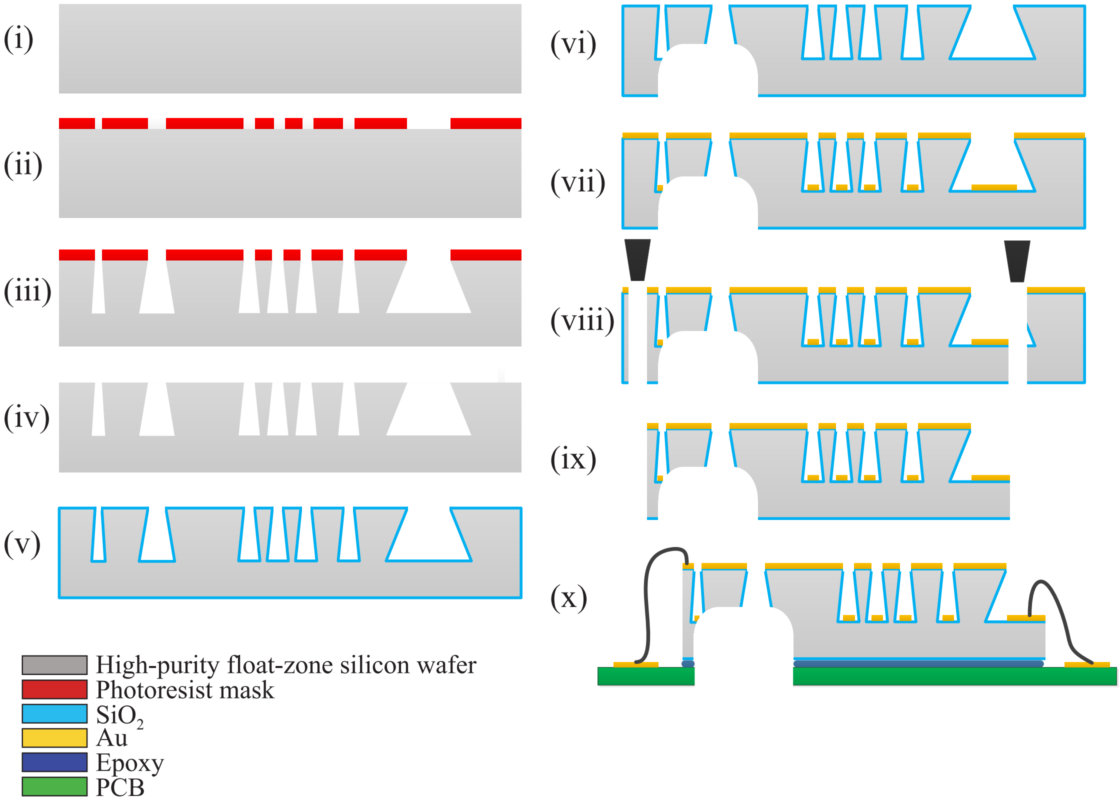

Figure 6.2: A schematic of the fabrication sequence [224]. (i-iii) Patterning of the bulk silicon using photoresist masks and DRIE. (iv) Stripping photoresist, cleaning, and dimensions fine tuning. (v) Forming a SiO$_2$ layer by means of thermal oxidation. (vi) Mechanical drilling on the backside of the structure while the top surface is protected. (vii) Directional gold coating. (viii) Dicing. (ix) Cleaning. (x) Assembling the structure on the PCB board and wire bonding. See text for details.

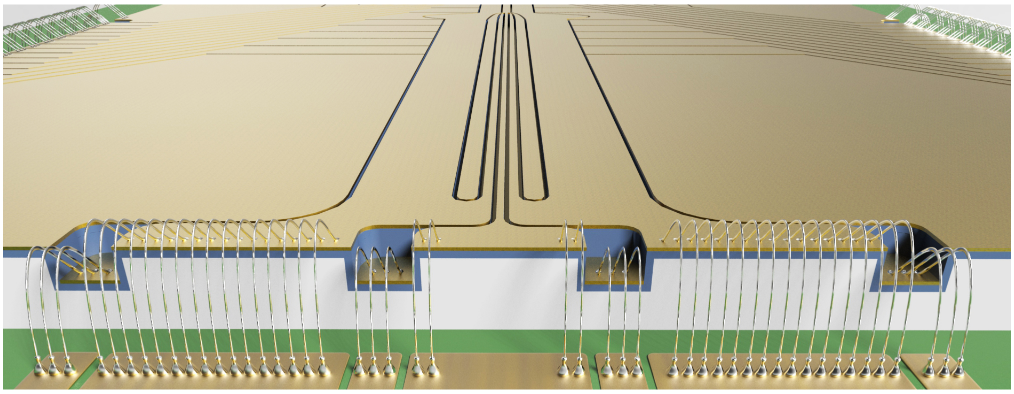

Figure 6.3: Illustration of the wire bonding of the bottom of the trenches.

with gold, resulting in electrical discontinuity between the top and bottom of the trenches (Fig. 6.2 (vii)). After dicing and cleaning, the structure is epoxied and assembled on a PCB board which contains in-vacuum electronics of the chip (Fig. 6.2 (viii-x)).

The precision of manufacturing is $\pm 2\,\mu$m which is much smaller than the $700\,\mu$m trapping height. The size of the finest structure in this manufacturing method is only restricted by practical limits such as voltage breakdown and mechanical stability of the structure. Each electrode is tapered by a factor of $2 \times t \times \tan 2^\circ$, where t is the trench depth. For $t = 350\,\mu$m, a 25 μm-wide electrode would be disconnected from the bulk due to the undercuts in the structure. Care was taken in optimizing the electrode geometries to avoid overly thin electrodes which may become disconnected. This choice also reduces the risk of damaging the structure when applying voltages. In particular, for the central bridge of the cross junction as discussed in Section 5.3.3, the width was constrained to 70 μm.

In ion channel intersections as well as in octupolar channels where the contributions of higher-order multipoles become large, the trench properties affect the trapping potential (Section 5.4.2). To reduce the sensitivity of the trapping potential, the bottom of the trenches are grounded using large openings provided for wire bonding (Fig. 6.3). This makes the device robust against exposed charges, which might be accumulated in the structure, and hence unwanted potentials.

6.3 Final chip features

The previous and current chapters present a detailed discussion about the design of the multi-functional chip with features summarised as follows:

(1) A single-layer monolithic chip device enables integration of several experimental zones in four linear quadrupolar channels and an octuplar one, where guiding ions between zones is facilitated by two junction structures.

(2) The trapping centre is generated at about 700 μm above the surface. At this trapping height, anharmonicity effects are still negligible (Section 4.4.3), and therefore, these contributions would not cause "intrinsic" segregation of mixed-species ion crystals[7].

(3) Gap structures were designed with undercuts, which combined with the possibility to ground the bottom of the trenches, makes the trap robust to the effects of exposed dielectrics.

(4) The device is operational at both room temperature and in cryogenic systems.

(5) There is the capability of backside loading.

---

[7] Note that this effect is caused by the trap geometry in a stationary configuration as opposed to the separation of bicomponent crystals in a shuttling process.

Chapter 7

Conclusions and Outlook

The goal of the project was to first demonstrate sympathetic cooling of molecular ions in a surface-electrode (SE) radiofrequency trap, and to characterise the energetic and structural properties of bicomponent Coulomb crystals in the trap using molecular dynamics (MD) simulation methods. N_2^+ and CaH^+ ions were confined in the SE trap and cooled by the interaction with laser-cooled Ca^+ ions to secular translational temperatures in the milliKelvin range. The configuration of trapping potentials generated by the surface electrodes enabled the formation of three- and two-dimensional bicomponent Coulomb crystals. In addition, a method for spatially separating the molecular from atomic ions above the surface of the chip using static control fields was detailed and the effect of the separation on the shape and energies of ionic species was discussed.

The effects of trap anharmonicities on the shape and energies of bicomponent crystals were theoretically explored. It was found that anharmonicities appreciably affect the crystal properties in small to medium-sized traps where the spatial extension of crystals becomes comparable to the smallest anharmonicity parameter of the specific trap used, but they can be neglected in large, mm-sized traps such as the six-wire SE trap used. Moreover, the calculations performed suggest that anharmonicity in the trapping potentials can deliberately be engineered to spatially separate ion species in bicomponent crystals.

Furthermore, a multi-functional, monolithic ion-trap chip has been developed to enable the integration of several experiments with cold molecular ions. This chip features carefully engineered ion channel intersections that enable transporting sympathetically cooled molecular ions in the form of bicomponent crystals. To achieve this, two junctions were designed: a cross between four quadrupolar ion channels featuring a central DC bridge which leads to a confining pseudopotential at the intersection centre, and a quadrupole-to-octupole junction. The geometry of the all constituent elements of the chip have been obtained from comprehensive optimisation processes. The resulting work additionally provides a route for designing and optimising arbitrary SE patterns to precisely shape trapping potentials.

The next step is the fabrication of the chip, which is currently being executed, as well as the design and implementation of the electronics of the chip. Sympathetically-cooled molecular ions will be shuttled together with co-trapped atomic ions in the presence of cooling laser beams. The figure of merit for the operation of the chip as a guided-ion beam machine is a minimum loss rate of molecular ions after many round trips. Coulomb crystallisation of molecular ions in the SE octupole field can be obtained, and as an interesting investigation the structure of these crystals can be manipulated. This chip offers new prospects for a significant simplification of the technological overhead for experiments with molecular ions, which have thus far mainly relied on complex and costly guided-ion beam machines [51, 160, 228].

A clear direction of future work is to develop combined experiments for the investigation of hybrid quantum systems, for instance, hybrid ion-atom traps [229, 230] or coupling trapped ions to other quantum systems such as mechanical oscillators [231, 232] as well as confined quantum emitters in an optical cavity [233]. The integration of a microfabricated trap with a microwave cavity [199] can also be extended to molecular ions [234]. The integration of microfabricated optics and imaging systems [235–237] promises the development of modular, compact devices for experiments with cold and controlled molecules.

Bibliography

[1] K. Southwell, *Nature*, 2002, **416**, 205.

[2] C. E. Wieman, D. E. Pritchard, and D. J. Wineland, *Rev. Mod. Phys.*, 1999, **71**, 253.

[3] D. J. Wineland, C. Monroe, W. M. Itano, D. Leibfried, B. E. King, and D. M. Meekhof, *J. Res. Natl. Inst. Stan.*, 1998, **103**, 259.

[4] N. Huntemann, B. Lipphardt, C. Tamm, V. Gerginov, S. Weyers, and E. Peik, *Phys. Rev. Lett.*, 2014, **113**, 210802.

[5] R. M. Godun, P. B. R. Nisbet-Jones, J. M. Jones, S. A. King, L. A. M. Johnson, H. S. Margolis, K. Szymaniec, S. N. Lea, K. Bongs, and P. Gill, *Phys. Rev. Lett.*, 2014, **113**, 210801.

[6] T. Pruttivarasin, M. Ramm, S. G. Porsev, I. I. Tupitsyn, M. S. Safronova, M. A. Hohensee, and H. Häffner, *Nature*, 2015, **517**, 592.

[7] A. Härter, A. Krükow, M. Dei, B. Drews, E. Tiemann, and J. Hecker Denschlag, *Nat. Phys.*, 2013, **9**, 512.

[8] F. H. J. Hall, M. Aymar, N. Bouloufa-Maafa, O. Dulieu, and S. Willitsch, *Phys. Rev. Lett.*, 2011, **107**, 243202.

[9] J. I. Cirac and P. Zoller, *Phys. Rev. Lett.*, 1995, **74**, 4091.

[10] H. Häffner, C. F. Roos, and R. Blatt, *Phys. Rep.*, 2008, **469**, 155.

[11] C. Monroe, D. M. Meekhof, B. E. King, S. R. Jefferts, W. M. Itano, D. J. Wineland, and P. Gould, *Phys. Rev. Lett.*, 1995, **75**, 4011.

[12] J. P. Home, D. Hanneke, J. D. Jost, J. M. Amini, D. Leibfried, and D. J. Wineland, *Science*, 2009, **325**, 1227.

[13] T. P. Harty, D. T. C. Allcock, C. J. Ballance, L. Guidoni, H. A. Janacek, N. M. Linke, D. N. Stacey, and D. M. Lucas, *Phys. Rev. Lett.*, 2014, **113**, 220501.

[14] I. Bloch, J. Dalibard, and S. Nascimbène, *Nat Phys*, 2012, **8**, 267.

[15] K. Kim, M.-S. Chang, S. Korenblit, R. Islam, E. E. Edwards, J. K. Freericks, G.-D. Lin, L.-M. Duan, and C. Monroe, *Nature*, 2010, **465**, 590.

[16] J. W. Britton, B. C. Sawyer, A. C. Keith, C. C. J. Wang, J. K. Freericks, H. Uys, M. J. Biercuk, and J. J. Bollinger, *Nature*, 2012, **484**, 489.

[17] D. Kienzler, H.-Y. Lo, B. Keitch, L. de Clercq, F. Leupold, F. Lindenfelser, M. Marinelli, V. Negnevitsky, and J. P. Home, *Science*, 2015, **347**, 53.

[18] J. Fortágh and C. Zimmermann, *Science*, 2005, **307**, 860.

[19] M. F. Riedel, P. Böhi, Y. Li, T. W. Hänsch, A. Sinatra, and P. Treutlein, *Nature*, 2010, **464**, 1170.

[20] C. F. Ockeloen, R. Schmied, M. F. Riedel, and P. Treutlein, *Phys. Rev. Lett.*, 2013, **111**, 143001.

[21] T. Rosenband, D. B. Hume, P. O. Schmidt, C. W. Chou, A. Brusch, L. Lorini, W. H. Oskay, R. E. Drullinger, T. M. Fortier, J. E. Stalnaker, S. A. Diddams, W. C. Swann, N. R. Newbury, W. M. Itano, D. J. Wineland, and J. C. Bergquist, *Science*, 2008, **319**, 1808.

[22] R. V. Krems, W. C. Stwalley, and B. Friedrich, *Cold Molecules: Theory, Experiment, Applications*, CRC Press, Boca Raton, 2009.

[23] Y.-P. Chang, K. Dlugolecki, J. Küpper, D. Rösch, D. Wild, and S. Willitsch, *Science*, 2013, **342**, 98.

[24] M. Quack, J. Stohner, and M. Willeke, *Annu. Rev. Phys. Chem.*, 2008, **59**, 741.

[25] D. DeMille, *Phys. Rev. Lett.*, 2002, **88**, 067901.

[26] J. Mur-Petit, J. Pérez-Ríos, J. Campos-Martínez, M. I. Hernández, S. Willitsch, and J. J. García-Ripoll, *Phys. Rev. A*, 2012, **85**, 022308.

[27] J. C. J. Koelemeij, B. Roth, A. Wicht, I. Ernsting, and S. Schiller, *Phys. Rev. Lett.*, 2007, **98**, 173002.

[28] M. Germann, X. Tong, and S. Willitsch, *Nature Phys.*, 2014, **10**, 820.

[29] H. Loh, K. C. Cossel, M. C. Grau, K.-K. Ni, E. R. Meyer, J. L. Bohn, J. Ye, and E. A. Cornell, *Science*, 2013, **342**, 1220.

[30] J. J. Hudson, D. M. Kara, I. J. Sallman, B. E. Sauer, M. R. Tarbutt, and E. A. Hinds, *Nature*, 2011, **473**, 493.

[31] O. Asvany, K. M. T. Yamada, S. Brünken, A. Potapov, and S. Schlemmer, *Science*, 2015, **347**, 1346.

[32] M. Drewsen, A. Mortensen, R. Martinussen, P. Staanum, and J. L. Sorensen, *Phys. Rev. Lett.*, 2004, **93**, 243201.

[33] P. F. Staanum, K. Højbjerre, and M. Drewsen in *Practical Aspects of Trapped Ion Mass Spectrometry*, Vol. 5; CRC Press, Boca Raton, 2010; p. 291.

[34] S. Willitsch, M. T. Bell, A. D. Gingell, S. R. Procter, and T. P. Softley, *Phys. Rev. Lett.*, 2008, **100**, 043203.

[35] S. Ospelkaus, K.-K. Ni, D. Wang, M. H. G. de Miranda, B. Neyenhuis, G. Quéméner, P. S. Julienne, J. L. Bohn, D. S. Jin, and J. Ye, *Science*, 2010, **327**, 853.

[36] F. H. J. Hall and S. Willitsch, *Phys. Rev. Lett.*, 2012, **109**, 233202.

[37] M. Kirste, X. Wang, H. C. Schewe, G. Meijer, K. Liu, A. van der Avoird, L. M. C. Janssen, K. B. Gubbels, G. C. Groenenboom, and S. Y. T. van de Meerakker, *Science*, 2012, **338**, 1060.

[38] S. Schiller, D. Bakalov, and V. I. Korobov, *Phys. Rev. Lett.*, 2014, **113**, 023004.

[39] S. Schiller and V. Korobov, *Phys. Rev. A*, 2005, **71**, 032505.

[40] J. Biesheuvel, J. P. Karr, L. Hilico, K. S. E. Eikema, W. Ubachs, and J. C. J. Koelemeij, *Nat. Commun.*, 2016, **7**, 10385.

[41] H. L. Bethlem and G. Meijer, *Int. Rev. Phys. Chem.*, 2003, **22**, 73.

[42] M. T. Bell and T. P. Softley, *Mol. Phys.*, 2009, **107**, 99.

[43] L. D. Carr, D. DeMille, R. V. Krems, and J. Ye, *New J. Phys.*, 2009, **11**, 055049.

[44] K. M. Jones, E. Tiesinga, P. D. Lett, and P. S. Julienne, *Rev. Mod. Phys.*, 2006, **78**, 483.

[45] T. Köhler, K. Gorál, and P. S. Julienne, *Rev. Mod. Phys.*, 2006, **78**, 1311.

[46] S. A. Rangwala, T. Junglen, T. Rieger, P. W. H. Pinkse, and G. Rempe, *Phys. Rev. A*, 2003, **67**, 043406.

[47] S. Y. T. van de Meerakker, H. L. Bethlem, N. Vanhaecke, and G. Meijer, *Chem. Rev.*, 2012, **112**, 4828.

[48] S. Chervenkov, X. Wu, J. Bayerl, A. Rohlfes, T. Gantner, M. Zeppenfeld, and G. Rempe, *Phys. Rev. Lett.*, 2014, **112**, 013001.

[49] A. Prehn, M. Ibrügger, R. Glöckner, G. Rempe, and M. Zeppenfeld, *Phys. Rev. Lett.*, 2016, **116**, 063005.

[50] F. G. Major, V. N. Gheorghe, and G. Werth, *Charged Particle Traps*, Springer, Berlin and Heidelberg, 2005.

[51] D. Gerlich, *Adv. Chem. Phys.*, 1992, **82**, 1.

[52] H. J. Metcalf and P. van der Straten, *Laser Cooling and Trapping*, Springer, New York, 1999.

[53] D. J. Wineland, J. C. Bergquist, W. M. Itano, J. J. Bollinger, and C. H. Manney, *Phys. Rev. Lett.*, 1987, **59**, 2935.

[54] S. Willitsch, *Int. Rev. Phys. Chem.*, 2012, **31**, 175.

[55] B. Heazlewood and T. P. Softley, *Annu. Rev. Phys. Chem.*, 2015, **66**, 475.

[56] J. P. Schiffer, *Phys. Rev. Lett.*, 2002, **88**, 205003.

[57] L. Hornekær, N. Kjærgaard, A. M. Thommesen, and M. Drewsen, *Phys. Rev. Lett.*, 2001, **86**, 1994.

[58] N. Kjærgaard and M. Drewsen, *Phys. Rev. Lett.*, 2003, **91**, 095002.

[59] S. Willitsch, M. T. Bell, A. D. Gingell, and T. P. Softley, *Phys. Chem. Chem. Phys.*, 2008, **10**, 7200.

[60] M. T. Bell, A. D. Gingell, J. Oldham, T. P. Softley, and S. Willitsch, *Faraday Discuss.*, 2009, **142**, 73.

[61] P. Bowe, L. Hornekaer, C. Brodersen, M. Drewsen, J. S. Hangst, and J. P. Schiffer, *Phys. Rev. Lett.*, 1999, **82**, 2071.

[62] E. S. Shuman, J. F. Barry, and D. DeMille, *Nature*, 2010, **467**, 820.

[63] M. T. Hummon, M. Yeo, B. K. Stuhl, A. L. Collopy, Y. Xia, and J. Ye, *Phys. Rev. Lett.*, 2013, **110**, 143001.

[64] V. Zhelyazkova, A. Cournol, T. E. Wall, A. Matsushima, J. J. Hudson, E. A. Hinds, M. R. Tarbutt, and B. E. Sauer, *Phys. Rev. A*, 2014, **89**, 053416.

[65] T. A. Isaev, S. Hoekstra, and R. Berger, *Phys. Rev. A*, 2010, **82**, 052521.

[66] A. D. Kudashov, A. N. Petrov, L. V. Skripnikov, N. S. Mosyagin, T. A. Isaev, R. Berger, and A. V. Titov, *Phys. Rev. A*, 2014, **90**, 052513.

[67] J. H. V. Nguyen, C. R. Viteri, E. G. Hohenstein, C. D. Sherrill, K. R. Brown, and B. Odom, *New J. Phys.*, 2011, **13**, 063023.

[68] M. D. Rosa, *Eur. Phys. J. D*, 2004, **31**, 395.

[69] Y. Gao and T. Gao, *Phys. Rev. A*, 2014, **90**, 052506.

[70] F. Robicheaux, *J. Phys. B: At. Mol. Opt. Phys.*, 2009, **42**, 195301.

[71] T. A. Isaev and R. Berger, *Phys. Rev. Lett.*, 2016, **116**, 063006.

[72] B. Roth and S. Schiller in *Cold Molecules*, ed. R. V. Krems, W. C. Stwalley, and B. Friedrich; CRC Press, Boca Raton, 2009; p. 651.

[73] R. E. Drullinger, D. J. Wineland, and J. C. Bergquist, *Appl. Phys.*, 1980, **22**, 365.

[74] D. J. Larson, J. C. Bergquist, J. J. Bollinger, W. M. Itano, and D. J. Wineland, *Phys. Rev. Lett.*, 1986, **57**, 70.

[75] T. Baba and I. Waki, *Jpn. J. Appl. Phys.*, 1996, **35**, 1134.

[76] K. Mølhave and M. Drewsen, *Phys. Rev. A*, 2000, **62**, 011401.

[77] A. Ostendorf, C. B. Zhang, M. A. Wilson, D. Offenberg, B. Roth, and S. Schiller, *Phys. Rev. Lett.*, 2006, **97**, 243005.

[78] L. Schmöger, O. O. Versolato, M. Schwarz, M. Kohnen, A. Windberger, B. Piest, S. Feuchtenbeiner, J. Pedregosa-Gutierrez, T. Leopold, P. Micke, A. K. Hansen, T. M. Baumann, M. Drewsen, J. Ullrich, P. O. Schmidt, and J. R. C. López-Urrutia, *Science*, 2015, **347**, 1233.

[79] A. K. Hansen, O. O. Versolato, L. Klosowski, S. B. Kristensen, A. Gingell, M. Schwarz, A. Windberger, J. Ullrich, J. R. C. Lopez-Urrutia, and M. Drewsen, *Nature*, 2014, **508**, 76.

[80] P. O. Schmidt, T. Rosenbrand, C. Langer, W. M. Itano, J. C. Bergquist, and D. J. Wineland, *Science*, 2005, **309**, 749.

[81] M. D. Barrett, B. DeMarco, T. Schaetz, V. Meyer, D. Leibfried, J. Britton, J. Chiaverini, W. M. Itano, B. Jelenković, J. D. Jost, C. Langer, T. Rosenband, and D. J. Wineland, *Phys. Rev. A*, 2003, **68**, 042302.

[82] J. P. Home, *Adv. At. Mol. Opt. Phys.*, 2016, **62**, 231.

[83] H. G. Dehmelt, *Adv. At. Mol. Phys.*, 1967, **3**, 53.

[84] W. Paul, *Rev. Mod. Phys.*, 1990, **62**, 531.

[85] M. D. Hughes, B. Lekitsch, J. A. Broersma, and W. K. Hensinger, *Contemp. Phys.*, 2011, **52**, 505.

[86] D. Kielpinski, C. Monroe, and D. J. Wineland, *Nature*, 2002, **417**, 709.

[87] J. Chiaverini, R. B. Blakestad, J. Britton, J. D. Jost, C. Langer, D. Leibfried, R. Ozeri, and D. J. Wineland, *Quantum Inf. Comput.*, 2005, **5**, 419.

[88] J. R. Castrejón-Pita and R. C. Thompson, *Phys. Rev. A*, 2005, **72**, 013405.

[89] C. Ospelkaus, U. Warring, Y. Colombe, K. R. Brown, J. M. Amini, D. Leibfried, and D. J. Wineland, *Nature*, 2011, **476**, 181.

[90] J. M. Amini, H. Uys, J. H. Wesenberg, S. Seidelin, J. Britton, J. J. Bollinger, D. Leibfried, C. Ospelkaus, A. P. VanDevender, and D. J. Wineland, *New J. Phys.*, 2010, **12**, 033031.

[91] J. P. Home and A. M. Stean, *Quantum Inf. Comput.*, 2006, **6**(4), 289.

[92] D. R. Crick, S. Donnellan, S. Ananthamurthy, R. C. Thompson, and D. M. Segal, *Rev. Sci. Instrum.*, 2010, **81**, 013111.

[93] C. Monroe and J. Kim, *Science*, 2013, **339**, 1164.

[94] R. C. Sterling, H. Rattanasonti, S. Weidt, K. Lake, P. Srinivasan, S. C. Webster, M. Kraft, and W. K. Hensinger, *Nat. Commun.*, 2013, **5**, 3637.

[95] D. A. Hite, Y. Colombe, A. C. Wilson, D. T. C. Allcock, D. Leibfried, D. J. Wineland, and D. P. Pappas, *MRS Bull.*, 2013, **38**, 826.

[96] D. Stick, W. K. Hensinger, S. Olmschenk, M. J. Madsen, K. Schwab, and C. Monroe, *Nat. Phys.*, 2006, **2**, 36.

[97] K. K. Mehta, A. M. Eltony, C. D. Bruzewicz, I. L. Chuang, R. J. Ram, J. M. Sage, and J. Chiaverini, *Appl. Phys. Lett.*, 2014, **105**, 044103.

[98] ed. J. Reichel and V. Vuletić, *Atom Chips*, Wiley-VCH, Weinheim, 2011.

[99] S. A. Meek, H. Conrad, and G. Meijer, *Science*, 2009, **324**, 1699.

[100] S. D. Hogan, P. Allmendinger, H. Saßmannshausen, H. Schmutz, and F. Merkt, *Phys. Rev. Lett.*, 2012, **108**, 063008.

[101] M. Germann PhD thesis, University of Basel, 2016.

[102] F. Wolf, Y. Wan, J. C. Heip, F. Gebert, C. Shi, and P. O. Schmidt, *Nature*, 2016, **530**, 457.

[103] J. C. J. Koelemeij, B. Roth, and S. Schiller, *Phys. Rev. A*, 2007, **76**, 023413.

[104] A. Mokhberi and S. Willitsch, *Phys. Rev. A*, 2014, **90**, 023402.

[105] A. Mokhberi and S. Willitsch, *New J. Phys.*, 2015, **17**, 045008.

[106] C. F. Foot, *Atomic Physics*, Oxford University Press, Oxford, 2005.

[107] M. Drewsen and A. Brøner, *Phys. Rev. A*, 2000, **62**, 045401.

[108] D. J. Berkeland, J. D. Miller, J. C. Bergquist, W. M. Itano, and D. J. Wineland, *J. Appl. Phys.*, 1998, **83**, 5025.

[109] M. G. Raizen, J. M. Gilligan, J. C. Bergquist, W. M. Itano, and D. J. Wineland, *Phys. Rev. A*, 1992, **45**, 6493.

[110] A. Mokhberi, Simulation of the trapping potential for a linear Paul trap report, University of Basel, 2011.

[111] D. Wineland in *Les Houches*, ed. D. Esteve, J.-M. Raimond, and J. Dalibard, Vol. 79; Elsevier, Amsterdam, 2004; p. 261.

[112] A. Drakoudis, M. Söllner, and G. Werth, *Int. J. Mass Spectrom.*, 2006, **252**, 61.

[113] F. A. Shaikh and A. Ozakin, *J. Appl. Phys.*, 2012, **112**, 074904.

[114] M. G. House, *Phys. Rev. A*, 2008, **78**, 033402.

[115] J. P. Home, D. Hanneke, J. D. Jost, D. Leibfried, and D. J. Wineland, *New J. Phys.*, 2011, **13**, 073026.

[116] D. H. E. Dubin, *Phys. Rev. Lett.*, 1993, **71**, 2753.

[117] H. Kaufmann, S. Ulm, G. Jacob, U. Poschinger, H. Landa, A. Retzker, M. B. Plenio, and F. Schmidt-Kaler, *Phys. Rev. Lett.*, 2012, **109**, 263003.

[118] J. P. Schiffer, *Phys. Rev. Lett.*, 1993, **70**, 818.

[119] I. M. Buluta, M. Kitaoka, S. Georgescu, and S. Hasegawa, *Phys. Rev. A*, 2008, **77**, 062320.

[120] I. M. Buluta and S. Hasegawa, *Phys. Rev. A*, 2009, **42**, 154004.

[121] B. Szymanski, R. Dubessy, B. Dubost, S. Guibal, J. P. Likforman, and L. Guidoni, *Appl. Phys. Lett.*, 2012, **100**, 171110.

[122] M. Madsen, W. Hensinger, D. Stick, J. Rabchuk, and C. Monroe, *Appl. Phys. B-Lasers O.*, 2004, **78**, 639.

[123] R. Schmied, J. H. Wesenberg, and D. Leibfried, *Phys. Rev. Lett.*, 2009, **102**, 233002.

[124] J. H. Wesenberg, *Phys. Rev. A*, 2008, **78**, 063410.

[125] J. M. Amini, J. Britton, D. Leibfried, and D. J. Wineland in *Atom Chips;* Wiley-VCH, Weinheim, 2011.

[126] W. M. Itano and D. J. Wineland, *Phys. Rev. A*, 1982, **25**, 35.

[127] D. T. C. Allcock, T. P. Harty, H. A. Janacek, N. M. Linke, C. J. Ballance, A. M. Steane, D. M. Lucas, R. L. Jarecki, S. D. Habermehl, M. G. Blain, D. Stick, and D. L. Moehring, *Appl. Phys. B*, 2012, **107**, 913.

[128] C. Roos, T. Monz, K. Kim, M. Riebe, H. Häffner, D. James, and R. Blatt, *Phys. Rev. A*, 2008, **77**, 040302.

[129] X. R. Nie, C. F. Roos, and D. F. V. James, *Physics Letters A*, 2009, **373**, 422.

[130] R. Alheit, C. Hennig, R. Morgenstern, F. Vedel, and G. Werth, *Applied Physics B*, 1995, **61**, 277.

[131] R. Alheit, S. Kleineidam, F. Vedel, M. Vedel, and G. Werth.

[132] Y. Wang, J. Franzen, and K. P. Wanczek, *International Journal of Mass Spectrometry and Ion Processes*, 1993, **124**, 125.

[133] J. Mikosch, U. Frühling, S. Trippel, D. Schwalm, M. Weidemüller, and R. Wester, *Phys. Rev. Lett.*, 2007, **98**, 223001.

[134] S. Schulz, U. Poschinger, K. Singer, and F. Schmidt-Kaler, *Fortschr. Phys.*, 2006, **54**, 648.

[135] G. D. Lin, S. L. Zhu, R. Islam, K. Kim, M. S. Chang, S. Korenblit, C. Monroe, and L. M. Duan, *Europhys. Lett.*, 2009, **86**, 60004.

[136] L. Wang and D. Babikov, *Phys. Rev. A*, 2011, **83**, 022305.

[137] N. Löch, E. Amitai, A. Nunnenkamp, and C. Bruder, *Phys. Rev. Lett.*, 2016, **117**, 073601.

[138] D. Gerlich, *Physica Scripta*, 1995, **T59**, 256.

[139] B. Höltkemeier, P. Weckesser, H. López-Carrera, and M. Weidemüller, *Phys. Rev. Lett.*, 2016, **116**, 233003.

[140] K. Okada, K. Yasuda, T. Takayanagi, M. Wada, H. A. Schuessler, and S. Ohtani, *Phys. Rev. A*, 2007, **75**, 033409.

[141] K. Okada, M. Ichikawa, M. Wada, and H. A. Schuessler, *Phys. Rev. Applied*, 2015, **4**, 054009.

[142] M. Debatin, M. Kröner, J. Mikosch, S. Trippel, N. Morrison, M. Reetz-Lamour, P. Woias, R. Wester, and M. Weidemüller, *Phys. Rev. A*, 2008, **77**, 033422.

[143] A. Walther, F. Ziesel, T. Ruster, S. Dawkins, K. Ott, M. Hettrich, K. Singer, F. Schmidt-Kaler, and U. Poschinger, *Phys. Rev. Lett.*, 2012, **109**, 080501.

[144] R. Bowler, J. Gaebler, Y. Lin, T. R. Tan, D. Hanneke, J. D. Jost, J. P. Home, D. Leibfried, and D. J. Wineland, *Phys. Rev. Lett.*, 2012, **109**, 080502.

[145] R. B. Blakestad, C. Ospelkaus, A. P. VanDevender, J. M. Amini, J. Britton, D. Leibfried, and D. J. Wineland, *Phys. Rev. Lett.*, 2009, **102**, 153002.

[146] F. Splatt, M. Harlander, M. Brownnutt, F. Zähringer, R. Blatt, and W. Hänsel, *New J. Phys.*, 2009, **11**, 103008.

[147] M. Kumph, P. Holz, K. Langer, M. Meraner, M. Niedermayr, M. Brownnutt, and R. Blatt, *New J. Phys.*, 2016, **18**, 023047.

[148] T. Schätz, U. Schramm, and D. Habs, *Nature*, 2001, **412**, 717.

[149] B. Tabakov, F. Benito, M. Blain, C. R. Clark, S. Clark, R. A. Haltli, P. Maunz, J. D. Sterk, C. Tigges, and D. Stick, *Phys. Rev. Applied*, 2015, **4**, 031001.

[150] P.-J. Wang, T. Li, C. Noel, A. Chuang, X. Zhang, and H. Häffner, *J. Phys. B: At. Mol. Opt. Phys.*, 2015, **48**, 205002.

[151] J. Hammer, S. Thomas, P. Weber, and P. Hommelhoff, *Phys. Rev. Lett.*, 2015, **114**, 254801.

[152] W. K. Hensinger, S. Olmschenk, D. Stick, D. Hucul, M. Yeo, M. Acton, L. Deslauriers, C. Monroe, and J. Rabchuk, *Appl. Phys. Lett.*, 2006, **88**, 034101.

[153] R. B. Blakestad PhD thesis, Universiy of Colorado, 2010.

[154] R. B. Blakestad, C. Ospelkaus, A. P. VanDevender, J. H. Wesenberg, M. J. Biercuk, D. Leibfried, and D. J. Wineland, *Phys. Rev. A*, 2011, **84**, 032314.

[155] J. Wesenberg, *Phys. Rev. A*, 2009, **79**, 013416.

[156] D. L. Moehring, C. Highstrete, D. Stick, K. M. Fortier, R. Haltli, C. Tigges, and M. G. Blain, *New J. Phys.*, 2011, **13**, 075018.

[157] G. Shu, G. Vittorini, A. Buikema, C. S. Nichols, C. Volin, D. Stick, and K. R. Brown, *Phys. Rev. A*, 2014, **89**, 062308.

[158] K. Wright, J. M. Amini, D. L. Faircloth, C. Volin, S. Charles Doret, H. Hayden, C.-S. Pai, D. W. Landgren, D. Denison, T. Killian, R. E. Slusher, and A. W. Harter, *New J. Phys.*, 2013, **15**, 033004.

[159] *GTRI Satellite ion traps for QIP applications, operation manual*, 2013.

[160] P. B. Armentrout, *J Am Soc Mass Spectrom*, 2002, **13**, 419.

[161] P. B. Armentrout, *J. Anal. At. Spectrom.*, 2004, **19**, 571.

[162] D. J. Douglas, A. J. Frank, and D. Mao, *Mass Spectrom. Rev.*, 2005, **24**, 1.

[163] R. D. Voyksner and H. Lee, *Rapid Communications in Mass Spectrometry*, 1999, **13**, 1427.

[164] C. Schneider, S. J. Schowalter, K. Chen, S. T. Sullivan, and E. R. Hudson, *Phys. Rev. Applied*, 2014, **2**, 034013.

[165] K. A. E. Meyer, L. L. Pollum, L. S. Petralia, A. Tauschinsky, C. J. Rennick, T. P. Softley, and B. R. Heazlewood, *J. Phys. Chem. A*, 2015, **119**, 12449.

[166] D. Hucul, M. Yeo, S. Olmschenk, C. Monroe, W. K. Hensinger, and J. Rabchuk, *Quantum Inf. Comput.*, 2008, **8**, 501.

[167] J. D. Jackson, *Classical Electrodynamics*, 3 ed., 1994.

[168] M. H. Oliveira and J. A. Miranda, *European Journal of Physics*, 2001, **22**, 31.

[169] R. Schmied, *New J. Phys.*, 2010, **12**, 023038.

[170] K. Singer, U. Poschinger, M. Murphy, P. Ivanov, F. Ziesel, T. Calarco, and F. Schmidt-Kaler, *Rev. Mod. Phys.*, 2010, **82**, 2609.

[171] J. P. Schiffer, M. Drewsen, J. S. Hangst, and L. Hornekaer, *Proc. Natl. Acad. Sci.*, 2001, **97**, 10697.

[172] J. P. Schiffer, *J. Phys. B: At. Mol. Opt. Phys.*, 2003, **36**, 511.

[173] C. B. Zhang, D. Offenberg, B. Roth, M. A. Wilson, and S. Schiller, *Phys. Rev. A*, 2007, **76**, 012719.

[174] K. Okada, M. Wada, T. Takayanagi, S. Ohtani, and H. A. Schuessler, *Phys. Rev. A*, 2010, **81**, 013420.

[175] D. H. E. Dubin and T. M. O'Neill, *Phys. Rev. Lett.*, 1988, **60**, 511.

[176] X. Tong, D. Wild, and S. Willitsch, *Phys. Rev. A*, 2011, **83**, 023415.

[177] I. Rouse and S. Willitsch, *Phys. Rev. A*, 2015, **92**, 053420.

[178] T. Matthey, T. Cickovski, S. S. Hampton, A. Ko, Q. Ma, M. Nyerges, T. Raeder, T. Slabach, and J. A. Izaguirre, *ACM Trans. Math. Softw.*, 2004, **30**, 237.

[179] R. Schmied, SurfacePattern software package, 2013.

[180] X. Tong, A. H. Winney, and S. Willitsch, *Phys. Rev. Lett.*, 2010, **105**, 143001.

[181] D. T. C. Allcock, J. A. Sherman, M. J. Curtis, G. Imreh, A. H. Burrell, D. J. Szwer, D. N. Stacey, A. M. Steane, and D. M. Lucas, *New J. Phys.*, 2010, **12**, 053026.

[182] COMSOL Multiphysics, www.comsol.com.

[183] M. J. Curtis PhD thesis, Universiy of Oxford, 2010.

[184] I. M. Georgescu, Five-wire SE ion trap fabrication report, University of Basel, 2010.

[185] R. M. Jones, D. Gerlich, and S. L. Anderson, *Rev. Sci. Instrum.*, 1997, **68**, 3357.

[186] I. M. Buluta and S. Hasegawa, *Phys. Rev. A*, 2008, **78**, 042340.

[187] B. Lekitsch, S. Weidt, A. G. Fowler, K. Mølmer, S. J. Devitt, C. Wunderlich, and W. K. Hensinger, *arXiv:1508.00420v2*, 2015.

[188] J. D. Siverns, S. Weidt, K. Lake, B. Lekitsch, M. D. Hughes, and W. K. Hensinger, *New J. Phys.*, 2012, **14**, 085009.

[189] F. N. Krauth, J. Alonso, and J. P. Home, *J. Phys. B: At. Mol. Opt. Phys.*, 2014, **48**, 015001.

[190] R. Reichle, D. Leibfried, R. B. Blakestad, J. Britton, J. D. Jost, E. Knill, C. Langer, R. Ozeri, S. Seidelin, and D. J. Wineland, *Fortschr. Phys.*, 2006, **54**, 666.

[191] H. A. Eschenauer, J. Koski, and A. Osyczka, in *Multicriteria Design Optimization: Procedures and Applications*, Springer Berlin, Heidelberg, 1990.

[192] W. Liu, S. Chen, and W. Wu, *Appl. Phys. B*, 2014, **117**, 1149.

[193] R. T. Marler and J. S. Arora, *Engineering Optimization*, 2005, **37**, 551.

[194] *Mathematica 10.0*, Wolfram Research, Inc., Champaign, Illinois, 2014.

[195] A. H. Nizamani and W. K. Hensinger, *Appl. Phys. B*, 2011, **106**, 327.

[196] B. Lekitsch PhD thesis, Universiy of Sussex, 2013.

[197] S. Pau and R. E. Slusher, 2007.

[198] K. Aardal and R. Weismantel in *Annotated bibliographies in combinatorial optimization;* Wiley, 1997.

[199] D. T. C. Allcock, T. P. Harty, C. J. Ballance, B. C. Keitch, N. M. Linke, D. N. Stacey, and D. M. Lucas, *Appl. Phys. Lett.*, 2013, **102**, 044103.

[200] P. F. Herskind, S. X. Wang, M. Shi, Y. Ge, M. Cetina, and I. L. Chuang, *Opics Lett.*, 2011, **36**, 3045.

[201] J. Labaziewicz PhD thesis, Massachusetts Institute of Technology, 2008.

[202] S. Seidelin, J. Chiaverini, R. Reichle, J. J. Bollinger, D. Leibfried, J. Britton, J. H. Wesenberg, R. B. Blakestad, R. J. Epstein, D. B. Hume, W. M. Itano, J. D. Jost, C. Langer, R. Ozeri, N. Shiga, and D. J. Wineland, *Phys. Rev. Lett.*, 2006, **96**, 253003.

[203] R. C. Jaeger, *Introduction to Microelectronic Fabrication (Modular Series on Solid State Devices* vol 5), Englewood-Cliffs, NJ: Prentice-Hall, 2 ed., 2002.

[204] C. Monroe, 12th canadian summer school on quantum infromation, University of Waterloo, 2012.

[205] S. A. Schulz PhD thesis, University of Ulm, 2009.

[206] D. Kienzler PhD thesis, Eidgenössische Technische Hochschule, Zürich, 2015.

[207] D. R. Leibrandt, J. Labaziewicz, R. J. Clark, I. L. Chuang, R. J. Epstein, C. Ospelkaus, J. H. Wesenberg, J. J. Bollinger, D. Leibfried, D. J. Wineland, D. Stick, J. Sterk, M. C., C.-S. Pai, Y. Low, R. Frahm, and R. E. Slusher, *Quantum Inf. Comput.*, 2009, **9**, 901.

[208] G. Wilpers, P. See, P. Gill, and A. G. Sinclair, *Nature Nanotech.*, 2012, **7**, 572.

[209] S. C. Doret, J. M. Amini, K. Wright, C. Volin, T. Killian, A. Ozakin, D. Denison, H. Hayden, C.-S. Pai, R. E. Slusher, and A. W. Harter, *New J. Phys.*, 2012, **14**, 073012.

[210] G. Vittorini, K. Wright, K. R. Brown, A. W. Harter, and S. C. Doret, *Rev. Sci. Instrum.*, 2013, **84**, 043112.

[211] J. Britton, D. Leibfried, J. A. Beall, R. B. Blakestad, J. H. Wesenberg, and D. J. Wineland, *Appl. Phys. Lett.*, 2009, **95**, 173102.

[212] M. Niedermayr, K. Lakhmanskiy, M. Kumph, S. Partel, J. Edlinger, M. Brownnutt, and R. Blatt, *New J. Phys.*, 2014, **16**, 113068.

[213] P. B. Antohi, D. Schuster, G. M. Akselrod, J. Labaziewicz, Y. Ge, Z. Lin, W. S. Bakr, and I. L. Chuang, *Rev. Sci. Instrum.*, 2009, **80**, 013103.

[214] S. Wang, J. Labaziewicz, Y. Ge, R. Shewmon, and I. L. Chuang, *Phys. Rev. A*, 2010, **81**, 062332.

[215] R. J. Clark, Z. Lin, K. S. Diab, and I. L. Chuang, *Journal of Applied Physics*, 2011, **109**, 076103.

[216] L. Deslauriers, S. Olmschenk, D. Stick, W. K. Hensinger, J. Sterk, and C. Monroe, *Phys. Rev. Lett.*, 2006, **97**, 103007.

[217] S. X. Wang, Y. Ge, J. Labaziewicz, E. Dauler, K. Berggren, and I. L. Chuang, *Appl. Phys. Lett.*, 2010, **97**, 244102.

[218] J. Labaziewicz, Y. Ge, P. Antohi, D. Leibrandt, K. R. Brown, and I. L. Chuang, *Phys. Rev. Lett.*, 2008, **100**, 013001.

[219] J. Labaziewicz, Y. Ge, D. Leibrandt, S. Wang, R. Shewmon, and I. L. Chuang, *Phys. Rev. Lett.*, 2008, **101**, 180602.

[220] L. Jensen, private communication.

[221] J. Krupka, J. Breeze, A. Centeno, N. Alford, T. Claussen, and L. Jensen, *IEEE Trans. Micro- wave Theory Tech.*, 2006, **54**, 3995.

[222] B. Lekitsch, private communication.

[223] J. Britton PhD thesis, University of Colorado, 2008.

[224] Y. Petremand, Multi-functional microchip project description, and private communication, Swiss Center for Electronics and Microtechnology *CSEM*.

[225] S. Franssila, *Introduction to Microfabrication*, Wiley Ltd., 2 ed., 2010.

[226] J. Parasuraman, A. Summanwar, F. Marty, P. Basset, D. E. Angelescu, and T. Bourouina, *Microelectronic Engineering*, 2014, **113**, 35.

[227] S. X. Wang, G. Hao Low, N. S. Lachenmyer, Y. Ge, P. F. Herskind, and I. L. Chuang, *J. Appl. Phys.*, 2011, **110**, 104901.

[228] O. Asvany, O. Ricken, H. S. P. Müller, M. C. Wiedner, T. F. Giesen, and S. Schlemmer, *Phys. Rev. Lett.*, 2008, **100**, 233004.

[229] M. Cetina, A. Grier, J. Campbell, I. Chuang, and V. Vuletic, *Phys. Rev. A*, 2007, **76**, 041401.

[230] A. T. Grier, M. Cetina, F. Oručević, and V. Vuletić, *Phys. Rev. Lett.*, 2009, **102**, 223201.

[231] K. R. Brown, C. Ospelkaus, Y. Colombe, A. C. Wilson, D. Leibfried, and D. J. Wineland, *Nature*, 2011, **471**, 196.

[232] W. K. Hensinger, D. W. Utami, H.-S. Goan, K. Schwab, C. Monroe, and G. J. Milburn, *Phys. Rev. A*, 2005, **72**, 041405.

[233] S. Begley, M. Vogt, G. K. Gulati, H. Takahashi, and M. Keller, *Phys. Rev. Lett.*, 2016, **116**, 223001.

[234] D. I. Schuster, L. S. Bishop, I. L. Chuang, D. DeMille, and R. J. Schoelkopf, *Phys. Rev. A*, 2011, **83**, 012311.

[235] C. R. Clark, C. Chou, A. R. Ellis, J. Hunker, S. A. Kemme, P. Maunz, B. Tabakov, C. Tigges, and D. L. Stick, *Phys. Rev. Appl.*, 2014, **1**, 024004.

[236] S. Marx, D. Adu Smith, M. J. Abel, T. Zehentbauer, G. Meijer, and G. Santambrogio, *Phys. Rev. Lett.*, 2013, **111**, 243007.

[237] E. W. Streed, B. G. Norton, A. Jechow, T. J. Weinhold, and D. Kielpinski, *Phys. Rev. Lett.*, 2011, **106**, 010502.

List of puplications

- A. Mokhberi, R. Schmied, and S. Willitsch,
  "Optimal surface-electrode ion-trap junctions for experiments with cold molecular ions", under preparation.

- A. Mokhberi and S. Willitsch,
  "Structural and energetic properties of molecular Coulomb crystals in a surface-electrode ion trap" New J. Phys. **17**, 045008 (2015), invited for the Focus on New Frontiers of Cold Molecules Research.

- A. Mokhberi and S. Willitsch,
  "Sympathetic cooling of molecular ions in a surface-electrode ion trap" Phys. Rev. A **90**, 023402 (2014).